Studies on Effect of Surface Profiles and Field Shaper Geometries on Electromagnetic Crimping of Tubes on Rods

A thesis submitted for the award of degree of

DOCTOR OF PHILOSOPHY

by

RAMESH KUMAR

(Roll No: 146103008)

DEPARTMENT OF MECHANICAL ENGINEERING

INDIAN INSTITUTE OF TECHNOLOGY GUWAHATI

GUWAHATI – 781039, INDIA

OCTOBER, 2018

Dedicated to My Parents

Suresh Choudhary

Manju Devi

Whose blessings and endless faith always

Inspired me to move forward

Declaration

I hereby certify that the information presented in this dissertation '**Studies on Effect of Surface Profiles and Field Shaper Geometries on Electromagnetic Crimping of Tubes on Rods**' is entirely my own account of research performed under the supervision of Prof. Sachin Dnyandeo Kore. Any part of this work has not earlier been submitted for the award of any degree, diploma, associate-ship, fellowship or its equivalent to any Institution or University.

Ramesh Kumar
Roll No. 146103008
Department of Mechanical Engineering
Indian Institute of Technology Guwahati
Assam-781039, INDIA

Certificate

It is certified that the work presented in the thesis entitled '**Studies on Effect of Surface Profiles and Field Shaper Geometries on Electromagnetic Crimping of Tubes on Rods**' submitted by Mr. Ramesh Kumar, a student in the Mechanical Engineering Department, Indian Institute of Technology Guwahati, for the award of the degree of Doctor of Philosophy has been carried out under my supervision. This work has not been submitted previously elsewhere for the award of any other degree or diploma.

Dr. Sachin D. Kore
Department of Mechanical Engineering
Indian Institute of Technology Guwahati
Assam-781039, INDIA

Acknowledgment

It is a pleasure to express my thanks wholeheartedly to every, and each one contributed to make this Ph.D. achievable. I wish to express my heartfelt gratitude to Prof. Gautam Biswas (Director of the Institute). I am grateful to former and present heads of the Department of Mechanical Engineering, Prof. Anoop K. Dass and Prof. S. K. Dwivedy for extending various facilities during the tenure of my doctoral program. I am also grateful to the marvelous faculty and staff of the Indian Institute of Technology Guwahati for the familial environment.

I would like to express my gratitude to supervisor Dr. Sachin D. Kore for his guidance and intellectual inputs throughout the completion of the research work. His amazing skills of organization, planning and management tough me a lot, and his mesmerizing ability to bring me confidence and peaceful in any dilemma I have faced, and I indeed appreciate his parental supervision.

I thank the members of my doctoral committee: Prof. S. Senthilvelan (Chairman), Prof. Pankaj Biswas and Prof. Harshal B. Nemade for their time, encouragement and valuable suggestions during my doctoral research work.

I wish to express my sincere thanks to Mr. Jiten Basumatary, Mr. Amal Kalita, Mr. Nip Borah, Mr. Sanjib Sarma and Mr. S. Ahmed for their assistance during the experimental work. I sincerely thank Mr. N. K. Das, Mr. D. Chetri, Mr. N. Saikia, Mr. M. Sarma, Mr. B. Chandan, Mr. U. Gohain, and Mr. M.C. Medhi for their help in conducting experiments. I also like to thank the entire group of Central Instruments Facility IIT Guwahati for their directly or indirectly support.

I express my sincere thanks to my friends Mr. Jyoti K. Doley, Dr. Chandrahas Patel, Dr. Ashish K. Rajak, Mr. Piyush Singh, Mr. Getu T. Areda, Mr. Sagar Pawar, Mr. Avinish Tiwari, Mr. Deepak Kumar, Mr. Alok Kumar for their help and encouragement. My sincere thanks also go to Mr. Srikant Prasad, Mr. P.V.S.S. Sridhar, and Mr. Rasmi R. Behera.

I will always be grateful to my parents (Mr. Suresh Choudhary and Ms. Manju Devi), my brother Mr. Nitesh Kumar and my sisters Nirmala Kumari and Nitu Devi for their unconditional love, support and encouragement during my research work.

April 2018 Ramesh Kumar

Abstract

The electromagnetic crimping (EMC) is a high energy, high strain rate, high velocity and green mechanical joining technique. Joining of dissimilar materials was very difficult because their physiochemical properties are seldom compatible or similar. Therefore, this type of solid-state joining technique can be an alternative for joining dissimilar materials.

Numerical studies as well as experimental work were carried out for EMC process. Numerical simulations were carried out for finding out the optimized parameters for crimping and then experiments were conducted on the optimized parameters. The results obtained from the simulations revealed that for the successful crimping minimum value of collision velocity, plastic strain, electromagnetic pressure, and stand-off distance must be maintained.

To increase the strength of the joint profiles were created on the base rod. There were three types of profiles created threaded, knurled, and plain profile. The influence of these profiles on the joint strength, surface roughness and microstructure of the joint were analyzed and compared. Mechanical tests such as compression-shear test and a pull-out test revealed that threaded surface profile on the steel rod gives better strength in comparison to the other two profiles.

Along the circumference of the Copper-Steel composite rod, the microstructure images of the joints were analyzed and it was found that there was a negligible gap along the circumference of the sample crimped at 5.3 kJ of discharge energy with a plain profile. This study has been carried out with two different combinations of materials such as aluminum-steel and Copper-Steel. For the Copper-Steel combination of materials, tapered field shaper was used whereas for aluminum-steel combination of materials stepped field shaper was used.

Further, to compare to the performance of the field shaper. A comparative experimental as well as a numerical study has been carried out for three different types of field shapers namely tapered, step-tapered and stepped field shapers. In this comparison the material combination used was Copper-Aluminum. From the study it can be concluded that the step-tapered field shaper results better in terms of uniformity in crimp quality, joint strength in compression, joint strength in tension, joint electrical resistance, joint leakage and surface finish of the crimped sample among the three types of field shaper.

The comparative study of the three types of field shaper was further extended to measure the temperature generation near the working zone. The measured temperature distribution in the experiments were compared with the temperature distribution obtained from the numerical study. The numerical results were validated with the experimental results with respect to the temperature distribution and with the measured crimped sample diameter. The model was also used to study the effect of the tapered andle of the field shaper, and it was found that with the increase in the tapered angle the efficiency of the field shaper also increases.

Table of Contents

भारतीय प्रौद्योगिकी संस्थान गुवाहाटी
Indian Institute of Technology Guwahati

List of Figures

List of Tables

भारतीय प्रौद्योगिकी संस्थान गुवाहाटी
Indian Institute of Technology Guwahati

1 Introduction

Motivation for environmental protection, responsibility and resources saving in the society influences the industrial manufacturing. For this reason, there is an increasing demand for lightweight manufacturing of automobiles and aerospace parts. For many years design based on multi-material was a well-known strategy which can be applied to weight reduction, higher production efficiency and cost reduction. Conventionally available techniques fail when it comes to joining of dissimilar material combinations having significantly different melting temperatures. In joining of dissimilar material combinations, they tend to form brittle intermetallic phases such. Joining of dissimilar materials by joining by forming can be an alternative for manufacturing the lightweight products.

1.1 Metal Forming

A type of manufacturing process in which metal undergoes a plastic deformation under suitable external load is known as metal forming process. This load can be applied either manually or through a machine. Conventional metal forming and high strain rate forming are the two broad classifications of metal forming process.

1.1.1 Conventional metal forming

In conventional metal forming a punch and a die system is used to deform the material into the required shape. The strain rate developed in the convention metal forming has typical value in the range of 0.1 to 5.0 s^{-1}. Rolling, forging, drawing, extrusion, coining, sheet metal forming, bending etc. are some of the typical examples of the conventional metal forming process.

1.1.2 High strain rate metal forming

The high strain rate metal forming processes are different from the conventional metal forming processes because in this process the workpiece is accelerated to high kinetic energy, which results in plastic deformation of the material. The strain rate in the high strain rate forming process is of the order of 10^3 s^{-1}. Some typical examples of high strain rate metal forming processes are explosive forming, electrohydraulic forming, and electromagnetic forming (EMF) process. In the last few years, there is an increase in interest to use aluminium to replace steel, especially in automobile sectors to reduce the weight of the automobile, which results in

an increase in the efficiency of the automobile. However, formability of aluminium is lower than that of steel due to low strain hardening coefficient. Also, springback of material is more severe in the case of aluminium as compared to steel due to low modulus of elasticity. The formality of aluminium can be improved by utilising high strain rate metal forming processes. Some of the typical high strain rate forming methods such as explosive forming, electrohydraulic forming, and EMF are discussed in the following subsections.

1.1.2.1 Explosive forming

The explosive forming process is a type of high strain rate forming process in which instead of punch chemical energy of explosives is used. Some of the commonly used explosives are trinitrotoluene, cyclonite, and pentolite. There are two types of explosive forming one is contact type and another is standoff type explosive forming. In contact type, the explosive is in contact with the workpiece while in standoff type the explosive material is placed at some distance from the workpiece and the workpiece is clamped over a die, and the assembly is placed into a container filled with water as shown in Fig. 1.1. As the explosive is detonated, a shock wave of the high-intensity pressure wave is produced in water. When the high-intensity pressure wave strikes against the workpiece, the metal is formed into the die. Explosive forming requires long setup time, and it is suitable for the production of unique, high volume products, high cost and has to be performed in remote area.

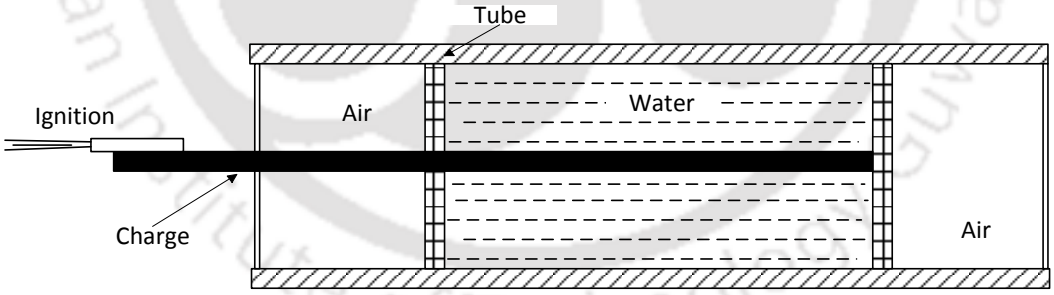

Fig. 1.1 Schematic of an explosive forming process

1.1.2.2 Electrohydraulic forming

Electrohydraulic forming is a type of high strain rate forming process in which electrical energy of the capacitor bank is converted into the mechanical energy. In this process, a high-frequency pulse current is passed through two electrodes placed apart in a container filled with fluid as shown in Fig. 1.2. The applied pulsed current electric vaporises the fluid around the electrode and creates a shock wave in the fluid. The developed shock wave moves away from the

electrodes towards the workpiece and when the shock wave impinges on the workpiece, it crates deformation [1].

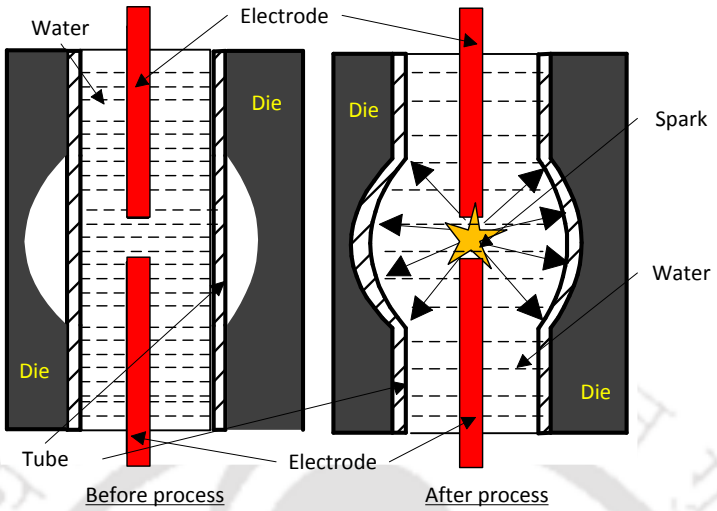

Fig. 1.2 Schematic of an electrohydraulic forming process

1.1.2.3 Electromagnetic forming

In EMF process, the capacitor bank is used to store the electrical energy and discharge energy to make a pulsed current to flow through the coil. In EMF, the coil replaces the punch as in conventional forming to get the desired deformation. The process of EMF is illustrated schematically in Fig. 1.3. The details of the EMF is discussed in the subsequent section.

1.2 Electromagnetic Forming

1.2.1 Principles of EMF

In principle, an EMF system consists of a capacitor bank, a conductive coil and the metallic workpiece to be deformed. The primary components of an EMF process with field shaper are shown in Fig. 1.3. The capacitor bank is connected to the forming coil, which is near the field shaper and workpiece. When the main switch is closed, the high current pulse passes through the forming coil and produces a transient magnetic field that induces eddy currents in the nearby metallic workpiece. The currents in the coil and metallic workpiece travel in opposite directions, according to Lenz's Law. The electromagnetic repulsion between the oppositely flowing currents, governed by the Lorentz force, provides the deformation force to the workpiece.

1.2.2 Components of EMF

Power supply, switch, capacitors bank, working coil, field shaper etc. are the main components of EMF system. The details of the main components are discussed in the following sub-sections.

1.2.2.1 Capacitors bank

Capacitors bank are used to store electric energy by charging the capacitors and produces a high-frequency and high-intensity pulse sinusoidal current by discharging the energy.

1.2.2.2 Forming coil

The electrical energy in the capacitors bank was converted into electromagnetic energy with the help of forming a coil, which is finally transformed to electromagnetic pressure on the workpiece. A high magnitude damped sinusoidal pulse current flows through the forming coil, which is a part of the RLC circuit. The high magnitude current produces the transient electromagnetic field necessary for the performance of the forming process. Forming coils are an essential part of any EMF process. Depending on the type of EMF process, different types of the forming coils were used such as a solenoidal coil, flat pancake coils, and bar coils [2].

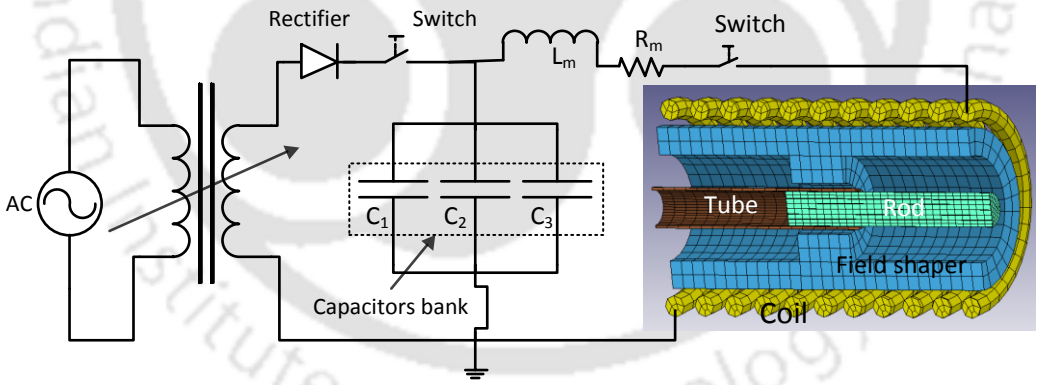

Fig. 1.3 Basic components of EMF process

1.2.2.3 Field shaper

To concentrate pressure at a definite location on the workpiece field shapers are used. They are also used to adjust large-diameter compression coils to smaller-diameter workpieces. The field shapers are single-turn coils and they are introduced between the workpiece and the coil. Field shapers receive energy from the working coil and transfer it to the workpiece by electromagnetic induction. Thus, by using different sizes of field shapers, the same working

coil can be used for different diameter of the workpiece. Field shaper must be electrically insulated from both the working coil and the workpiece. The usage of field shapers raises the life of the coil by dropping the force acting on the coil.

1.2.2.4 High-voltage switches

Very high-speed switches, capable of withstanding high voltages, are required for EMF operations. Ignitrons, spark gap switches, or rail gap switches are the examples of high voltage switches which can be used to close the RLC circuit and produce the high frequency damped current pulse in the forming coil.

1.3 Types of EMF

1.3.1 Sheet metal forming

In EM sheet metal forming process, rigid flat spiral pancake coil, is placed below the metal sheet which needs to be formed and then magnetic pressure is being applied with the help of pancake coil. The deformed sheet can take the shape of the die or can be a free bulged. By this means, there is a significant improvement in forming limit of metal sheet, which is not possible by the conventional quasi-static process [3].

1.3.2 Hybrid metal forming

In hybrid metal forming, the conventional forming operation is replaced with EM forming process. In this process, one or more coils are installed to obtain the deformation of the sheet inside a die which consists of complex geometry. Deformation is achieved by making use of localized force using tailoring the coil to get required magnetic pressure in the desired location, which is not possible by any other conventional forming process [4].

1.3.3 Tube forming

The EMF process is widely being used for axisymmetric components such as tube and cone etc., which have extensive use in industrial applications. In EM forming of the tube, the cylindrical tube is uniformly expanded or compressed by applying the electromagnetic force on the circumference of the tube. The Maxwell's equation is used to explain the working of EMF process.

1.4 Maxwell's Equations

The Maxwell's equations in the simplified version can be expressed by equations (1.1) to (1.4). In Maxwell's equations, equation (1.1) summarises the effects of matter plus Coulomb's law

of forces. The equation (1.2) represents an extension of Ampere's circuital law, the equation (1.3) proclaims Faraday's law of induction and equation (1.4) represents the non-existence of magnetic monopoles.

$$\nabla \cdot \vec{\mathrm{D}} = \rho \tag{1.1}$$

$$\nabla \times \vec{H} = \vec{J} + \frac{\partial \vec{D}}{\partial t} \tag{1.2}$$

$$\nabla \times \vec{E} = -\frac{\partial \vec{\mathrm{B}}}{\partial \mathrm{t}} \tag{1.3}$$

$$\nabla \cdot \vec{B} = 0 \tag{1.4}$$

where the vector functions $\vec{E}$, $\vec{D}$, $\vec{B}$, and $\vec{H}$ are known as

$\vec{E}$: Electric field (V/m)

$\vec{D}$: Electric displacement field (coulomb/m^2)

$\vec{B}$: Magnetic induction (Tesla)

$\vec{H}$: Magnetic field (A/m)

Some sources generate the electromagnetic field and those sources are

$\vec{J}$: Electric current density (A/m^2)

ρ : Electric charge density (C/m^3)

The electric current density and the electric charge density are related through the continuity equation which is given by equation (1.5).

$$\nabla \cdot \vec{J} = -\frac{\partial \rho}{\partial \mathrm{t}} \tag{1.5}$$

1.5 Lorentz Force

In Maxwell's equation we must add the Lorentz force law to have a complete description of the electromagnetic phenomena. Lorentz force law relates mechanics with electromagnetism and it can be given by equation (1.6).

$$\vec{f} = \rho(\vec{E} + \vec{v} \times \vec{B}) \quad (1.6)$$

where $\vec{f}$ represents the force density (N/m3) and $\vec{v}$ represents the velocity of the electric charge density (m/s). The electric charge density moving with velocity $\vec{v}$ can be expressed by equation (1.7).

$$\vec{J} = \rho\vec{v} \quad (1.7)$$

Replacing $\rho\vec{v}$ from equation (1.6), the Lorentz force can be expressed by equation (1.8).

$$\vec{f} = \rho\vec{E} + \vec{J} \times \vec{B} \quad (1.8)$$

The power per unit volume p (W/m^3) obtained by the Lorentz force can be given by equation (1.9).

$$p = \vec{f} \cdot \vec{v} = \rho(\vec{E} + \vec{v} \times \vec{B}) \cdot \vec{v} = \rho\vec{E} \cdot \vec{v} = \vec{E} \cdot \vec{J} \quad (1.9)$$

1.5.1 Lorentz force developed on a charged particle

The expression to find the electromagnetic force that developed on a charged particle is given by equation (1.10).

$$\vec{F} = q(\vec{E} + \vec{v} \times \vec{B}) \quad (1.10)$$

where $\vec{F}$ represents the total amount of force (N) developed on the charged particles.

1.5.2 Lorentz force developed on a flyer tube

The Lorentz force developed on the outer tube or flyer tube is unidirectional and it can be used to calculate the impulse developed on the base tube by equation (1.11) [5].

$$\text{Impulse} = 2\int F dt \quad (1.11)$$

1.6 Advantages, Limitations and Applications of EMF

1.6.1 Advantages of EMF

EMF has many advantages that make this process an alternative technique of conventional forming processes. Among all the high-speed forming techniques EMF is one of the most suitable techniques of plastic deformation. The main advantages of EMF process are mentioned below:

- Controllability and repeatability
- High-speed forming
- High repeatability
- Reliable and well suited to high-volume production
- Many combinations using dissimilar metals are possible
- Cold clad without heat-affected zone (HAZ)
- No need for filler materials
- Green process (no heat, no sparks, no smoke, no radiation)
- No distortion
- Clean process (no pre- or post-weld cleaning)
- High quality, very aesthetic and cleaner interface
- Maintains mechanical strength (typical joints are stronger than the parent material)
- High precision (single micron precision obtainable by adjustment of the magnetic field)
- All these advantages translate into significantly lower costs and much higher quality and productivity Simple Fixtures - No Moving Parts
- Non-specialized operators
- Automated nondestructive examination
- More bond length
- No melting or heat affected regions
- No subsequent heat treatments
- Not sensitive to material history
- Dissimilar alloys easier to join
- Crack susceptible alloys easier to join
- High production rate capability

1.6.2 Limitations of EMF

Besides having many advantages of the EMF process, there are some limitations of the process.

Different limitations of the EMF process are listed below:

- The cost of the equipment is also significant.
- The volume of the equipment is also large. Which required large area to keep the equipment.
- Due to high voltage and high current in the process special safety precautions are needed before working on the equipment.
- The high speed of the process requires higher safety requirements and precautions.
- Materials with excellent electrical conductivity can be formed easily, like aluminum, copper, low carbon steels etc. However, if the materials have low electrical conductivity it cannot be formed easily.
- For forming poor electrical conducting materials, an intermediate high electrical conducting materials is required.
- The higher thickness of the workpiece is difficult to form.

1.6.3 Applications of EMF

The demand for tubular components in current and future automotive, heat exchanger, boiler etc. require developing high-productivity, low-cost, and robust joining process for tube connections [6]. This technique can be practically applied to pipework joints used in refrigerators and air conditioning systems. In this technique the pressure resistance and the weld strength required at pipework joints could be obtained from plastic deformation of cores and by decreasing the weld interface [7]. In addition to above mentioned application EMW of tubes were also used in aerospace, automotive, nuclear applications and electrical industry.

Table 1.1 Applications of EMF [8]

Aerospace Industry	**Automotive Industry**
➢ The lining of ammunition control rods ➢ Components of fuel pumps. ➢ Tubular space frames ➢ Composites over wrapped pressure vessels	➢ Space frames drive shafts ➢ Reinforcing bands on oil filters ➢ Components of air conditioning ➢ Fuel filters ➢ Tubular seat components
Electrical Industry	**Nuclear applications**
➢ Cable ducts ➢ Electrical fuses ➢ Components of electrical motors ➢ Connectors to copper cables ➢ Coaxial cable termination joints	➢ Closing caps ➢ End closers of nuclear fuel rods ➢ Metal canisters ➢ Nuclear fuel pins

1.7 Research Objectives

The main objective of this study is to investigate the suitability of the EMC for joining the dissimilar materials. More specifically, the aims of this study can be summarized as follows:

a) To design and build a coil to generate intense and concentrated magnetic field which can be used to join two similar or dissimilar materials.
b) To design and develop a field shaper to increase the life of coil and to increase the concentration of magnetic field.
c) To find the optimum surface profile on the base to increase the strength and life of the joint.
d) To study the temperature generation in the working zone of the EMC process.

1.8 Structure of Thesis

This thesis is organized in seven different chapters. This chapter discusses from the background of the research topic to the aims of the research. Each chapter in this thesis ends with a brief summary outlining the achievements and findings that were established. The remainder of this thesis is organized as follows:

Chapter 2: This chapter covers the elaborated theoretical background and literature review of related research topics.

Chapter 3: This chapter covers coil design procedures and feasibility trials for tube to rod configurations.

Chapter 4: Effect of the base profile on the Copper-Steel joint strength in tension with stepped field shaper was studied in this chapter.

Chapter 5: This chapter presents the influence of the base profiles on aluminum-steel joint strength in tension as well in compression-shear with the tapered field shaper.

Chapter 6: This chapter gives details about three types of field shapers geometries and to study the effect of geometries of the field shapers on the joint strength.

Chapter 7: In this chapter, the study of the temperature generation in the working zone in EMC has been reported.

Chapter 8: In this chapter, the effect of the field shaper tapered angle on the performance of the field shaper was studied.

.----------*----------*----------.

2 Literature Review

The electromagnetic principles were used and demonstrated in EMF process. This process fulfils the needs involving forming as well as joining of dissimilar material which is difficult-to-weld material [8].

2.1 Electromagnetic Forming

Authors Chu and Lee studied the effect of field shaper geometry for electromagnetic sheet impact forming process and found that the Lorentz force developed was concentrated at the end region of the slit. They also stated that the direction of current on the other side of the slit was in the opposite direction, causes repulsion hence wider slit will reduce the energy loss. Therefore, by considering the Lorentz force distribution as well as electromagnetic repulsion an optimal slit width should be determined. Some components in the field shaper result in more homogeneous Lorentz force distribution, and hence impact velocity will be more [9].

Arezoodar et al. have studied numerically the influence of the four different types of field shaper namely *conical*, *cylindrical*, *concave*, and *convex* as shown in Fig. 2.1 and found that magnetic flux was increased if a single stepped convex field shaper replaced to an inclined stepped field shaper [10]. The effect of stepped field shaper in electromagnetic inside bead forming was analyzed by Chaharmiri and Arezoodar and found that magnetic pressure was increased by decreasing the effective length but radial displacement was maximum at an optimum effective length. Also marked that 21 % increased the peak value of the magnetic pressure than that of using only direct coil [11]. Inside bead forming carried out by Murakoshi et al. suggested that increase in the discharge energy and width of the bead leads to an increase in the bead height formation [12].

Similar work using three types of field shaper namely cylindrical, concave and convex were compared by Suzuki et al. for tube bulging and found that the geometry of field shaper and the capacitor energy was the controlling parameter of the amount of the tube bulging. Also revealed that field shaper has a significant role in increasing the life of the working coil [13].

Yu et al. have studied the application of field shaper in EMF and found that the larger the effective area of field shaper results in larger uniform force area and smaller the amount of magnetic pressure [14]. Yu et al. have also added that the magnetic pressure decreases with the increase of the relative diameter of the field shaper [15].

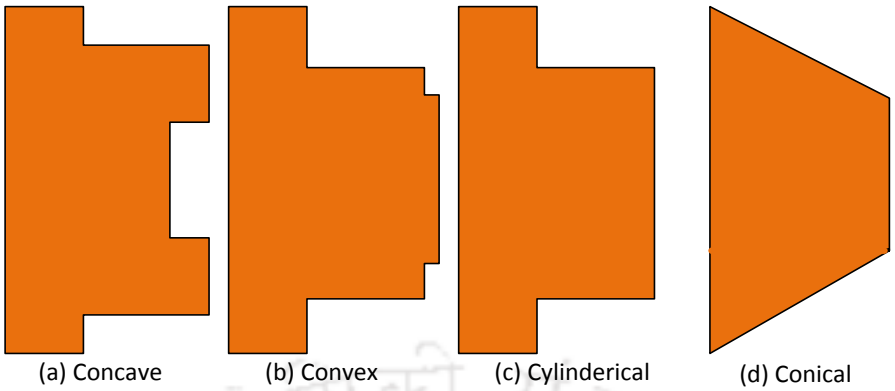

Fig. 2.1 Schematic diagram of the four different types of field shapers [10]

2.2 Electromagnetic Joining

To fulfil the desired weight reduction in engineering structures, a joining process is required which should have the ability to join dissimilar materials without additional mechanical elements, chemical binders or adverse influence of heat on the joining partners. The electromagnetic joining (EMJ) is an alternative to conventional thermal joining and mechanical joining process [16].

EMJ uses an electromagnetic force to accelerate flyer tube and collide against the base rod or tube with very high speed, resulting in a solid-state joint [17]. It is used for joining either homogeneous or heterogeneous material having different or same thicknesses [18]. It is a joining process in which lap joint surface of cylindrical components such as tubes, rods, and cones are joined together by using electromagnetic force [19]. EMJ is not only one of the most useful joining processes for the dissimilar metal joining for cylindrical components, but also a novel technology for metal joining using repulsive force on account of the interaction between electromagnetic part of working coil and current induced in an outer tube [20]. This process was invented for components with distinct geometries, by using the magnetic pressure to create reliable joints [21].

EMJ is a high speed, high strain rate, and high energy, impact joining process which has potential to significantly reduce weight and manufacturing cost, especially for joining cylindrical structures of similar or dissimilar materials. [22]. In such a short period, there is very less extent that the resultant joint will get heated [23]. In this method, no other pressurizing equipment is required, and it is a more straightforward process with the capability of joining within a microsecond. Therefore, this process can be employed as a technique which can be

applied to on-site tube work operations. This process is repeatable and depending upon collision velocity or discharge energy, the strength of the joint varies [24].

In EMJ of dissimilar metals and alloys, the temperature and heat negatively magnify the physical mismatch between material properties. The factors affecting the quality of joining are the discharge energy, the gap between the outer tube and inner tube or rod and thickness of an outer tube or flyer tube. The EMJ process greatly minimizes the problems of metallurgical incompatibilities between dissimilar metals and alloys.

The emergence of new joining techniques has great importance for the multi-material assemblies. EMC enables to join metals pairs with a substantial difference in their melting temperature using a high bonding pressure which can be achieved by an intense collision between the two parts to be joined [25]. This process covers joining of a broad variety of material combinations such as Al/Fe [25], Al/Ti, Ti/Ni, Cu/Manganin, Cu/Brass, Cu/Steel [26], Cu/Al, Al/Steel, Al/Mg, and Al/Ni.

2.2.1 Experimental studies on magnetic pulse cladding

Magnetic pulse cladding (MPC) technique was used by Yu et al. to form bi-metal tubes to achieved cladding of aluminum alloy (AA3003) on mild steel tube. The effect of geometry of the field shaper on cladding quality as well as other leading process parameters, such as, feeding size, radial gap and discharge voltage were investigated [19]. Mechanical property was evaluated by compression-shear test and a maximum strength of 79.2 MPa and an average of 29.7 MPa were obtained by the following process parameters settings: profiled field shaper, feeding size of 12 mm, radial gap of 2.0 mm and discharge voltage of 15 kV. Optical microscope (OM) and scanning electron microscopy (SEM) images showed smooth and small wavy integral interface. Energy dispersion spectrum (EDS) mapping revealed that the interfacial diffusion zone was up to 50 µm wide. The results showed that the proposed MPC process is able to form sound cladding bonds and could apply to a tubular clad component with a large axial length [19].

MPC technique was employed by Lee et al. to join the end closure of fuel pin made of ferritic-martensitic (FM) steel and oxide-dispersion-strengthened (ODS) steel. Rigid metallurgical bonding between the tube and end plug was obtained by high-velocity impact collision accompanied with surface jetting for a given set of optimal process parameters, e.g., the end-plug geometry. Joint region showed a typical wavy morphology with a narrow grain

boundary-like bonding interface. No local melting, was not observed and only the limited grain refinement was observed in the vicinity of the bonding interface without destructing the original reinforcement microstructure of the FM-ODS steel, i.e., a fine grain structure with oxide dispersion. No leaks were detected during helium leakage test, and moreover, the rupture occurred in the cladding tube section without leaving any joint damage during internal pressure burst test. All of the results proved the integrity and durability of the MP Clad joints and signified the enormous potential of this method of end closure joining for advanced fast reactor fuel pin fabrication [17].

The bi-metallic tube was fabricated by Fan et al. for engineering applications with an outer tubular component was structurally strong material and an inner tubular layer of corrosion-resistant material. Experimental arrangement of MPC process to produce an Al/Fe bi-metal tube with an outer carbon steel tube and an internal aluminum tube was made. Radial gap between the clad tube and the base tube significantly affect the bonding strength obtained from the impact-based operation. At 10 kV discharge voltage and radial gap of 1.7 mm, the optimum bonding strength obtain was 13.19 MPa [25].

2.2.2 Numerical studies on MPC

A novel approach was suggested by Fan et al. to fabricate bimetallic tube by using MPC of lapping portions of long tubes. An efficient numerical simulation of the MPC process to analyze the dynamic deformation and its effect on cladding result from a numerical view was presented. A 2D axisymmetric model was modelled and simulated a multi-steps cladding by forming based on the models similar to an actual MPC process. Predicted model results were compared with the experimental results by the contour of the clad tube and showed an acceptable agreement. The advantages of a new field shaper with tile angle $\alpha_1 \, of$ 3 and angle $\alpha_2 \, of$ 13° and the magnitude of the magnetic pressure, the stress-strain field and velocity of the collision were investigated [27].

2.2.3 Experimental studies on electromagnetic welding

The electromagnetic force was applied by Masumoto et al. for electromagnetic welding (EMW) aluminum tubes. The equipment used was a capacitor bank and coils of 10 turns were attached around the tubes. The test specimens taken were aluminum tubes and bars of similar or dissimilar metals and alloys and both tapered and straight cores. Although intermetallic compound layers similar to those in other welding processes were produced at the interface of welded zones, the thicknesses were minimal, 2 to 20 µm. Wavy patterns at the interface of the

welded zones which were similar to those in explosive welding were observed and it showed that such patterns were produced due to high-velocity collision between tube and core [28].

Tamaki and Kojima suggested the important factors which affect the result of EMW, and those factors were coil inductance, the clearance between the outer tube and core bar, the tapered angle of core bar, the thickness of the core when a tubular core is used, and hardness of outer tube. Welding was expressed by the ratio of welded length to interfacial length along the circumference. The results found could be summarised as follows: The optimum result of welding was obtained with a coil inductance of about 3 μH, the most suitable clearance was 3 mm, for the joint of straight core, and two welded zones were obtained near the ends of the coil. If the center of the coil as the tapered angle increased up to 8 degrees, welding was feasible for a tubular core, when its thickness exceeded about 6 mm. For constant energy input softer the outer tube easy will be the welding [29].

Aluminum specimens were welded by Kojima et al. consisting of a couple of tubes and cores by EMW process. Three types of core geometries were used: single-tapered-, concave- and convex cores. Effect of the tapered angle of the core on the width of welded zones were decided on the basis of the experimental results the distribution of collision angles in each joint, and the acceptable range of the joint was as follows:

- The position, width and number of welded zones can be controlled by the shape and tapered angle of the core.
- The optimum tapered angles are 12.5°, 17.5° and 7.5° respectively, for single-tapered-, concave- and convex cores.
- Two factors which decide the width of welded zones are the distribution of collision angles in the joint, and their acceptable values. Welded zones are produced in a series of positions whose collision angles meet those in the acceptable range.
- The tapered angle affects mostly the distribution of collision angles, but a little the range of acceptable ones [30].

MPW trials were carried out by Hokari et al. using aluminum and copper as outer tube and aluminium, copper, brass and mild steel for core materials. In this study, the voltage was varied and found that irrespective of the metal employed for the outer tube and the core, the optimum clearance between the tube and the core for welding was 0.5 mm for the shape, indicated in Fig. 2.2. For aluminium as a tube, a wide range of clearance is suitable and as a core the weld obtained at circumference was uniform throughout. Regular wavy pattern at the

interface similar to that of an explosion welded interface was observed. In addition, an increase in hardness was noted near the weld interface in both the tube and the core and work hardening was identified, due to plastic deformation [7].

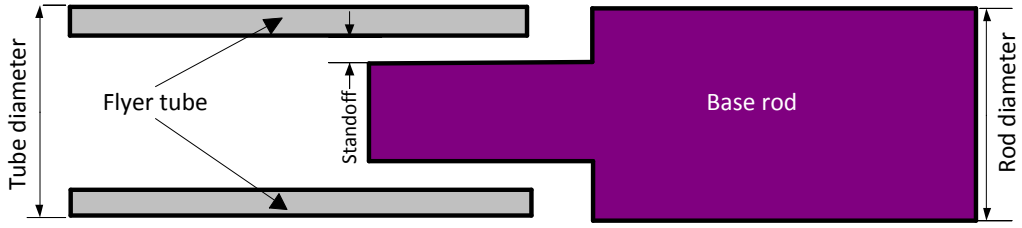

Fig. 2.2 Shape and size of the specimen used [7]

Stern and Aizenshtein investigated the microstructural features of the bonding zone in electromagnetic welds of similar and dissimilar metal pairs. The nature of the reactions and phase formation that occur in the electromagnetic joints displaying a discontinuous pocket type or a continuous transition layer along the bond interface regarding local melting followed by rapid solidification. The most significant feature of the transition zone created during the EMW process was an increase of hardness at the interface layer. For similar base metals, the main reason for the hardness increase was the fine-grained microstructure created during the rapid local solidification. In the dissimilar base metal welds, the increase in hardness was due to the formation of stable or metastable intermetallic phases and the fine-grained microstructure of the bonding zone [31].

Al 6061 tubes of 0.065 inch thickness to steel bars was joined by Kimchi et al. by using an MPW process. The width of the weld was found to be 1 mm to 2 mm. Optimum concentrator design and gap equal to half of thickness was a minimum criterion to achieved bond along the circumference. The receding angle on the base can promote and increase the weld quality, the receding angle used is shown in Fig. 2.3 [6].

With the EMW process Fe-Al intermetallic phases were formed by Marya et al. with limited interfacial heating. The strength of lap-joints is primarily related to the intermetallic layer thickness which has an optimum value of $4-6\ \mu m$ and the proportion of the Fe_3Al and Fe-Al phases [21].

The electromagnetic pressure was used by Faes et al. to deform, accelerate and weld workpieces in EMW. Experiments were performed to investigate the weldability of copper

tubes to brass solid workpieces. The tubes had an outer diameter and wall thickness of 25 mm and 1.5 mm respectively [32].

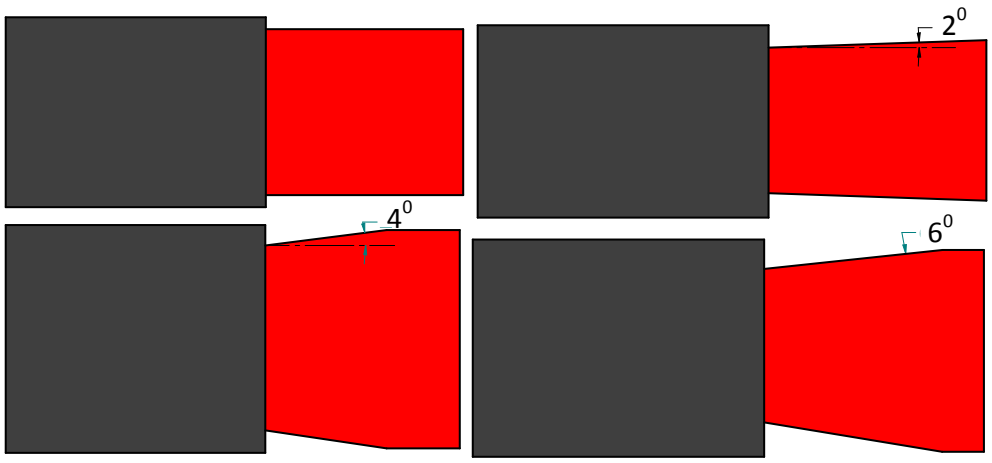

Fig. 2.3 Geometry of the inner steel rod with 0, 2, 4, and 6 degree receding angle

A multi-turn coil with five turns in combination with a field shaper to focus the electromagnetic flux and thus realise the high pressures needed for welding. The process parameters for joining these materials for maximum weld length was also optimized. The parameters taken into account where the position of the field shaper relative to the workpieces, the width of the air gap between the tube and the inner workpiece and the energy level. The weld quality based on metallographic examinations, scanning electron microscopy and hardness measurements were examined [32].

MPW machine was used by Zhidan et al. of 100 µF capacity to weld aluminium 3A21 tube of 20 mm outer diameter and 1 mm thickness with steel 20 tube of 16 mm outer diameter and 4 mm thickness by varying the voltage between 8 kV and 15kV. A wavy morphology with a wavelength of about 100 µm was observed at the welding interface. Al-Fe dissimilar tubes can be welded successfully with the optimum tapered angle of 4 degrees [33].

The weldability of aluminium alloy 6060T6 tubular assembly was developed by Raoelison et al. by using EMW technique. For bonding to be occur, the weld should able to undergo plastic deformation. The critical bonding is characterized by a straight bonded interface that breaks like an adhesive fracture. A zone of defectives weld formation at the high level of both charging voltage and gap was observed. The radial velocity of the flyer and its variation during the radial shrinkage were interpreted and found the convex shape of the welding range [34]. Yu et al. performed MPW for lap joining of AA3003-O and steel 20 tubes,

analyzed the mechanical properties, microstructure and interface pattern of welding. The tensile and torsional strength of weld was higher than aluminium tube for more than 8 kV of discharge voltage.

The impact velocity of the welding was studied by Zhidan et al. of Al–Fe heterologous pipe fittings by combining numerical simulation and technological test with the assistance of constitutive relations of 3A21Al alloy under a high strain rate. The momentary movement speeds were analyzed when the outer tube (Al) impacts the inner tube under four different voltages to obtain the critical voltage for welding inner and outer tubes. The speed of the welding points of the outer tube noticeably increased with the rise in the discharge voltage. The weld interfaces of both the inner and outer tubes produced regular zigzag waves when the impact velocity reached 350 m/s. The energy spectrum analysis revealed that pipes undergo severe deformation under high-speed impact, and the increased temperature enhances the activity of the atoms among other elements, thus producing a surface mass flow under strong impact and granulated substances [35].

For optimum process parameters or within an optimal range, Mousavi et al. found that welding will take place and wavy or transition bond could identify an optimal weld without any intermediate layer. This condition could be achieved when the collision velocity has a value greater than the transition velocity (the velocity at which waves start to form) and less than the sonic velocity of the workpiece or flyer [36]. The collision velocity has to impart the kinetic energy and fluid behavior for jet formation and should result in a collision angle corresponding to small wavy interface. Very high value of collision velocity causes interface melting.

Stern et al. focused their study on investigating that EMW was either solid state welding or fusion welding, i.e. any local melting and solidification would take place in the weld. There were massive plastic deformation take place on both of the workpieces. The welding was resulting due to high impact velocity accompanied by extreme local pressure and intense shearing deformation near the interface will take place. Finally, concluded that in the MPW of the Al/Mg couples, there were fusion zone containing equal quantities of both Al and Mg because of very close melting temperature. In the couples of Al/Cu and Al/Fe only Al were locally melted at low input energy and at high input energy for Al/Cu couples the interface temperature may exceeds the melting temperature of the Cu [37].

EMW technique was employed by Lee et al. to join the end closure of fuel pin made of ferritic-martensitic (FM) steel, and oxide-dispersion-strengthened steel (ODS). Rigid metallurgical bonding between the tube and end plug was obtained by high-velocity impact collision accompanied with surface jetting for a given set of optimal process parameters, e.g., the end-plug geometry. Joint region showed a typical wavy morphology with a narrow grain boundary-like bonding interface. Evidence of even local melting was not observed, and only the limited grain refinement was observed in the vicinity of the bonding interface without destructing the original reinforcement microstructure of the FM-ODS steel, i.e., a fine grain structure with oxide dispersion. No leaks were detected during helium leakage test, and moreover, the rupture occurred in the crimping tube section without leaving any joint damage during internal pressure burst test. All of the results proved the integrity and durability of the joints and signified the great potential of this technique of end closure joining for advanced fast reactor fuel pin fabrication [17].

Shim et al. experimentally studied the effect of process parameters on the MPW process and developed an empirical model. Using their model based on *Response Surface Method (*RSM*)* concluded that the gap between the inner and outer pipe has a strong influence on the quality of the joint [20].

2.2.4 Numerical studies on EMW

Shim and Kang modelled square working coil in ANSYS FEM software and found the distribution of electromagnetic force developed around the coil. The maximum electromagnetic force of 951 N was found at the centre of the coil and 503 N at the edge of the coil. The sin-waveform of decreasing vibration with a period of 25 μs was also measured [38].

A numerical model was developed by Shim et al. based on the algorithm shown in Fig. 2.4 to analyze the interaction between the outer part and the working coil using a finite element method for Maxwell equation's and solved using an ANSYS/EMAG code for MPW process. Experiments were also performed based on the same parameter which was used in the numerical model and was found a good agreement between them [39].

MPW of tubes were modeled by Guglielmetti et al. in two stages, in first stage constructed the magnetic model in the ANSYS finite element software and in the second stage mechanical model was coupled with the magnetic model in the ABAQUS [40].

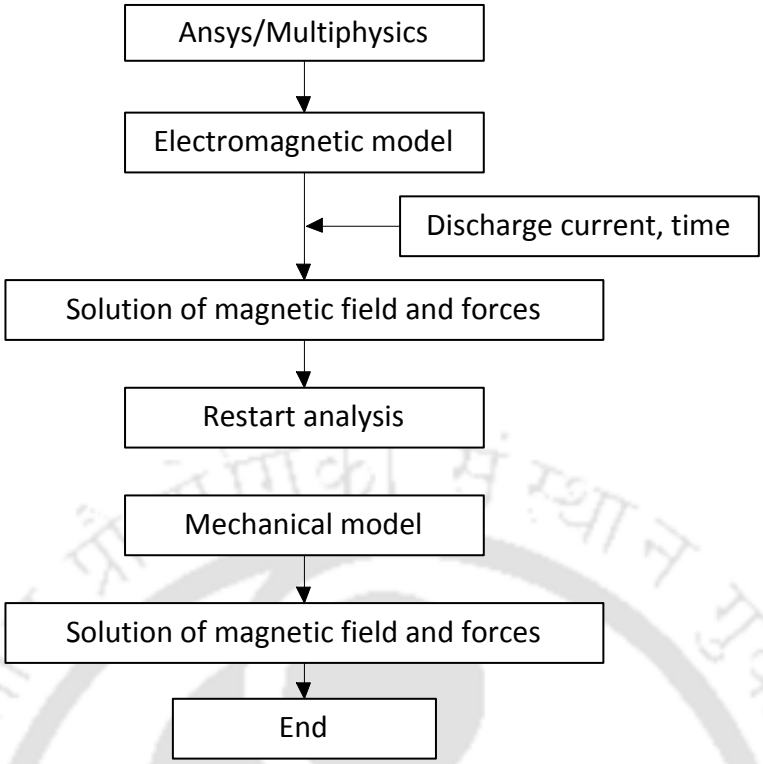

Fig. 2.4 Flow chart for the implemented algorithm [39]

Study of the magnetic model revealed that the principle parameters in the process were discharge current frequency, the tube-coil gap and the presence of the base tube. Higher discharge current and frequency with smaller gap was found to be the favorable condition for EM welding. Values of the above mentioned parameters were changed with the change in the material and geometry of the flyer and base tubes [40].

2.2.5 Field shaper design in EM joining

An efficient numerical simulation of the EMJ process to analyze the dynamic deformation and its effect on crimping result from a numerical view was presented [27]. There are in general two types of field shaper in common practice, one is constant cross-section field (C-field shaper) shaper, and another is profile field shaper (P-field shaper). P-field shaper can be obtained by modifying the geometry of the constant cross-section field shaper. The strength of the bond obtained through P-field shaper was more than that of C-field shaper EMJ. The schematic diagram of the constant cross-section and profiled field shaper reported by Yu et al. is shown in Fig. 2.6 [41]. Shim et al. have used the step-tapered field shaper for joining aluminum/steel pipe joint. The schematic of the process parameters used by the shim et al. is shown in Fig. 2.7 [39].

The EM joining was applied to the different shape of components such as cylindrical shape or flat shape, and also for several join configurations; half lap, overlap, cross lap, middle lap and end lap [42]. Zhidan et al. have performed numerical as well as experimental study for the impact velocity of Al tube in Al-steel pipe fitting by EMW. In this study, a rectangular coil as well as field shaper was used. For this study a high-speed camera system was used to measure the impact velocity of the flyer tube on to the base rod. It was found that the deformation of the tube first occurred in the centre where high electromagnetic field force was distributed, known as connection zone. Also observed that severe deformation in the tube at high-speed impact and for more than 200 m/s impact velocity the strength of the Al- steel joint obtained was more than that of the aluminum tube. A regular zigzag wavy structure at the interface was observed with a significant length and height if the impact velocity was more than the 355 m/s [43].

Wu and Shang used the step-tapered field shaper for EMW of Al tube on a copper rod. The effect of MPW conditions such as welding power, surface scratches, and contamination was studied and found that surface scratches in the tangential direction and higher applied power were results in a good weld, and oil on the surface was preventing the welding [44]. With this technique, a fast bond between two or more metals can be obtained as a result of a high-velocity impact of layers to be joined [45].

2.2.6 Variation in base rod geometry in EMJ

EMJ has one of the major application is in plastic metal forming in which electromagnetic field was used to create forming a force for joining [46]. Hammers et al. have studied the mandrel's surface effect on the mechanical properties of the joint. The mandrel's surface was varied by changing the materials of the mandrel. The increase in the stiffness of the materials led to an increase in the strength of the mechanical joint [47]. Bellmann et al. have studied the influences of different coating types on the steel for joining aluminum to steel. It was found that certain coatings improve the joint quality, some of them reduce the joint performance. Some coatings do not influence the joint quality [48].

Faes et al. have studied the groove filling for producing the axial form fit joints. Four different types of grooves used in the study is shown in Fig. 2.5. It was found that double grooved axial crimp joint providing a sufficient tensile strength in the formed form fit joints [49].

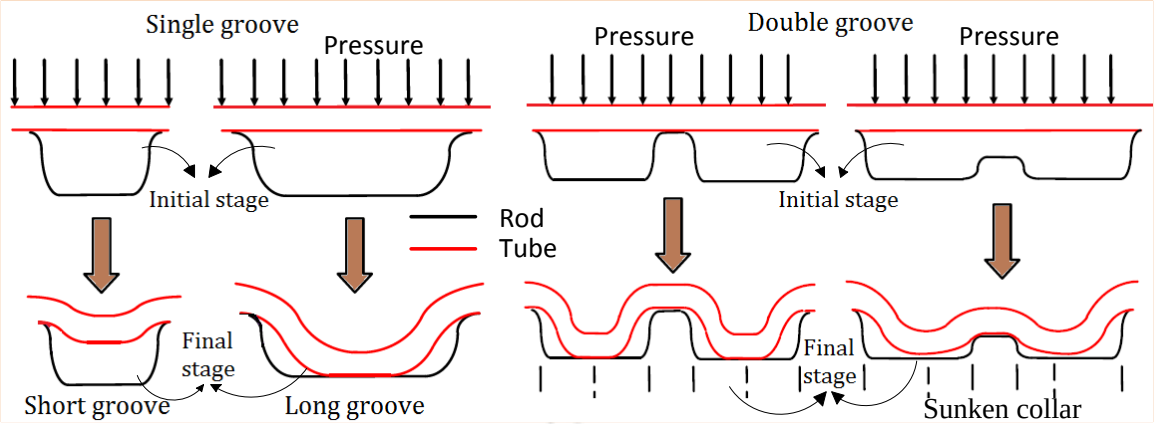

Fig. 2.5 Schematic diagram of the four different types of grooves created [49]

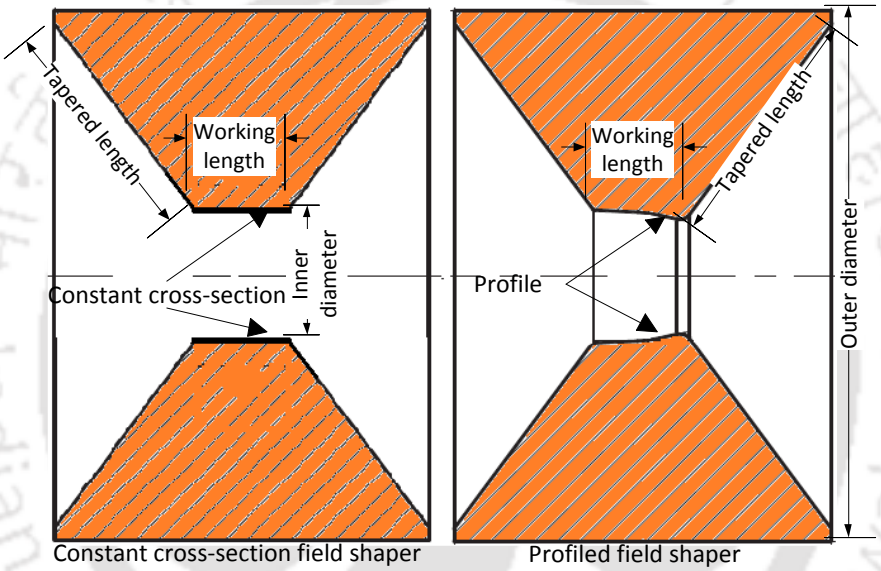

Fig. 2.6 Cross-section of constant cross-section and profiled field shaper [41]

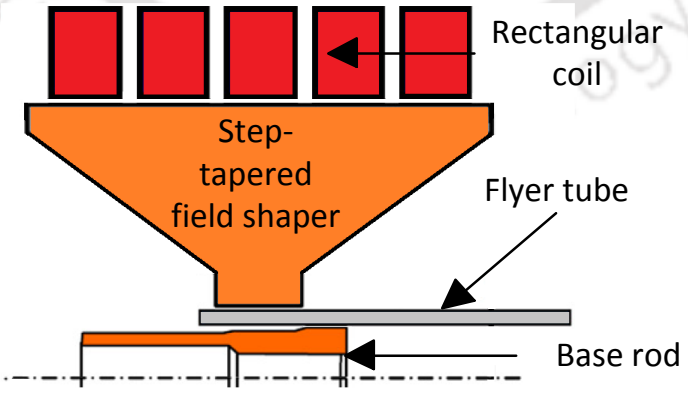

Fig. 2.7 Cross-section of step-tapered field shaper [39]

Faes et al. have produced form fit joints using EMJ technique and analyzed the effect of single and double groove on the joint strength. The width of the groove and the radial inward deformation of the tube was directly proportional. The radial deformation was increased with the increased in the discharge energy [49]. Weddeling et al. have reported the design principles related to the form-fit joints, and found that the joint strength was increased with narrower and deeper grooves [50]. Weddeling et al. have also reported that highest joint strength was obtained with the rectangular groove shapes [51].

2.2.7 Electromagnetic crimping

In technology, the wider use of steels has a significant obstacle because of the very poor corrosion resistance of steels. Hence, the prospective solution is to manufacture aluminum-steel bimetallic rods which will ensure increased corrosion resistance compared to homogenous steels [6]. Aluminum and its alloys have significantly higher corrosion resistance than steels. Hence, it can be expected that by producing a two-layered Al-steel rod the advantages of both the rods could be combined. The uniform tightness of the crimping aluminum layer on the perimeter and along the length of the steel core seem to be the key to the effective inhibition of the corrosion.

A bimetallic or composite rod is a cylindrical layered composite, having two or more than two metallic materials. Bimetallic rods combine the properties of two different metals in one rod such as corrosion-resistant, higher thermal, and electrical conductivity. Bimetallic rods were cost saving compared to the single metal rod and have different applications in the field of cryogenics, power generation, power transmission, overhead transmission conductor for electrical and electronics. The Copper-Steel combinations are frequently used because of their high electrical and thermal conductivity as well as high stiffness [7].

The joining of two or more different metals is important due to their various advantages. For example, a copper crimp aluminum rod is about 50 % lighter, 35 % cheaper and has conductivity equal to that of copper [52]. Hence, Copper-Aluminum composite components is a substitution for Cu components, result in both cost and weight reduction, and are highly relevant in industrial applications such as in the heating, electrical, and cooling applications [53]. Composite rods individually possess the distinct advantages of effective protection against the erosion or corrosion and increased mechanical strength because of their layered structure, where two or more different materials comprise the outer and inner layer [25]. The most important feature of the composite rod or composite sheet is the bonding or joining the

interface, either mechanically or metallurgically [26]. Electromagnetic crimped rods can be stock for manufacturing the wire rod, from which the bimetallic wire can be manufactured. By using an EMC technique, very good mechanical properties in the joints such as corrosion resistant and high-temperature resistance can be achieved. EMC is a cost saving, rapid and potentially reliable method which can replace conventional joining technique [54].

Fan et al. suggested a novel approach to fabricate bimetal tubes by using EMC of lapping portions of long tubes. The 2D axisymmetric model was modeled and simulated multi-steps are crimping by forming based on the models similar to an actual EMC process. Predicted model results compared with the experimental results by the contour of the clad tube and showed an acceptable agreement. The advantages of a new field shaper with tile angle $\alpha_1 \; of \; 3°$ and angle $\alpha_2 \; of \; 13°$ and the magnitude of the magnetic pressure, the stress-strain field and, velocity of collision were investigated [27].

An EMC technique was used by Yu et al. to form bi-metallic tubes by crimping of aluminum alloy (AA3003) on mild steel tube. The effect of various field shaper geometry, as well as other main process parameters, such as feeding size, radial gap and discharge voltage on the crimping quality and joint strength, were reported [19].

Fan et al. fabricated bi-metal tubfor engineering applications with an outer tubular component was structurally strong material and an inner tubular layer of corrosion-resistant material. Experimental arrangement of EMC process to produce an Al/Fe bi-metal tube with an outer carbon steel tube and an internal aluminum tube was made. Radial gap between the clad tube and the base tube greatly affect the bonding strength obtained from the impact-based operation. At 10 kV discharge voltage and radial gap of 1.7 mm the optimum bonding strength obtain of 13.19 MPa was observed. Bonding strength of the joint obtained by the crimping process were increase with the increase in the value of discharge voltage [25].

2.3 Parameters of EMF

To explain the effects of various process parameters, a simplified description of the process can be made by combining different equations, starting with the Newton's second law, which is going to describe flyer tube motion as a function of the time and different forces developed during the entire process and it is expressed by equation (2.1).

$$m\frac{d^2h}{dt^2} = F_m - F_\sigma \qquad (2.1)$$

In the above equation, m is the mass of the moving workpiece or flyer tube, h is the gap separating the two workpiece, F_m is the induced magnetic force (which is the product of magnetic pressure and external area of the outer workpiece), and F_σ is the force induced by accelerated workpiece as it resist deformation and this force is described by the equation (2.2)

$$F_\sigma = 2\sigma . n l_w r \tag{2.2}$$

In the above equation, σ is the plastic flow stress of the moving workpiece material or flyer tube i.e., its strength in N/m^2 or Pa, l_w is the length of its deformed area (in m), and r is the either inner or outer radius of the moving workpiece or flyer tube (those best applied). Here, σ represents the strength of the flyer tube in uniaxial condition, as well as it includes the dependency on the strain rate and strain hardening [55]. The various process parameters of EMF process includes the discharge energy, discharge current, standoff distance, magnetic pressure, collision velocity etc. These process parameters were discussed indetail in the following subsections.

2.3.1 Discharge energy

Stored energy in the capacitor bank was discharged into the coil and within few micro seconds the flyer accelerates and gets impact on the second part with very high velocity. Discharge energy could be increased by increasing the charging voltage or capacitance of the capacitor bank and thus shearing strength of the welds will also enhance [56]. The value of discharge energy can be calculated by the equation (2.3):

$$E = \frac{1}{2} C {V_0}^2 \tag{2.3}$$

where, V_0 represents charging voltage, E represents energy stored in the capacitor bank and C represents capacitance of the capacitor bank [7]. The impulse energy per unit area at the instant when the outer tube impacts with the inner tube or inner rod with velocity (v) and acceleration (a) is obtained using the equation (2.4). The percentage reduction in the cross-section of the workpiece can be calculated from the equation (2.5).

$$e = \frac{mv^2}{2} + \frac{\lambda m^2 a^2}{2E_0} \tag{2.4}$$

$$\text{Reduction of cross section} = \frac{S_0 - S}{S_0} \times 100\ (\%) \tag{2.5}$$

where e represents impulse energy per unit area, v represents outer tube impulse velocity, m represents mass per unit area of the outer tube, E_0 represents elastic constant of the outer tube, λ represents constant, a represents impulse acceleration, S_0 represents area of cross-section of the core prior to welding, and S represents minimum area of cross section of the core after welding [7].

2.3.2 Discharge current

The variation of the discharge current with the time is shown in Fig. 2.8. The frequency of the discharge current decreases from maximum to zero with the time. Initially the frequency of the discharge current was maximum and it comes to zero after about 450 μs. The peak value of the discharge current was useful for either welding or cladding process and the other value of the discharge current was useless and by removing those frequencies could increase the life of the coil or field-shaper used in forming process [2].

The discharge current curve can be expressed by the mathematical relation given by equation (2.6) as:

$$I(t) = \frac{V_o}{\omega L}\, e^{-\beta t} \sin(\omega t) \tag{2.6}$$

where V_o represents the initial discharge voltage, β is the damping factor or exponent, ω is the angular frequency and L is the equivalent inductance of a circuit in the system [22].

The maximum current produced by a capacitor bank is directly proportional to the charging voltage and the square root of the capacitance (C), and also inversely related to the square root of the inductance (L_a) [2]. Mathematically, the peak current produced can be expressed by equation (2.7).

$$I_{max} = V_o \sqrt{\frac{C}{L_a}} \tag{2.7}$$

2.3.3 Standoff distance

The distance between parts before the discharge is termed as standoff distance or gap, and for higher gap, the discharge energy should be high. The gap between parts help to gain velocity and to acquire kinetic energy, it should be optimum value and if its value was low, collision

will take place before the flyer speed could reach the maximum value, also if its value were higher than then the speed of flyer reduces from the maximum at the time of collision. The variation in the standoff distance reduces the velocity as well as kinetic energy and hence reduces the shearing strength and width of the joint.

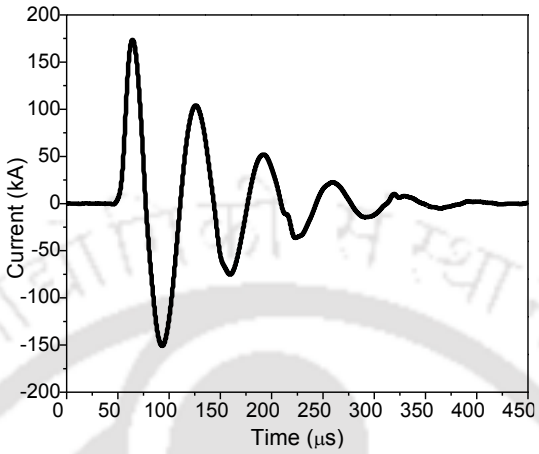

Fig. 2.8 Discharge current in EMF process

2.3.4 Magnetic pressure

Due to eddy current magnetic pressure is developed on the flyer tube and for successful bond the magnetic pressure must be high, otherwise flyer tube will impact to the base tube with lower velocity and no bonding will occur. For a constant gap between flyer tube and base tube the tensile shear strength of the joint will increases if the magnetic pressure will increase. When the gap increases, the discharge energy has to increase, to increase the magnetic pressure for better quality of the bond. Expression for magnetic pressure was studied by Shim et al. [39] can be given by equation (2.8)

$$P = \frac{B^2}{2\mu} \tag{2.8}$$

Moreover, due to this magnetic pressure the force developed on the flyer tube were determined by using equation (2.9) [39]

$$F = \frac{SB^2}{2\mu} \tag{2.9}$$

where *P* represents magnetic pressure, *B* represents magnetic field density inside the coil, *F* represents mechanical force acting on the cylindrical tube, and μ represents magnetic permeability and *S* represents minimum area of cross section of the core after welding.

The magnetic pressure generated due to eddy current pulse through the coil of tubular shape can also be expressed by equation (2.10) [57].

$$P = \left[\frac{\mu_0 C K^2 n^2 V^2 sin^2(\omega t) e^{\left(-\frac{Rt}{L}\right)}}{2L{l_w}^2}\right] \tag{2.10}$$

where *P* is magnetic pressure created by inductive current pulse (approx.), μ_o is the magnetic permeability of free space ($\mu_o = 4\pi \times 10^{-7}\ N\ A^{-2}$), *K* is coefficient depends on the physical dimension of the coil, *n* is number of winding of the coil, *R* is total electrical resistance of the discharge circuit, *C* is the total capacitance of the capacitor, *L* is the inductance of the unit, l_w is working zone length of the coil and *t* is the time [57]. Magnetic pressure *P* was calculated by using the analytical equation (2.11) and it was given by equation (2.11), where n the number of coil turns, l_s coil length, and k the coupling factor between the primary and secondary currents [58].

$$P = k\frac{\mu_o n^2 I^2(t)}{2l_s^2} \tag{2.11}$$

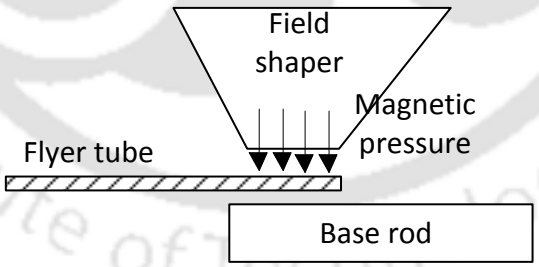

Fig. 2.9 Magnetic pressure on the outer tube caused by the field shaper

2.3.5 Collision velocity and collision angle

Collision velocity and collision angle between flyer tube and the core was an essential factor which governs the feasibility of high energy rate welding process. An optimum collision angle requires minimum welding energy [7]. The microstructure and properties of the weld interface will vary as the gap and collision velocity increases, the interface becomes wavy and an intermetallic layer forms. Joining is achieved preliminary in the central parts of the lap joint,

where the discontinuous thin material layers without any crack will form. In the terminal part of the welds, the collision velocity and resulting interface heating is sufficient to crack the intermetallic phases. In a tube-to-tube weld the velocity vector is oriented perpendicular to the surface for high-velocity collision to occurred [21].

Impact velocity is one of the major factors which decide the occurrence of weld and/or formation of a wavy interface in the welded zone. Published literature suggests an analytical relation to calculate the minimum velocity of impact required for the weld occurrence for similar material combination [24]. The relation was given by equation (2.12):

$$v_{i_{min}} = \sqrt{\left(\frac{\sigma_{TU}}{v_s}\right)} \tag{2.12}$$

where $v_{i_{min}}$ the minimum impact velocity required for successful welding to occur, σ_{TU} was the ultimate tensile stress (MPa) and v_s was the bulk sound velocity (m/s).

The high velocity of flyer metal plays an important role because it will create a jet that will remove any oxidation particles or, contaminants from both the surfaces and produces sound weld having excellent strength. The uniform pressure electromagnetic actuator was an innovative tool which was used by Raoelison, et al. to predict the workpiece velocity by taking into account the input energy, equipment and set up property as well as mechanical properties of the workpiece [34].

The relation between collision pressure and impact velocity is given by equation (2.13).

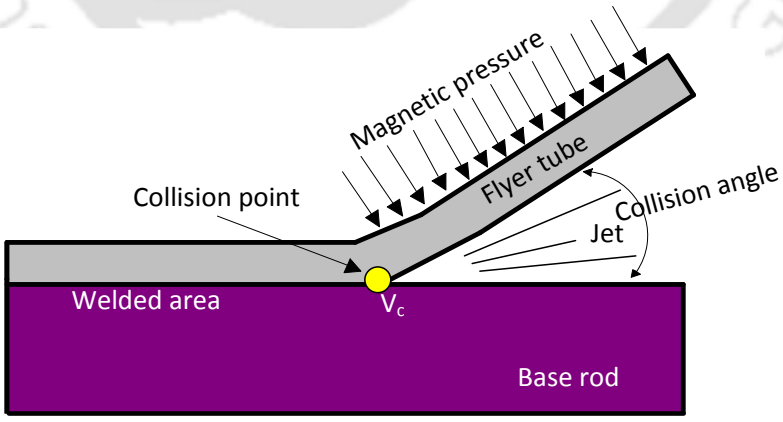

Fig. 2.10 Parameters in EMW [59]

$$P = \frac{\rho_1 \rho_2 C_1 C_2}{\rho_1 C_1 + \rho_2 C_2} v_i \tag{2.13}$$

where P represents collision pressure, ρ represents material density, C represents longitudinal wave speed, and v_i represents impact velocity

2.3.6 Damage initiation and damage evolution

The maximum nominal stress criterion was used by Raoelison et al. to evaluate the damage initiation, if t_n is the nominal stress in the direction normal to the interface, and t_n^0 is the peak value, t_s & t_n are the nominal stress in the first and second shear direction, t_s^0 & t_t^0 are their respective peak value then according to maximum nominal stress criterion [57] –

$$\max\left\{\frac{t_n}{t_n^0}, \frac{t_s}{t_s^0}, \frac{t_t}{t_t^0}\right\} = 1 \tag{2.14}$$

The relation for damage evolution using a criterion of energy dissipation due to failure was calculated by Raoelison et al. [57]. Damage evolution is a scalar quantity and it is a function of the effective displacement at the interface.

$$D = \frac{\delta_m^f(\delta_m^{max} - \delta_m^o)}{\delta_m^{max}(\delta_m^f - \delta_m^o)} \tag{2.15}$$

In the above expression δ_m^{max} was the maximum value of the effective displacement reached during the loading, $\delta_m^o$the effective displacement at damage initiation and δ_m^f the effective displacement at damage initiation at complete failure which is a function of the fracture energy –

$$\delta_m^f = \frac{2G^c}{T_{eff}^o} \tag{2.16}$$

where t_{eff}^o stand for the effective traction at the damage initiation and G^c the fracture energy or the input damage parameter to describe the damage initiation [57].

2.3.7 Measurement of strain distribution and plastic work

Welding of Al as flyer tube and Cu as base core was obtained by Wu et al. and the average strain components was calculated in hoop, thickness and axil directions based on the equations

(2.17), (2.18), and (2.19) respectively. In these equations *d(x), t(x), A(x)* was deformed tube outer diameter, thickness and cross sectional area at *x*, d_0, t_0, A_0 represents initial tube outer diameter, thickness and cross-sectional area, [44].

$$\varepsilon_\theta = \ln\left[\frac{d(x) - t(x)}{d_0 - t_0}\right] \tag{2.17}$$

$$\varepsilon_t(x) = \ln\left[\frac{t(x)}{t_0}\right] \tag{2.18}$$

$$\varepsilon_x(x) = \ln\left[\frac{A_0}{A(x)}\right] = \ln\left[\frac{(d_0 - t_0)t_0}{\big(d(x) - t(x)\big)t(x)}\right] = -(\varepsilon_\theta + \epsilon_t) \tag{2.19}$$

where $\varepsilon_e(x)$ represents true effective von-Mises strain at *x* was calculated by using the equation (2.20) where $\varepsilon_t(x)$ represents true strain component in the thickness direction at *x*, $\varepsilon_x(x)$ represents true strain component in axial direction at *x*, and $\varepsilon_0(x)$ represents true strain component in hoop direction at *x* [44]

$$\varepsilon_e = \sqrt{\left[\frac{2}{3\big(\varepsilon_x^2 + \varepsilon_\theta^2 + \epsilon_t^2\big)}\right]} \tag{2.20}$$

where *w(x)* is the work done per volume at *x* = effective stress × effective strain, [44]

$$w(x) = \int_0^{\varepsilon_e} \sigma_e d\varepsilon_e \approx Y\varepsilon_e(x) \tag{2.21}$$

In equation (2.22) *Y* is the mean of yield strength and ultimate strength used as the ideal work without considering strain hardening and strain rate effect on the flow stress The total plastic work *W* of entire deformation zone was obtained by further integrating the unit energy per volume w over weld zone volume *V* over the *x* range [a, b] [44]

$$W = \int_a^b w(x)A(x)dx = \int_a^b \pi[d(x) - t(x)]t(x)\,Y\varepsilon_e(x)dx \tag{2.22}$$

2.4 Gaps in Literature

After a literature review, a finite literature gap was found, which can be studied to increase the effectiveness and quality of the process. The gaps found which was not reported in the literature and can be used to study are as follows:

- Selection of solenoid coil parameters such as coil length, wire diameter, inner coil diameter, coil pitch, stand-off distance, etc. for designing of the solenoid coil.
- Effect of surface profiles created on the rod to increase the joint strength in tension or compression.
- Only a few kinds of literature were reported based on a numerical study of field shaper due to complexity in the simulation. Numerical simulation becomes difficult due to double mutual interaction, i.e., mutual interaction between coil-field shaper and field shaper-workpiece.
- Experimental and numerical comparison among different type of field-shapers such as tapered, step-tapered and stepped.
- Numerical and experimental study of heating in the coil or tube during the EMC process.

.----------*----------*----------.

3 Electromagnetic Crimping of Tube on Rod

OVERVIEW

The EMC is a high energy, high strain rate, high velocity and green materials joining or surface coating technique. Joining of dissimilar materials was very difficult because their physiochemical properties are seldom compatible or similar. Therefore, this type of solid-state joining technique can be an alternative for joining dissimilar materials. In present work, composite rods were produced by the EMC technique, which was characterized by a uniform distribution of the flyer tube on the base rod perimeter. The materials used were Al 1050 as flyer tube and dual phase steel as a base rod. Numerical simulations were carried out for finding out the optimized parameters for crimping and then experiments were conducted on the optimized parameters. The results obtained from the simulations revealed that for the successful crimping minimum value of collision velocity, plastic strain, electromagnetic pressure, and stand-off distance must be maintained. With the same optimized parameters and dimensions used in the simulations, experiments were conducted. The post process current obtained from the simulations and first peak of the discharge current measured in the experiments was compared. The variation in the maximum value of discharge currents in simulations from the experimental values was found to be 2%, 3% and 7% at 2.5 kJ, 2.6 kJ and 2.9 kJ of discharge energy. The outer diameter of the successfully crimped samples was measured and compared with the outer diameter obtained from the simulations and found a maximum of 6.6 % variation in the simulation value from the experimental value. The optical microscope image was analyzed and it was found that the Al-tube was crimped on the dual phase steel rod with a negligible gap. Further pull-out tests and hardness tests at the interface were performed to test the strength and hardness of the joints respectively.

3.1 Physics and Principle in the Process

EMC is mainly governed by three physical effects:

- As per *Faraday's law*, a changing magnetic flux in a closed loop, develops a time varying current in the loop, as long as the magnetic flux keeps changing.
-

- *Lenz's law* states that the inductive current has always tended to oppose the change in the magnetic field inducing it and hence produces an opposing current in the coil.
- Two opposite direction currents always repel each other with the *Lorentz's Force.*

The electromagnetic processing system consists of an AC power supply unit, switches, capacitor bank, and coil tool. Different components associated with the EMC unit are shown in Fig. 3.1. In the Fig. 3.1, C_1, C_2 and C_3 are the capacitance of the three capacitors, L_m and R_m are the inductance and electrical resistance of the machine L_c and R_c are the inductance and electrical resistance of the coil and L_w and R_w are the inductance and electrical resistance of the workpiece respectively. Coil tool is the actual tool, with the help of which magnetic pressure is being generated on the flyer tube. In Fig. 3.1, M represents the mutual inductance of the current from the coil to the workpiece. The current flowing in the primary and secondary circuit are coil current ($I_c(t)$) and workpiece current ($I_w(t)$). There are two switches, switch A and switch B in the circuit, shown in Fig. 3.1.

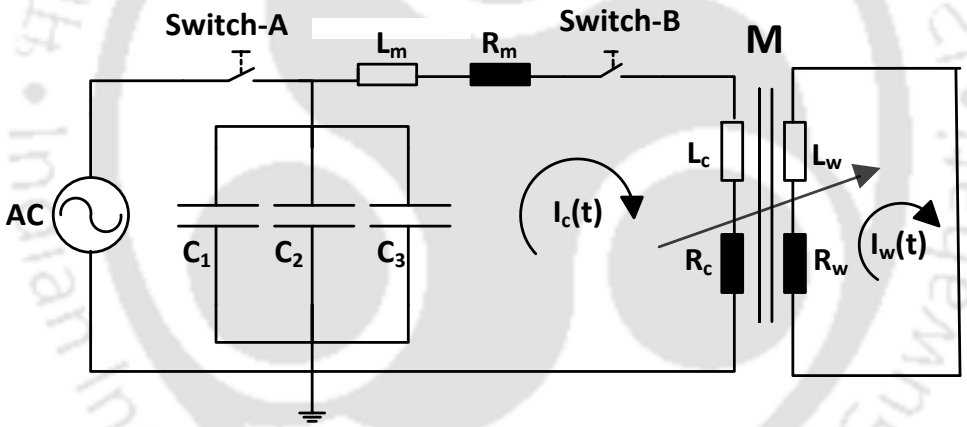

Fig. 3.1 Circuit diagram of the EMC process

The complete setup of the EMC system is shown in Fig. 3.2. The setup is consists of the working zone, control unit, digital oscilloscope, Human–Machine Interface (HMI) control, and a capacitor bank. The multi-turn coil was made of Copper-alloy with 99 % purity. The discharge current from the capacitor bank passes through the circular cross-sectioned solenoid coil having an outer diameter of 5 mm and then an eddy current was induced in the field shaper.

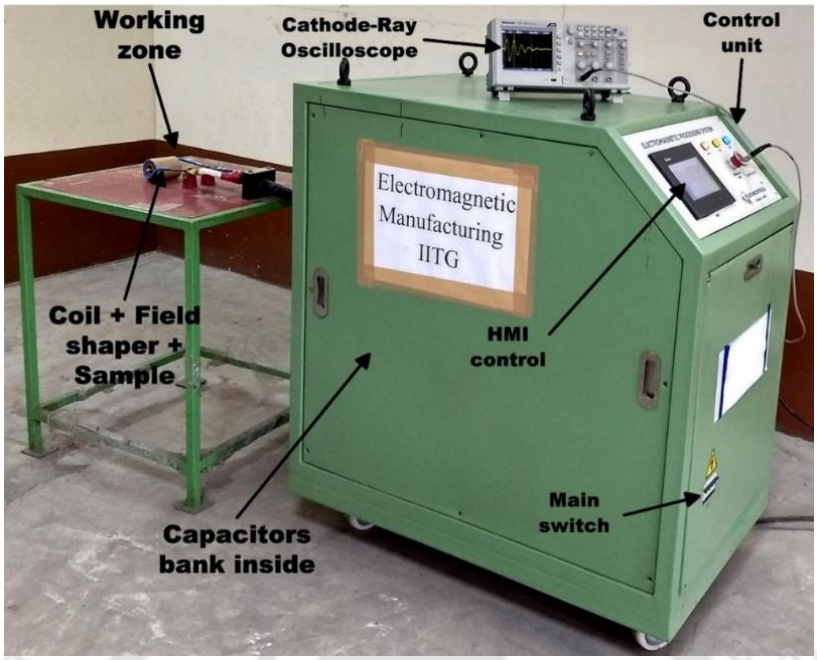

Fig. 3.2 Experimental setup used in EMC

The physics in the process can be explained by an example of the EMC of tube-to-rod, shown in Fig. 3.3. A metal tube is placed coaxially inside a solenoid coil, which is connected with a capacitor bank by a high voltage switch. The capacitor is charged to an initial voltage and when the switch is closed to complete the circuit, a sinusoidal damped current is produced. This current generates a transient alternating magnetic field about the coil; consequently, inducing an eddy current in the flyer tube. The current in the coil and the workpiece flow in opposite directions obeying Lenz's law and repel each other [60].

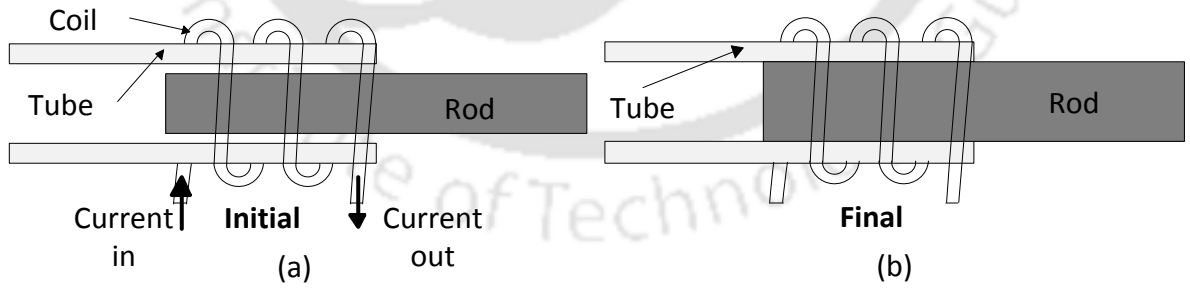

Fig. 3.3 Schematic diagram of EMC process (a) before and (b) after crimping

In this process, joining is achieved by a pressure joining using only electromagnetic force. The electromagnetic force developed on the outer tube causes it to be compressed and shrunk. Thus pressure joining is carried out by high-speed impact with the metal core positioned inside the outer tube [7].

3.1.1 Finite element method

For problems where the strain rates vary over a large range, the Johnson Cook strain-rate sensitive plasticity model was used. Thermal effects and thermal damages were ignored in this simplified Johnson Cook materials model. Since thermal softening is not available which is very significant in reducing the yield stress under adiabatic loading there is limited maximum stress. As a result of the simplifications related to thermal softening and thermal damage, this model is 50% faster than the full Johnson Cook materials model. To compensate for the deficiency of thermal softening, limiting stress values are used to keep the stresses within reasonable limits.

Constants in this equation for materials Al tube and dual phase (DP) steel rod is given in Table 3.1. For electromagnetic simulations the model was simulated for different values of discharge voltages, ranging from 6.8 kV, 7.0 kV, 7.1 kV, 7.4 kV, 7.7 kV, and 8.0 kV.

Table 3.1 Values of Johnson Cook material constant parameters

Materials	A (MPa)	B (MPa)	n	C	T_m (K)	m
Al 1050 [61]	110	150	0.4	0.01	918	1
DP Steel [62]	430	823.6	0.5	0.08	1048	0.6

3.2 Experimental Detail

The EMC was carried out by using a maximum of 10 kJ rated energy and 15 kV rated voltage electromagnetic processing system. In this section, the types of materials used, the initial input conditions, and the input load which was the discharge current were discussed in detail.

3.2.1 Materials and method

EMC of Al 1050 tube (tube dimensions: 17 mm outer diameter, 0.6 mm thickness and 40 mm length) to dual phase steel rod (rod dimensions: 15 mm outer diameter and 40 mm length) was performed using an Electromagnetic processing system with a maximum charging energy of 10 kJ and voltage of 15 kV. The total capacitance of the capacitors equals 90 μF. Fig. 3.4 shows the overlap configuration and corresponding dimensions of the Al tube and DP steel rod in the helical coil. The Al tube is called the flyer tube and is located just below the coil conductor. The DP steel rod is called base rod. The stand-off distance is the distance by which the Al flyer

tube is separated from the DP steel base rod prior to the discharge. The overlap is the distance between the spiral coil and the Al flyer tube. The mechanical properties of the tube and rod are listed in Table 3.2 and their chemical compositions are listed in Table 3.3.

Table 3.2 Mechanical properties of the materials used in the study

Materials	**Ultimate tensile strength (MPa)**	**Yield tensile strength (MPa)**	**Elongation at break (%)**	**Density (Kg/m^3)**	**Speed of sound (m/s)**
DP steel	650	465	26.3	7870	-
Al 1050	244	217	8.85	2705	3100-6400

Table 3.3 Chemical composition of the materials used

Materials	**C (%)**	**Fe (%)**	**Mn (%)**	**Si (%)**	**Al (%)**	**Ti (%)**	**V (%)**
DP steel	≤ 0.14	≥ 97.86	≤ 1.6	≤ 0.40	-	-	-
Al 1050	-	≤ 0.40	≤ 0.1	≤ 0.25	≥ 99.5	≤ 0.1	≤ 0.1

3.2.2 Process conditions

In the simulations, the discharge energy was varied from 1.0 kJ to 2.9 kJ. The stand-off distance was fixed throughout the study and it was taken equal to 0.4 mm about half of the thickness and overlap distance was taken as 15 mm.

The lap configuration joining of the samples can be achieved in three ways such as middle joint, left end joint and right end joint. In middle joint configuration, the tube was compressed at other than the end of the tube but in the end joint, the tube was compressed at the end position. In this study the lap configuration obtained was left end joint. The input load applied in the EMC is the peak value of the discharge current. Mainly the first peak of the discharge current was responsible for the deformation of the flyer tube which causes joining with the base rod.

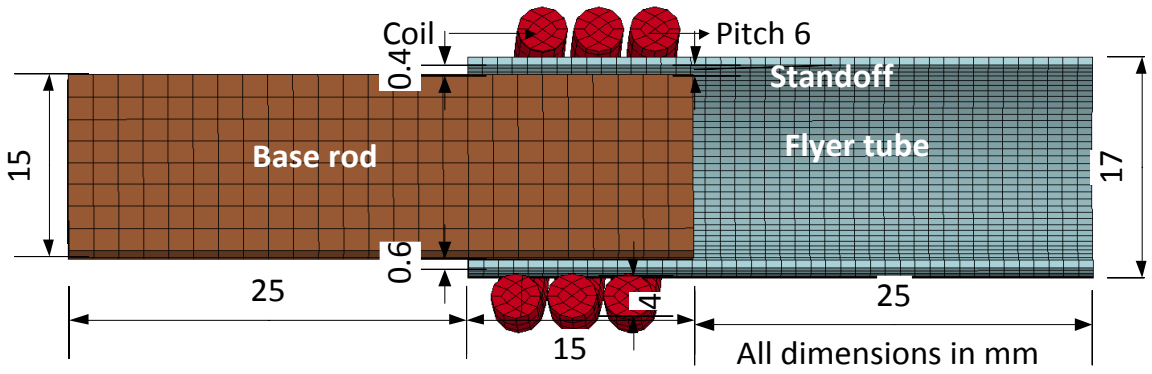

Fig. 3.4 Dimensions of the copper coil, Al tube and DP steel rod sample

Discharge current at different energy was measured by using Rogowski coil and oscilloscope. Fig. 3.5 shows the discharged current curve and Fig. 3.6 shows the first peak of the discharged current measured during the experiment at different discharge energy. The load in the electromagnetic module, i.e., the pulse of current which passes through the coil and this current can be expressed by the equation (3.1) [63]

$$I = V_o \sqrt{\left[\frac{C}{L} e^{-\beta t} \sin(\omega t)\right]} \tag{3.1}$$

where V_o is the initial discharged voltage, β is the damping factor or exponent, L is the equivalent inductance of the circuit in the system [24], C is the total capacitance of the capacitor bank, and ω is the angular frequency.

The damping coefficient can be calculated by using the equation (3.2) and the angular frequency of the current can be calculated by equation (3.3).

$$\beta = \frac{R}{2L} \tag{3.2}$$

$$\omega = \sqrt{\left(\omega_o^2 - \beta^2\right)} \tag{3.3}$$

where ω_0 is the initial angular frequency and it can be calculated by equation (3.4) and R, L, C are the electrical resistance, inductance, and capacitance of the circuit respectively [22].

$$\omega_o = \frac{1}{\sqrt{LC}} \tag{3.4}$$

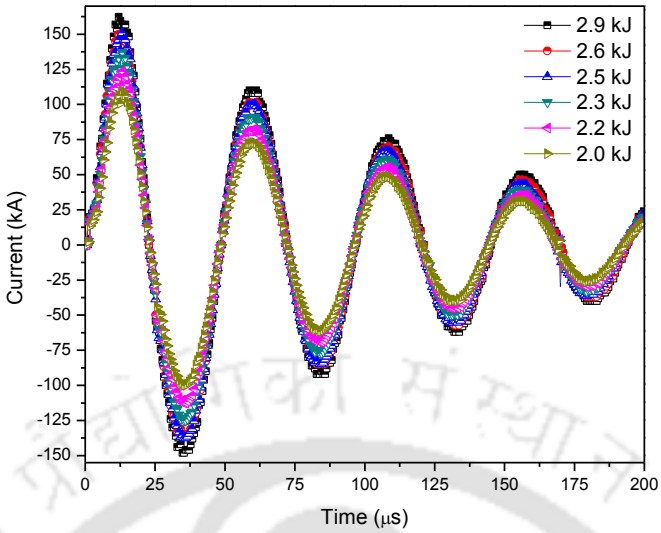

Fig. 3.5 Discharge current curve obtained from the experiment

3.2.3 Pull-out test

The samples were crimped successfully at six different discharge energy 2.0 kJ, 2.2 kJ, 2.3 kJ, 2.5 kJ, 2.6 kJ and 2.9 kJ with three turn solenoid coil. To evaluate the joint strength in tension, the pull-out test of the aluminum tube crimped on the DP steel rod was subjected to a pulling load or tensile load. A total 12 samples, two samples at each discharge energies were tested. Finally, the joint strength was evaluated by performing the tests using the universal testing machine (UTM) at a speed of 0.5 mm/min.

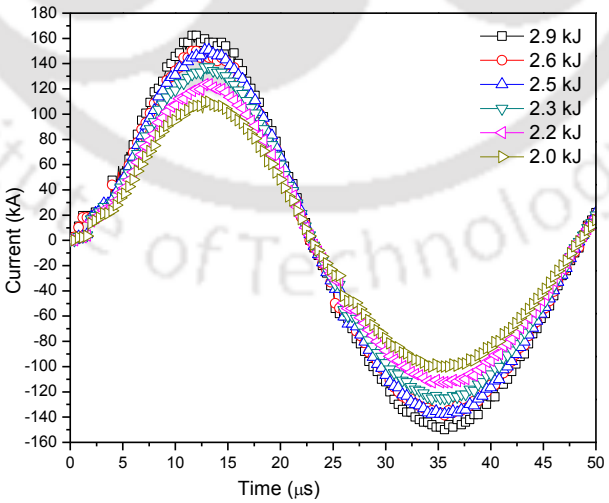

Fig. 3.6 Enlarged view of the first peak of the measured discharge current

The schematic diagram of the pull-out test performed on the UTM is shown in Fig. 3.7. In this test, crimped length was 15 mm and gripping length was 18 mm in the UTM gripper.

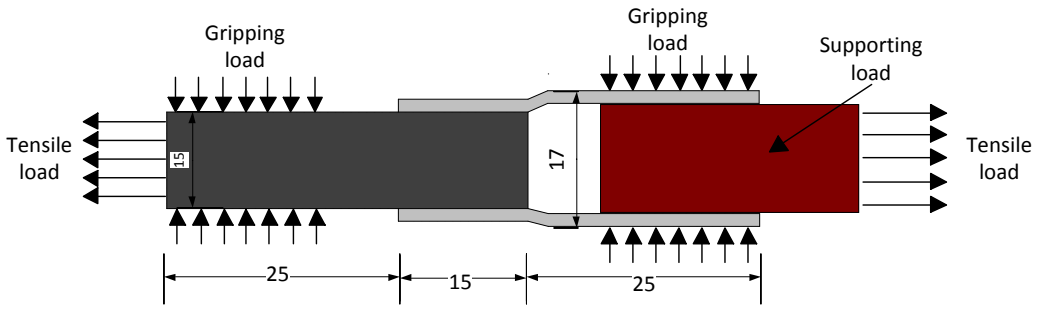

Fig. 3.7 Pull-out test arrangement made

3.3 Results and Discussions

The numerical simulations, as well as the experiments, were performed to obtain the successful crimping of the Al tube on the DP steel. The input parameters which greatly affect the process was the radial gap and the discharge energy. The various post process results obtained from the process were discussed in the preceding sections.

3.3.1 Simulation results

EMC is a complex transient high-velocity impact joining process. It involves the coupling effects of an electromagnetic field, thermal field, and mechanical field. In this work, the electromagnetism module of LS-DYNA was used for coupling the electromagnetic, structural and mechanical process. In this module, source electrical current can be introduced into the ends of the helical coil to solve the problem related to the electromagnetic field, structural field, and thermal field. Three-dimensional meshed numerical model for EMC is shown in Fig. 3.8. Ten simulations were run from 1.0 kJ to 2.9 kJ and out of which six simulations were found suitable for the study. Four simulations run below 2 kJ were not considered because the deformation obtained in the flyer tube was not found to be sufficient.

3.3.1.1 Current and magnetic pressure

The discharge current and the magnetic pressure were also analyzed in the study. The maximum value of the discharge current obtained from the simulation and that from the experiment have variation but in an acceptable range. The discharge current obtained from the simulations is shown in Fig. 3.9. The variation in the maximum value of discharge currents in simulations from the experimental values was found to be 2%, 3% and 7% at 2.5 kJ, 2.6 kJ and 2.9 kJ of discharge energy.

The maximum current produced by a capacitor bank is directly proportional to the charging voltage (V_o) and the square root of the capacitance (C), and also inversely related to the square root of the inductance (L) [2]. Mathematically, the peak current produced can be expressed by equation (3.5) and the current density J is given by the equation (3.6).

$$I_{max} = V_o \sqrt{\frac{C}{L}} \tag{3.5}$$

$$J = n\frac{I}{A} \tag{3.6}$$

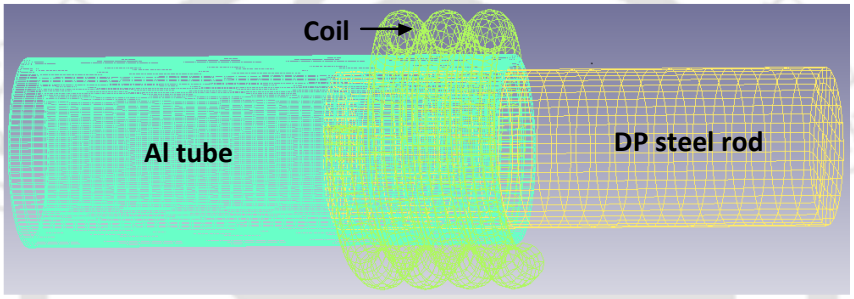

Fig. 3.8 Three dimensional meshed model used for the coupled field analysis

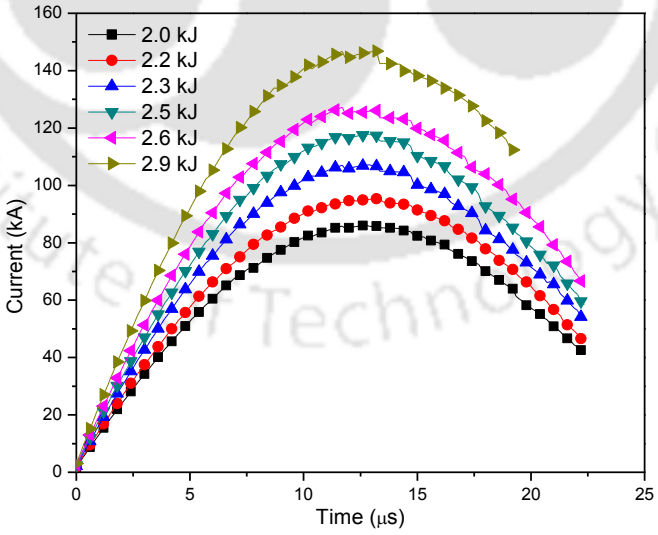

Fig. 3.9 Simulated currents under different discharge energies

where A represents the cross-sectional area of the wire of the actuator and n is the number of turns of the actuator. From the simulation, the contour plot of the current density

generated on the flyer tube at six different time steps at 2.9 kJ of discharge energy is shown in Fig. 3.10. In Fig. 3.10 the units of the current density is mA/mm^2. The maximum magnitude of the current density was observed at about 14 μs and then it was decreasing with the increase in the time.

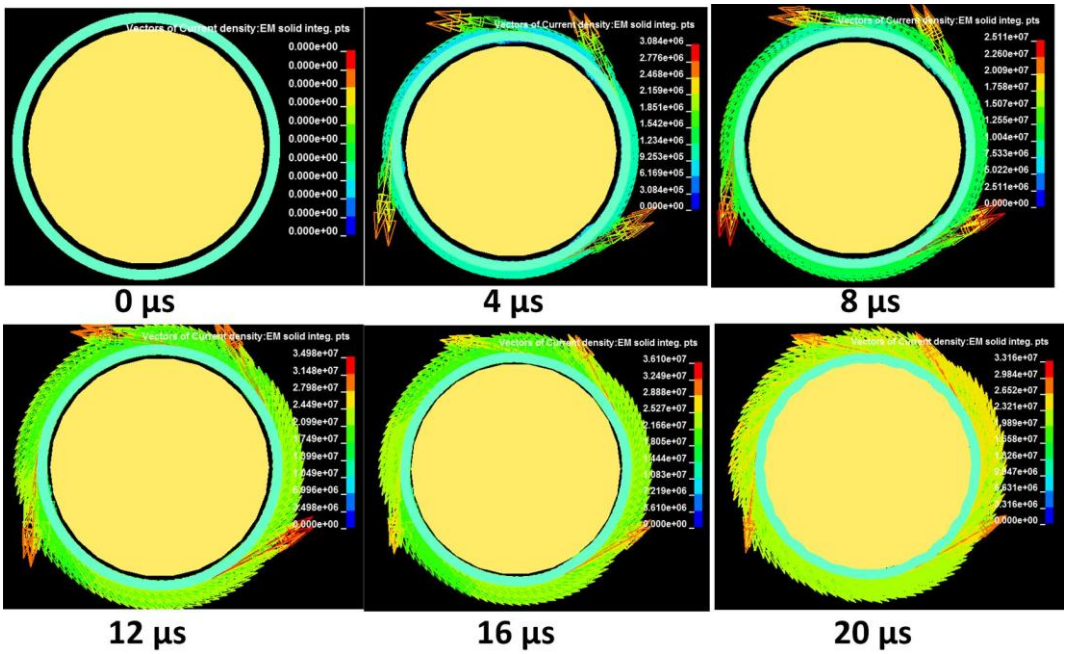

Fig. 3.10 Contour plot of the current density generated on the flyer tube at different time steps

The magnetic pressure variation with the time in the simulation at six different discharge energy is shown in Fig. 3.11. It was found that with the increase in the amount of the discharge energy the magnitude of the magnetic pressure also increases. The increase in the magnetic pressure causes due to the increase in the impact velocity of the flyer tube. It was also observed that first with the increase in time the magnitude of the pressure increases, attains a maximum amplitude and then decreases with the time. The amplitude of the magnetic pressure was maximum corresponding to the maximum amount of applied load i.e., maximum discharge current.

3.3.1.2 Deformation and impact velocity

Deformation of the flyer Al tube was simulated at different energy. Changes in the diameter of the flyer tube at six different time steps are shown in Fig. 3.12. The outer diameter of the flyer tube crimped on the base rod at six different discharge energies was measured in the simulations as well as in the experiment. The outer diameter of the crimped samples both in

the experiment and in the simulations was compared and it is shown in Fig. 3.13. The diameter of the rod and tube was also plotted for taking the reference for comparison.

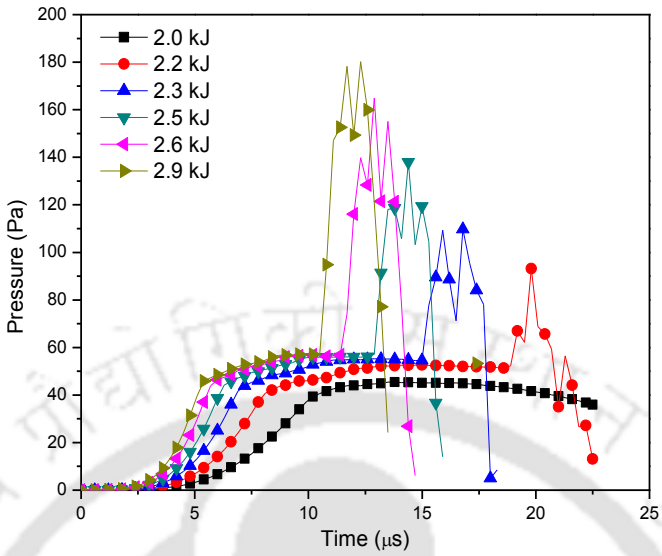

Fig. 3.11 Simulated magnetic pressures under different discharge energies

The measured outer diameter in the experiment is shown in Fig. 3.14 and in the simulation is shown in Fig. 3.15. There was a variation in the measured outer diameter of the crimped samples from the experiment and in the simulation. A maximum of 6.6 % variation was observed in the simulation data with respect to the experiment value. The percentage variation in the outer diameter at six different values of the discharge energy are tabulated in Table 3.4.

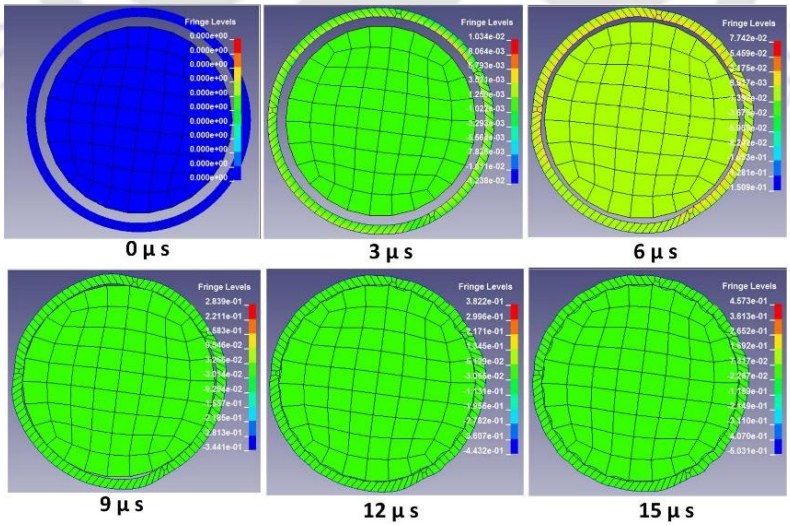

Fig. 3.12 Contours of resultant displacement at six different time steps in the simulations

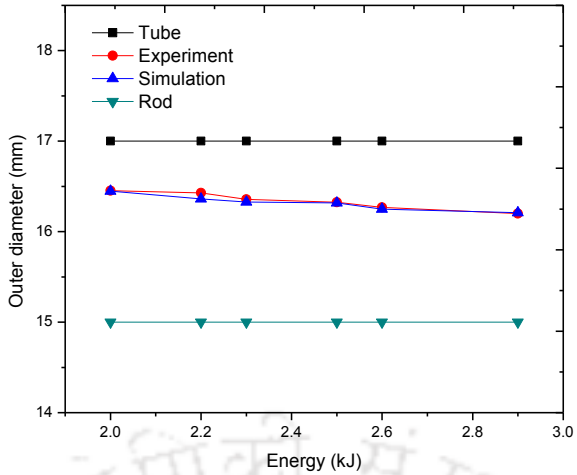

Fig. 3.13 Comparison of outer diameter from the simulation and experiment

With the increase in the discharge energy, the deformation or displacement of the flyer tube also increases. Fig. 3.16 shows the variation of the displacement with respect to time for six different discharge energies. From Fig. 3.16 it can be concluded that with respect to time the deformation of the tube first increases attained the maximum value and then decreases. The maximum deformation obtained was corresponding to the peak value of the discharge current.

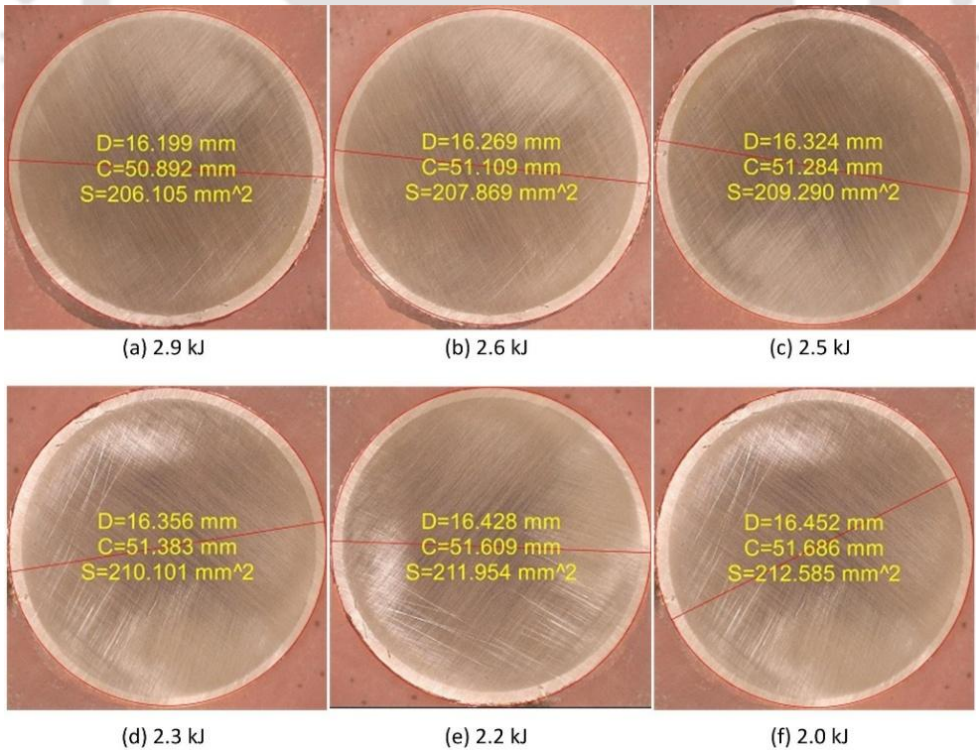

Fig. 3.14 Outer diameter of the crimped sample at six different discharge energy

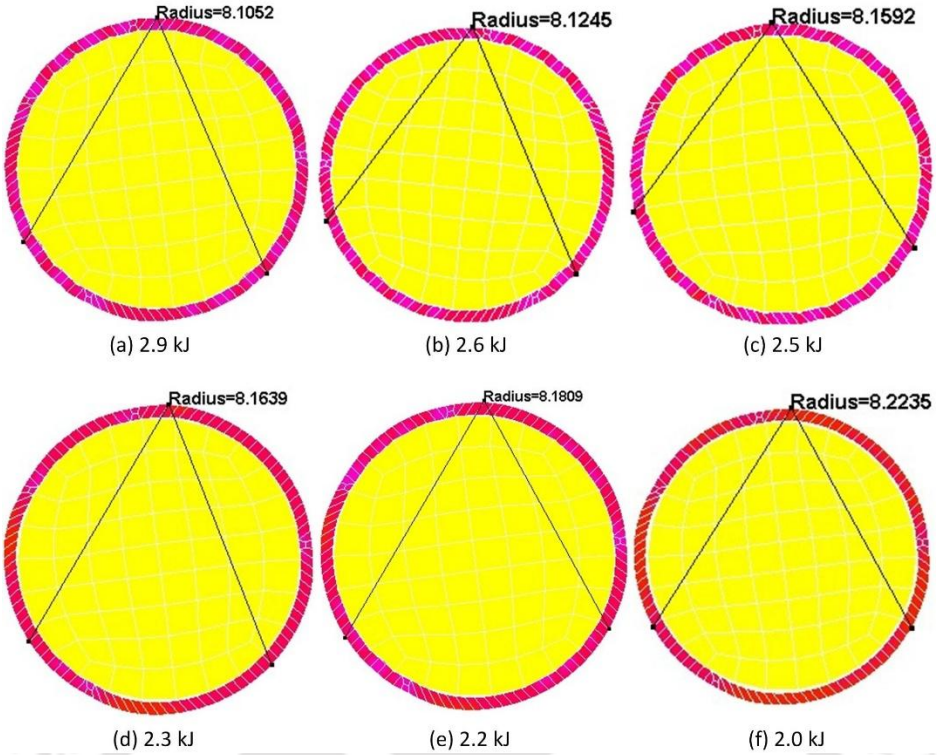

Fig. 3.15 Outer diameter of the crimped sample at six different discharge energies

In EMC, impact velocity is a very important process parameter. In the simulations, the impact velocities under different discharge energies were studied. The average value of simulated impact velocities under six different discharge energies are shown in Fig. 3.17. It can be concluded from Fig. 3.17 that with the increase in the discharge energy the magnitude of the impact velocity also increases. The mechanical strength of the joint was greatly influenced by the amount of the impact velocity, greater the impact velocity higher will be the strength of the joint. It can also be concluded from Fig. 3.17 that for a particular value of the discharge energy the magnitude of the impact velocity first increase with the time, and then decreases. The maximum value of the impact velocity was found corresponding to the peak value of the discharge current.

Table 3.4 Comparison of outer diameter in the experiment and simulation

Energy	**2 kJ**	**2.2 kJ**	**2.3 kJ**	**2.5 kJ**	**2.6 kJ**	**2.9 kJ**
Outer diameter from experiment	16.452	16.428	16.356	16.324	16.269	16.199
Outer diameter from simulation	16.447	16.362	16.328	16.318	16.249	16.210
% variation from experiment	0.5	6.6	2.8	0.6	2	-1.1

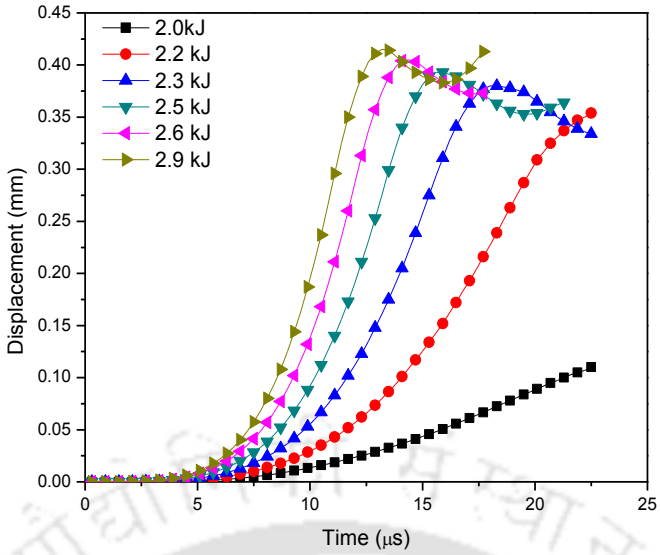

Fig. 3.16 Simulated displacements under different discharge energies

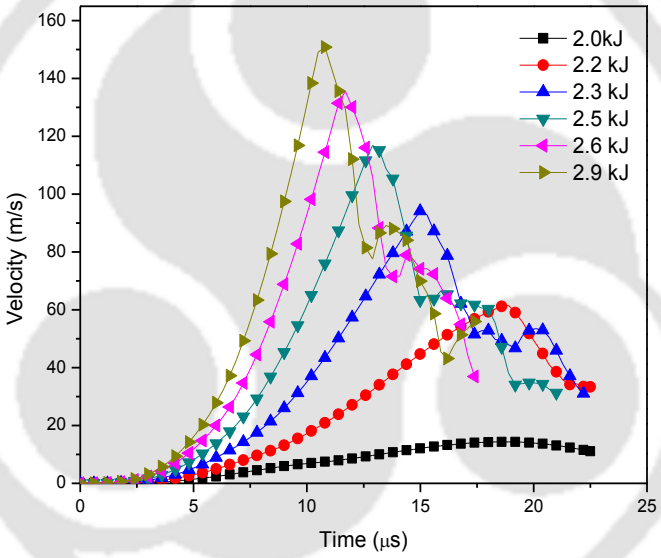

Fig. 3.17 Simulated velocities under different discharge energies

3.3.1.3 Tresca shear stress and magnetic field

The variation of the Tresca maximum shear stress developed in the flyer tube in the simulations was studied. It was found that with the increase in the discharge energy the shear stress value also increases. The variation in the maximum shear stress in the tube with the simulation time at six different discharge energy is shown in Fig. 3.18. The maximum value of the Tresca shear stress developed at six different discharge energies is listed in Table 3.5.

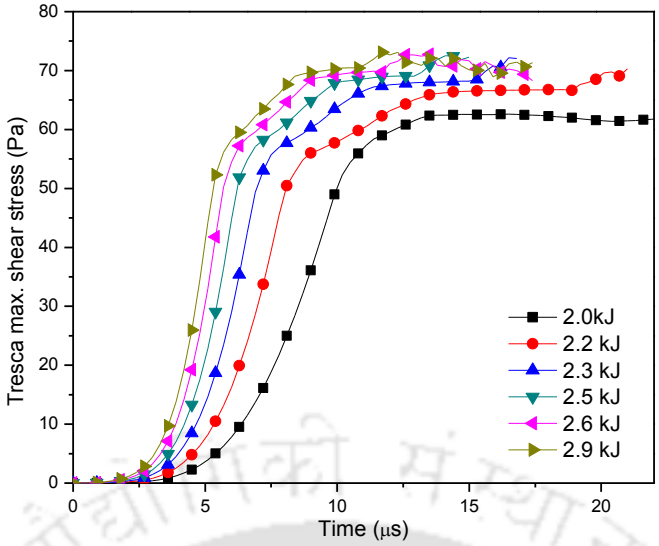

Fig. 3.18 Tresca maximum shear stress in tube at different energy

The magnetic force generated on the flyer tube is a proportion of the magnetic field strength. The distribution of the magnetic field of the flyer tube was studied in the simulation. Fig. 3.19 shows the simulated results of the magnetic field under six different discharge energies. The maximum value of the deformation, impact velocity, discharge current, magnetic pressure, magnetic field strength and plastic strain at six different discharge energy are listed in Table 3.5.

Table 3.5 Simulations results at different process parameters

Energy	**2 kJ**	**2.2 kJ**	**2.3 kJ**	**2.5 kJ**	**2.6 kJ**	**2.9 kJ**
Max. Current (kA)	85.82	95.31	106.7	117.898	126.12	146.8
Max. Disp. (mm)	0.112	0.357	0.38	0.393	0.405	0.415
Max. Plastic Strain	0.009	0.053	0.099	0.140	0.173	0.220
Max. Pressure (MPa)	45.47	93.22	109.77	137.92	164.98	180.24
Max. Lorentz Force (N)	16.95	34.47	58.71	89.49	125.09	167.68
Max. Magnetic Field (Tesla)	5.06	7	9.18	11.4	13.62	15.86
Max. Velocity (m/s)	14.36	61.55	94.18	116.83	135.6	150.89
Tresca Max. Shear Stress (MPa)	62.6	70	72	72.5	72.8	73.1

3.3.1.4 Plastic strain

Plastic strain in the flyer tube as well as in the rod was also studied in the simulations. In literature, it was found that for getting successful crimping or joining minimum value of plastic strain must be attained [64]. In the simulations, the maximum value of plastic strain obtained was 0.23 for 2.9 kJ discharge energy. The contours of the plastic strain in the flyer and in the

rod are shown in Fig. 3.20 and Fig. 3.21 respectively. Fig. 3.22 shows the average variation in the plastic strain with the time of the flyer tube, in the region where deformation occurred. The maximum value of the plastic strain at six different discharge energy is listed in Table 3.5. In Table 3.5, the process parameters such as the maximum values of the current (kA), displacement (mm), plastic strain, pressure (MPa), Lorentz force (N), magnetic field (Tesla), impact velocity (m/s) and Tresca Max. Shear Stress (MPa) is listed at six different energy. It was found that with the increase in discharge energy the process parameters values also increase.

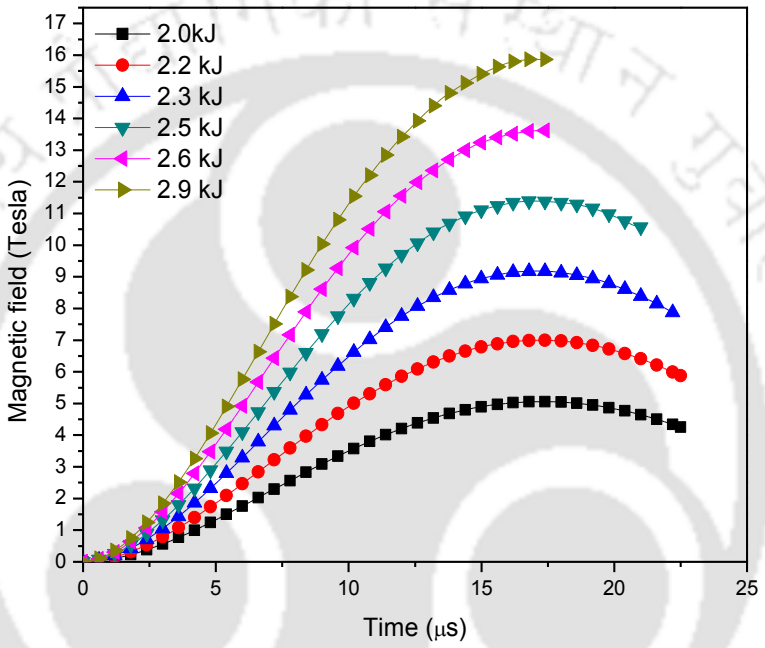

Fig. 3.19 Magnetic field under six different discharge energies

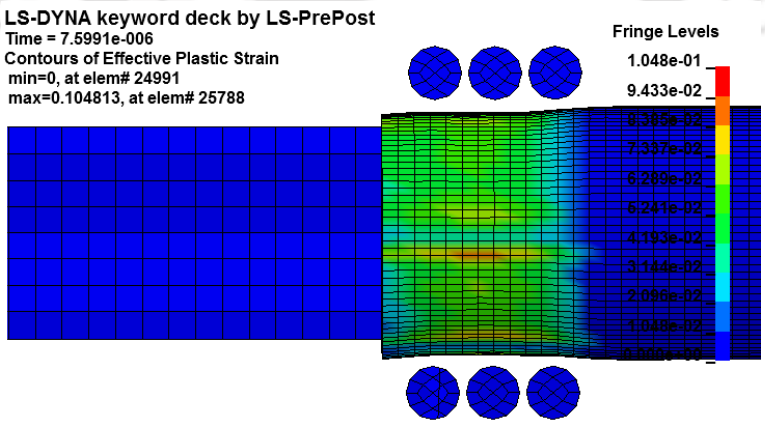

Fig. 3.20 Contours of plastic strain in the tube

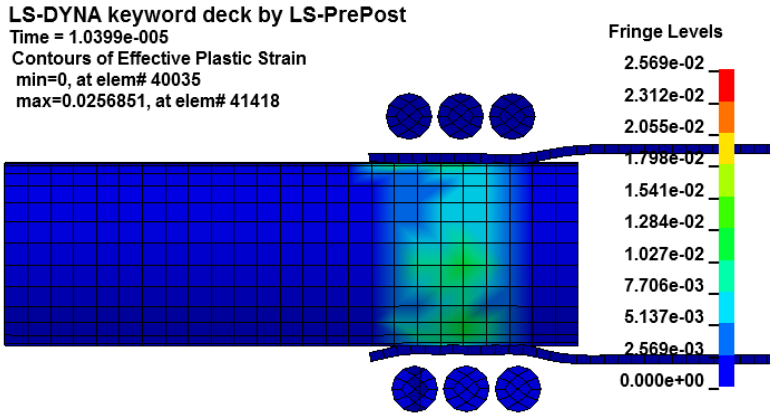

Fig. 3.21 Contours of plastic strain in the rod

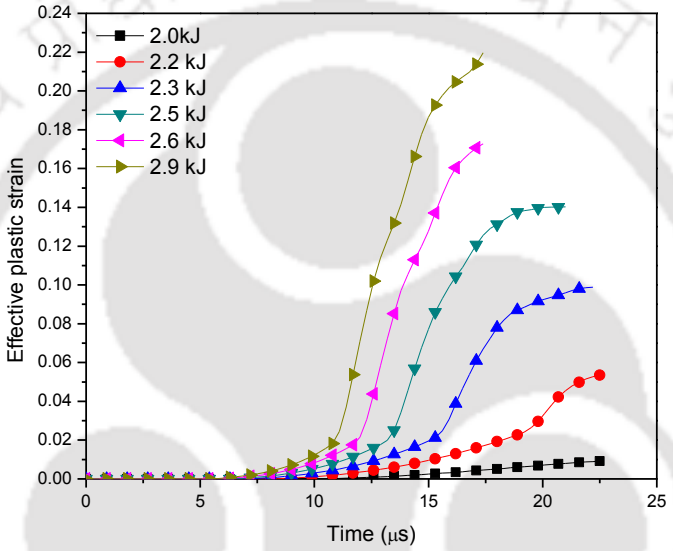

Fig. 3.22 Simulated plastic strains under six different discharge energies

3.3.2 Experimental results

Based on the parameters in the simulations, experiments were performed, and Al tube was successfully crimped on DP steel rod. Fig. 3.23 shows the samples being crimped successfully. The optical microscope (OM) images at the interface of the sample crimped at 2.9 kJ of discharge energy were analysed. In the OM image, a negligible gap was found for the sample being crimped at 2.9 kJ discharge energy. With the increase in the discharge energy, it was found that the quality of crimping was improved.

Different types of the pattern were observed at different locations in the OM images of the electromagnetic crimped samples. Some of the specific interface morphology such as small wavy, large wavy and straight pattern is shown in Fig. 3.24 (a), (b) and (c). These types of

morphology at the interface are due to the unevenness available on the DP steel rod. This will results in such types of morphology after high-velocity impact of the flyer tube on the rod.

Fig. 3.23 Al-tube crimped over DP steel rod

The strength of the crimped joint was varied with the types of profile or surface roughness available on the surface of the base rod. The effect of the mandrel's surface on the mechanical properties of joints was studied by Hammers et al. and found that surface roughness increases the strength of the joint [47].

3.3.3 Hardness test

Hardness tests using Vickers' micro-hardness tester with loads 300 gf and 500 gf were performed. Hardness was measured at four different locations on the sample crimped at 8 kV or 2.9 kJ discharge energy. Fig. 3.25 (a) shows an average hardness traverse across an Al/DP steel clad interface. The increase in hardness near the interface base materials is due to the high-velocity impact.

3.3.4 Pull-out test

The variation in the pull-out load and corresponding extension obtained in the joined sample at six different discharge energies is shown in Fig. 3.25 (b). Pull-out test results revealed that all the samples joined up to 2.9 kJ of discharge energy fail with separation failure mode. In the separation failure mode, the two samples joined together were separated from each other from the joint. The maximum pull-out load required was increased with the increase in discharge energy used to join the sample. With the increase in the discharge energy, the strength of the joint was increased, due to the increase in the impact velocity of the flyer tube. The normalized

maximum pull-out load with the yield strength of the tube variation with the discharge energy is shown in Fig. 3.26.

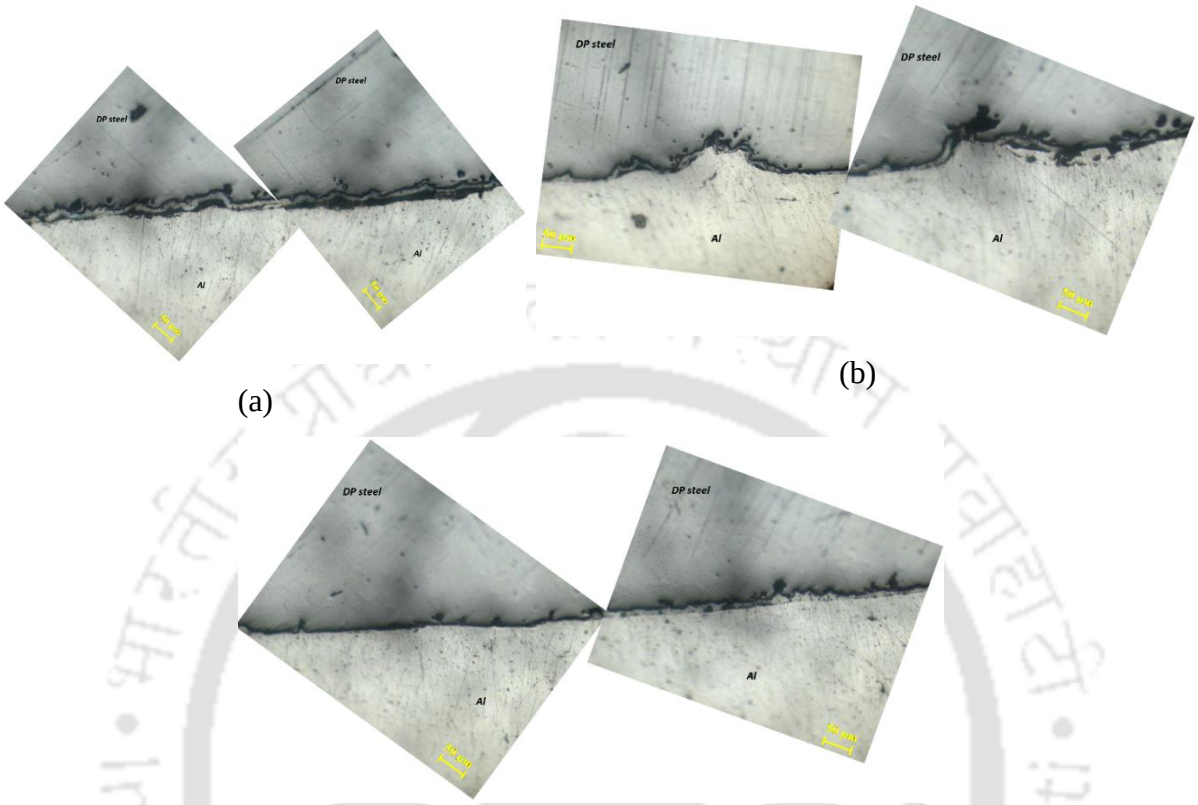

Fig. 3.24 Small wavy interface morphology along crimping interface of the crimped sample (a) small wavy, (b) large wavy, and (c) straight pattern

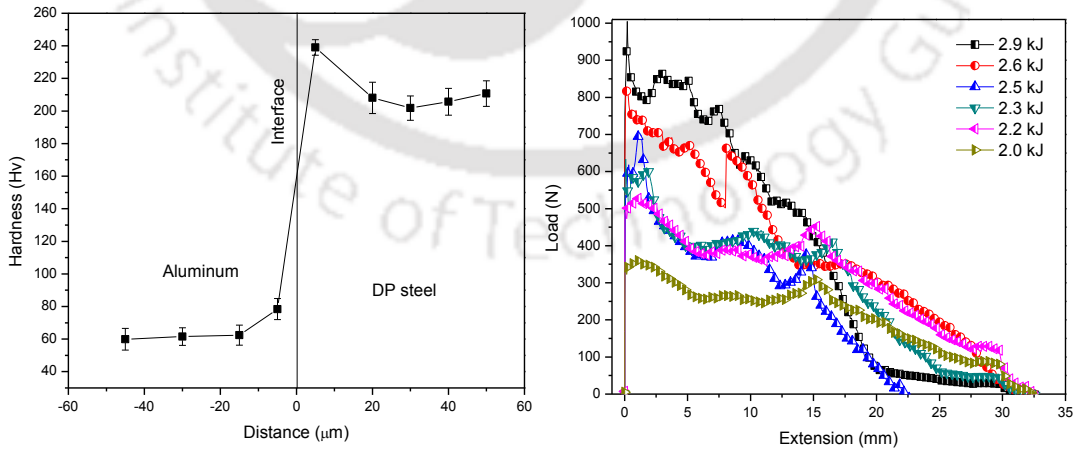

Fig. 3.25 (a) Hardness traverse across Al and DP steel crimped interface, and (b) pull-out load vs. extension plot at six different discharge energy

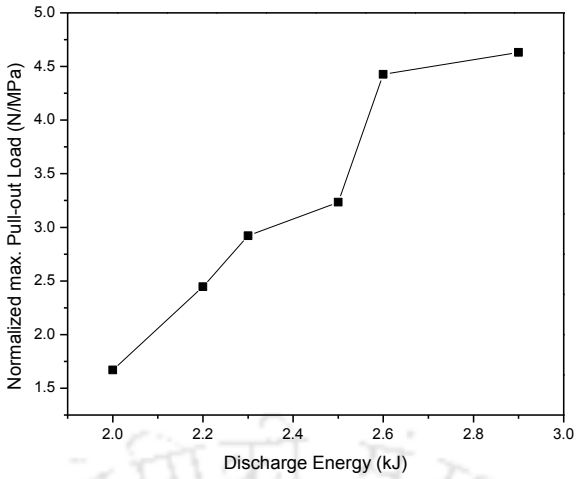

Fig. 3.26 Normalized max. pull-out load vs. discharge energy

3.4 Summary

EMC is a joining by high-velocity forming technique. In this chapter, first of all, EMC was simulated for ten different discharge energies out of which six simulations were chosen for the experiments. Experiments were performed based on the chosen simulations parameters and Al-tube was successfully crimped on the dual phase steel rod. Simulations results were validated with the experimental results with measured discharge current and the outer diameter of the flyer tube in the crimped sample. Variation was found in the maximum value of discharge currents in simulations from the experimental values and it were 2%, 3% and 7% at 2.5 kJ, 2.6 kJ and 2.9 kJ of discharge energy. The outer diameter of the successfully crimped samples was measured and compared with the outer diameter of the model in the simulations and found a maximum of 6.6 % variation in the simulation value from the experimental value. From the experimental work and simulation results, it can be concluded that process parameters such as stand-off distance, impact velocity, and discharge voltage or discharge energy must have a threshold value of 0.4 mm, 116.83 m/s and 2.5 kJ, respectively, for achieving successful crimping. Optical microscopy analysis revealed that there was a negligible gap in the sample crimped at 2.9 kJ of discharge energy. Hardness test showed that hardness was increased near the interface base materials due to the high-velocity impact. The strength of the joints produced by crimping Al tube on the dual phase steel rods has increased with the increase in discharge energy and a maximum load obtained in the test was 1015 N for sample crimped at 2.9 kJ.

.----------*----------*----------.

4 Effects of Surface Profiles on the Copper-Steel Joint Formation

OVERVIEW

In this study, experiments were carried out for fabrication of copper-steel crimped or composite rods. For production of composite rod three types of profiles threaded, knurled, and plain profile were created on the steel rod and then a copper tube was crimped over the rod. The mechanical properties of the joint was evaluated by pull-out test, compression-shear test and hardness test. The influence of surface profiles on the joint strength, surface roughness and microstructure of the joint were analyzed and compared. Compression-shear tests as well as pull-out tests were carried out to compare the strength of the crimped joint. The result of the pull-out tests as well as compression-shear tests revealed that threaded surface profile on the steel rod gives better strength in comparison to the other two profiles. Along the circumference of the Copper-Steel composite rod the microstructure images of the joints were taken and analyzed, it was found that there was no gap along the circumference of the sample crimped at 5.3 kJ of discharge energy with plain profile. For surface roughness, the R_a values of the crimped samples at 5.3 kJ were analyzed and it was found that average R_a value of the sample crimped on the threaded base was highest (0.80 μm) among threaded, knurled, and plain base samples. The effect of the surface profiles on the base rod on crimping quality was studied. The microstructure of the joint interface was studied and analyzed.

4.1 Methodology

The crimping experiments were performed on cylindrical assembly by using a electromagnetic processing system. The electromagnetic processing system (EMPS) transforms the low-voltage power supply into a high voltage power supply having a range of 0-15 kV. The EMPS used have total discharge energy of 10 kJ with a capacitance of 90 μF. The discharge current passes throughout a multi-turn solenoid coil, which provides a Lorentz force that causes the collision of the flyer tube onto the inner stationary rod.

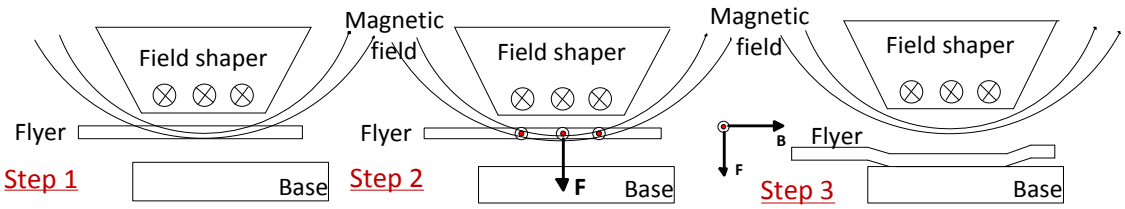

Fig. 4.1 Principle of the EMC process

The inductive coil used in the experiments was composed of a 9 turn solenoid coil and a field shaper which focuses the magnetic field in the work zone of 14 mm length and 11 mm diameter. The discharge pulse current frequency was measured with a Rogowski coil and oscilloscope. The experiments were carried out on samples with Cu flyer tube and steel inner rod. The detail dimensions of the working zone in the experiment used is shown in Fig. 4.3.

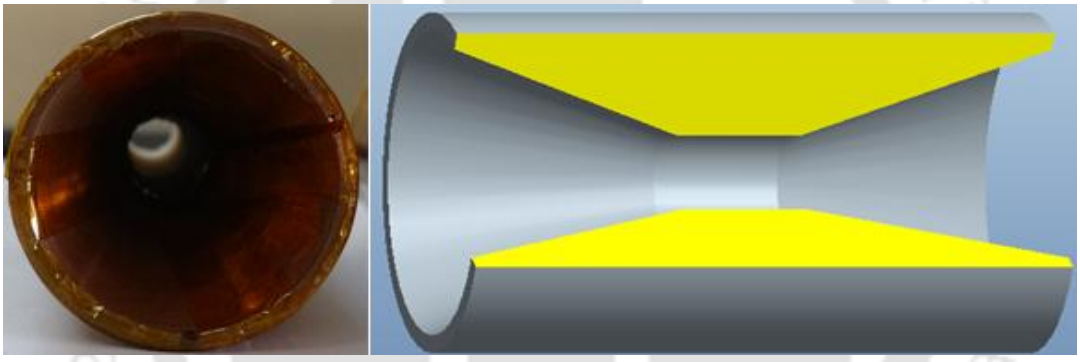

(a) (b)

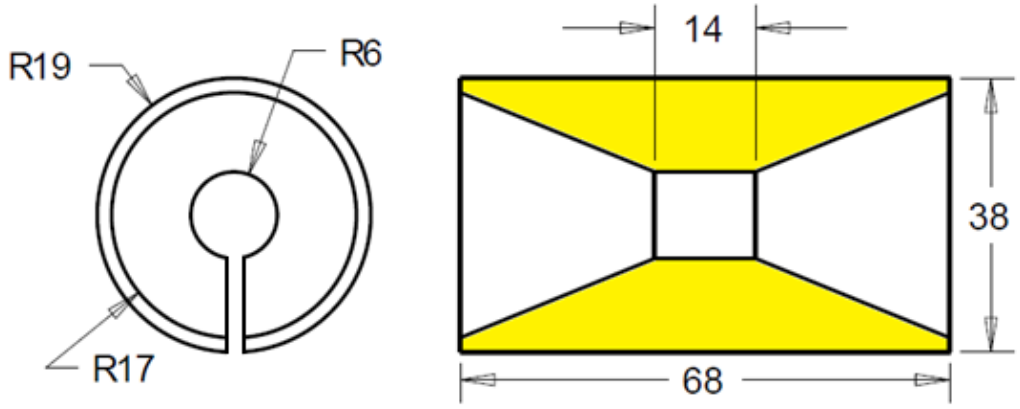

(c)

Fig. 4.2 Field shaper used in EMC (a) an actual image of the field shaper, (b) cross-section of the CAD model, and (c) dimensions of the field shaper

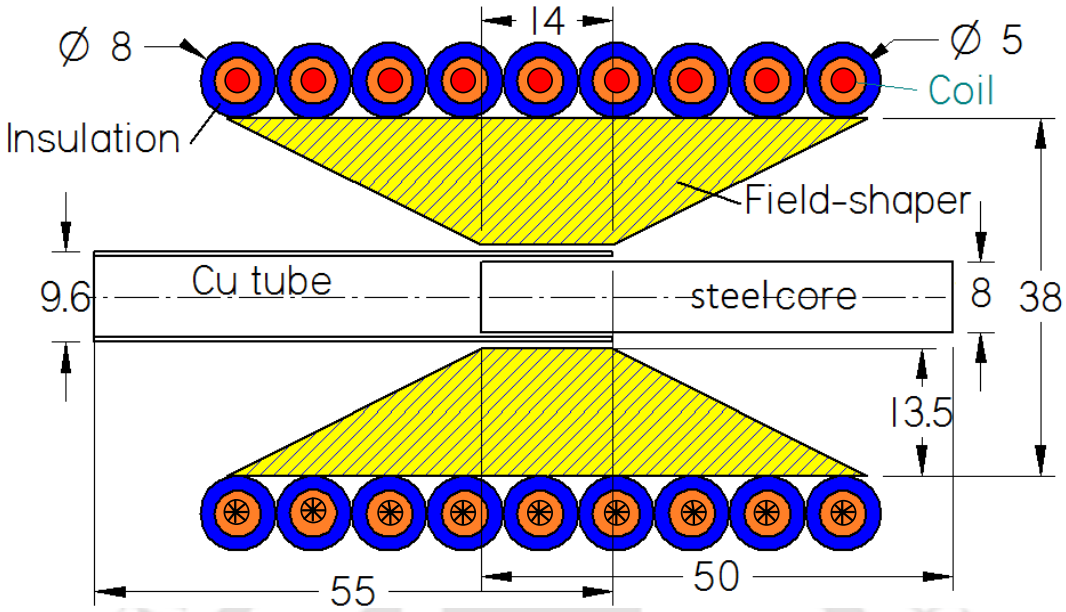

Fig. 4.3 Dimensions of the working zone in the experimental setup

4.1.1 Workpiece materials and their properties

Copper tube having a thickness of 0.5 mm was used as a flyer tube and steel was used as a core material, which was stationary. Dimensions of the tube and rod and their materials are given in Table 4.1 and the mechanical properties of the tube and rod are given in Table 4.2. The chemical composition in weight % of copper tube and steel rod was analyzed using energy dispersive X-ray spectroscopy (EDX) and compared with the standards available. Chemical compositions of Cu tube and steel 1020 rod is given in Table 4.3. The gap of 0.7 mm between the coil and the field shaper was maintained. The gap between the flyer tube and the base rod was 0.3 mm, which is about half of the thickness. In this work, plain surface profile as well as threaded and knurled surface profiles were produced on the steel rod.

Table 4.1 Dimensions of the tube and rod and their materials

Specimen	Outer diameter	Inner diameter	Length	Material
Rod	8.0 mm	-	50	Steel 1020
Tube	9.6 mm	8.6 mm	50	Copper

Table 4.2 Mechanical properties of the tube and rod

Part	Rod	Tube
Density (kg/m^3)	7870	8940
Young's modulus (GPa)	465	89
Poisson's ratio	0.29	0.31
Ultimate tensile strength (MPa)	650	227

Three combinations of the samples were prepared for the experiments, each combination consists of Cu tube and steel rods with three types of profiles. The CAD model as well as actual image of the steel rod having different surface profiles and corresponding dimensions of the profiles are shown in Fig. 4.4. The pitch of the thread (Thread per inch, TPI=25) and knurl (TPI=15) used was 1.0 mm and the type of knurl was general purpose point indented diamond knurls with 30° helix angle.

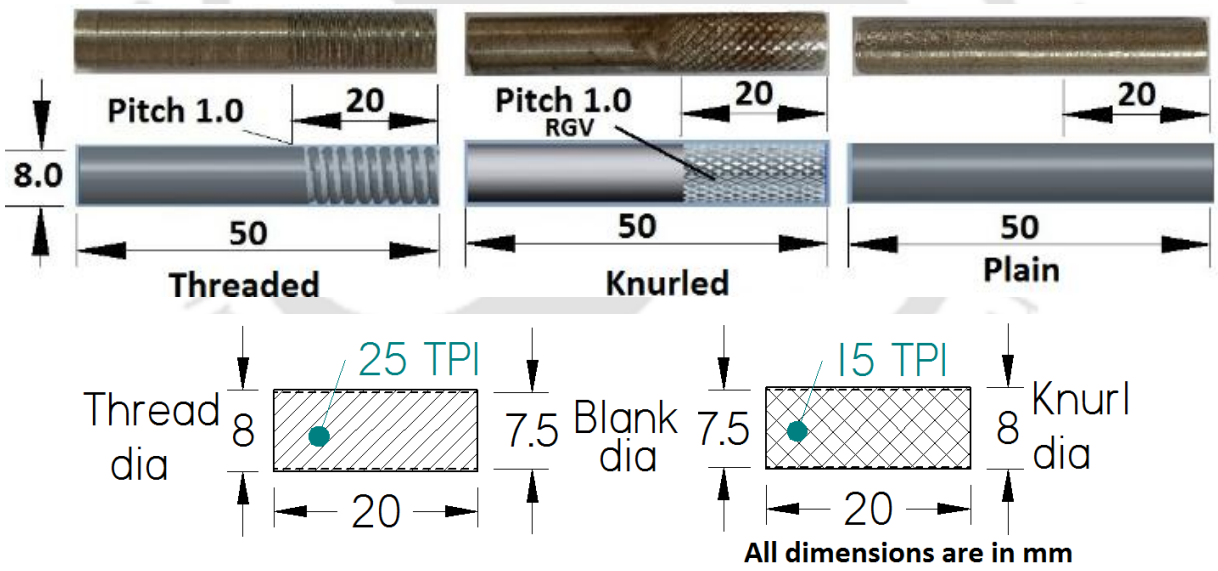

Fig. 4.4 Actual image as well as the CAD model of the three types of profiles threaded, knurled & plain, and dimensions of the thread and knurls

4.1.2 Pull-out test

In pull-out test the crimped interface of the Cu tube crimped on the steel rod was subjected to tensile load or pulling load to evaluate the joint strength. A total of 30 samples, two samples of each combinations namely plain, knurled and threaded steel rod with the Cu tube at five

different values of discharge energies were tested. Finally, to evaluate the strength of the joint, pull-out tests were performed by using Instron UTM at a speed of 0.5 mm/min. Schematic representation of the pull-out test carried out on the UTM is shown in Fig. 4.5. In this study, crimped length was 14 mm, gripping length was about 25 mm.

Table 4.3 Chemical compositions of Cu tube and steel 1020 rod (in weight %).

Material	**Composition (wt. %)**							
	C	**Mn**	**Ni**	**P**	**S**	**Cu**	**Cr**	**Fe**
Steel 1020	0.16-0.25	0.3-0.4	≤0.1	≤0.1	0.1-0.4	0.1-0.2	0.15-0.25	Rest
	Zn	-	Cu	Mn	Fe	P	Sn	
Cu	0.2	-	Rest	0.1	0.2	0.1	0.1	

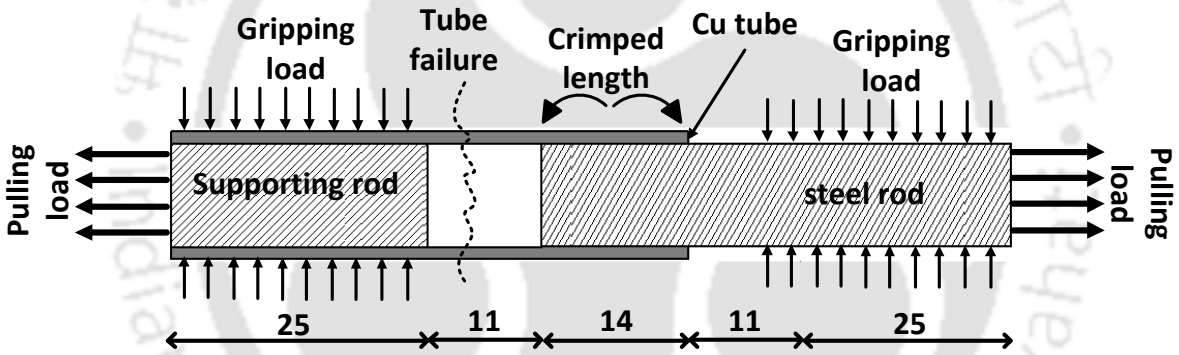

Fig. 4.5 Schematic representation of the pull-out test (all dimensions are in mm)

4.1.3 Compression-shear test

In compression-shear test, the crimped interface of the Cu tube crimped on the steel rod was subjected to compressive load to evaluate the joint strength. The crimped samples were cut continuously by wire electric discharge machine (WEDM), along the transverse direction of the length. The thickness of the crimped samples is 2 mm. A total of 27 samples, three samples of each combinations namely plain, knurled and threaded steel rod with the Cu tube at three different energy were cut for the test. Finally, to evaluate the strength of the joint compression-shear tests were performed by using Instron UTM at a speed of 0.5 mm/min.

Thereby, the joint strength (τ) of the joint, which according to equation (4.1) can be calculated from the maximum compressive load (P_{max}) in the load-extension plot and

crimping area (A). The crimping area (A) can be calculated by multiplication of circumference of the rod (πd) and thickness of the sample (h).

$$\tau = \frac{P_{max}}{A} = \frac{P_{max}}{\pi dh} \tag{4.1}$$

For compression-shear test to perform, an indenter and a holder was manufactured. In the holder, samples were kept and compressive load was gradually applied with the help of an indenter. The schematic of the principle involved in the compression-shear test and the fixture developed for the test is shown in Fig. 4.6 (a) and (b) respectively.

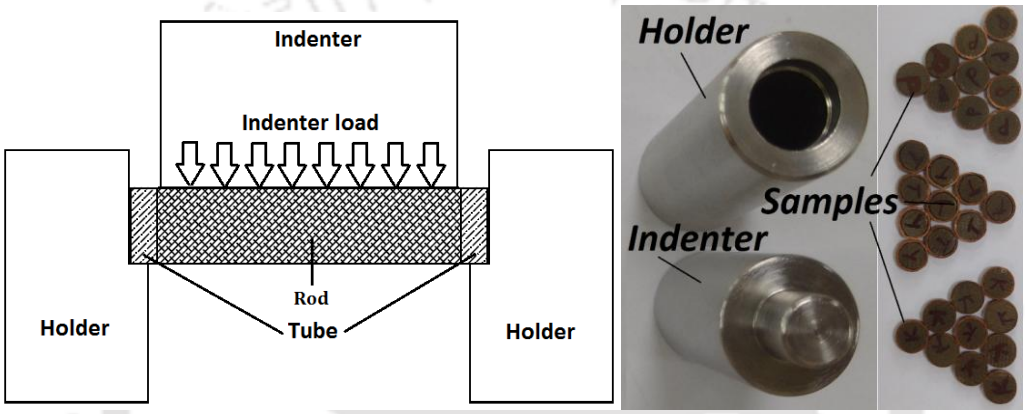

Fig. 4.6 (a) Compression-shear test schematic representation, and (b) sample, indenter and holder for compression shear test

4.2 Results and Discussion

4.2.1 Process characteristics

Entire set-up was fitted and then first of all the discharge current was measured by using a Rogowski coil to analyze the discharging parameters. Fig. 4.7 shows the discharge current curve at different level of discharge energy. Different Process parameters used in the experiments are tabulated in Table 4.

4.2.2 Effect of the discharge energy on the bonding strength

Experimental tests were performed for assessing the effect of discharge energy on joint strength with radial gap of 0.3 mm and feeding length of 14 mm. The discharge energies used were 2.7 kJ, 3.3 kJ, 3.9 kJ, 4.6 kJ and 5.3 kJ. The mechanical properties of the crimped joints are examined by pull-out tests.

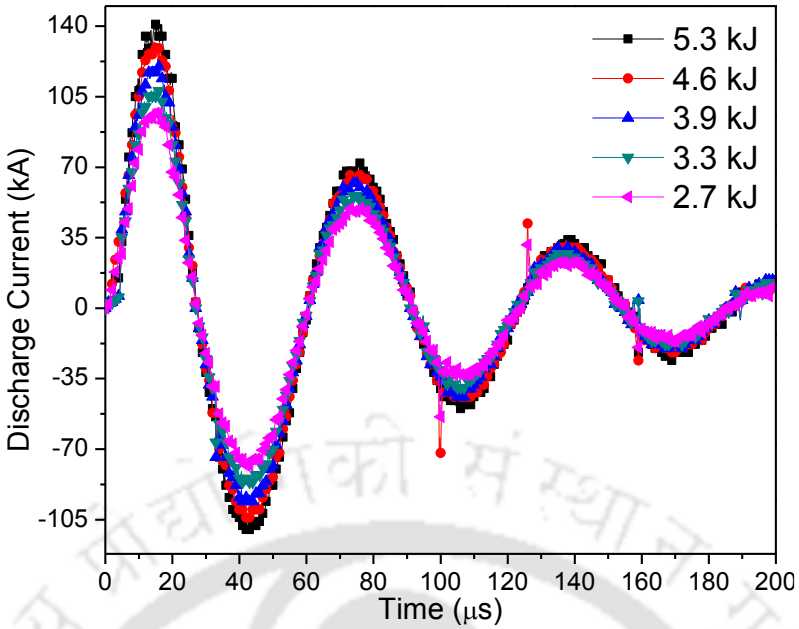

Fig. 4.7 Waveform of the discharge current at different energy level

Table 4.4 Process parameters used in the experiments

S No	Voltage (kV)	Energy (kJ)	Peak current (kA)	Time-period (μs)	Frequency (Hz)
1.	7.8	2.7	99	60.6	16502
2.	8.6	3.3	108	60.4	16556
3.	9.3	3.9	120	60.2	16611
4.	10.1	4.6	132	60.0	16667
5.	10.9	5.3	141	60.0	16667

In the pull-out test, it was found that crimped joints failed with two failure modes separation and crack failure mode. In separation failure mode, the two parts crimped together were separated but in crack failure mode weaker part was failed in the test. Crimped samples prepared at 2.7 kJ and 3.3 kJ, with three types of surface profiles failed with separation failure mode. Whereas crimped samples prepared at 3.9 kJ, 4.6 kJ or more, with three types of surface profiles failed with crack failure mode.

The crimped samples failed in the pull-out tests with two failure modes are shown in Fig. 4.8 (a) and (b). Threshold value of discharge energy was found to be 3.9 kJ for effective

joint strength i.e. strength of the joint was higher than that of the strength of weaker parent materials. The variation in the maximum pull-out load with the discharge energy for three types of the surface profiles is shown in Fig. 4.9(a). The variation in the normalized maximum pull-out load, normalized with the yield strength of the tube with the discharge energy for three types of the surface profiles is shown in Fig. 4.9(b).

Fig. 4.8 Samples after pull-out test (a) failure in the joint at lower energy (2.7 kJ and 3.3 kJ), (b) failure in the tube at higher energy (3.9 kJ and 4.6 kJ)

Crimped samples prepared at three different discharge energies 3.9 kJ, 4.6 kJ and 5.3 kJ were tested for compression-shear test. The samples which got separated after the test are shown in Fig. 4.10. The joint strength of the crimped samples prepared at three different discharge energies were tested by compression-shear test. The average variation in the joint strength at three level of discharge energies with three types of profile is shown in Fig. 4.11. From Fig. 4.11 (a), it can be concluded that increase in energy leads to increase in the strength of the joint. The failure of the joint in case of threaded profile, follows a non-uniform (i.e. increasing and decreasing) pattern after maximum load because of the crest and the root of the thread created on the steel rod. The joint failure for knurled profile as well as plain profile follows uniform decreasing pattern after maximum load.

4.2.3 Effect of the base profile on the bonding strength

The crimped samples prepared for five different discharge energies were tested using pull-out test. In the pull-out test, it was found that the samples prepared at 2.7 kJ and 3.3 kJ failed by separation failure while for discharge energy 3.9 kJ or more the samples failed by crack failure mode. The normalized load-extension plot for three type of profiles plain, knurled and threaded

profile at three different discharge energies 2.7 kJ, 3.3 kJ, and 3.9 kJ is shown in Fig. 4.12. The samples prepared at 4.6 kJ and 5.3 kJ were also failed by crack failure mode.

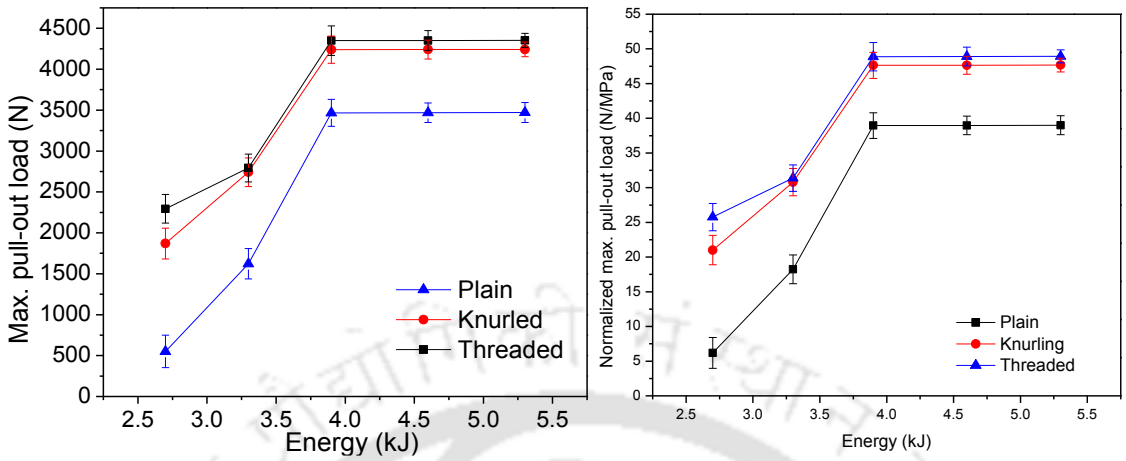

(a) (b)

Fig. 4.9 Variation in the (a) maximum pull-out load, and (b) normalized maximum pull-out load with the discharge energy for three types of the surface profiles

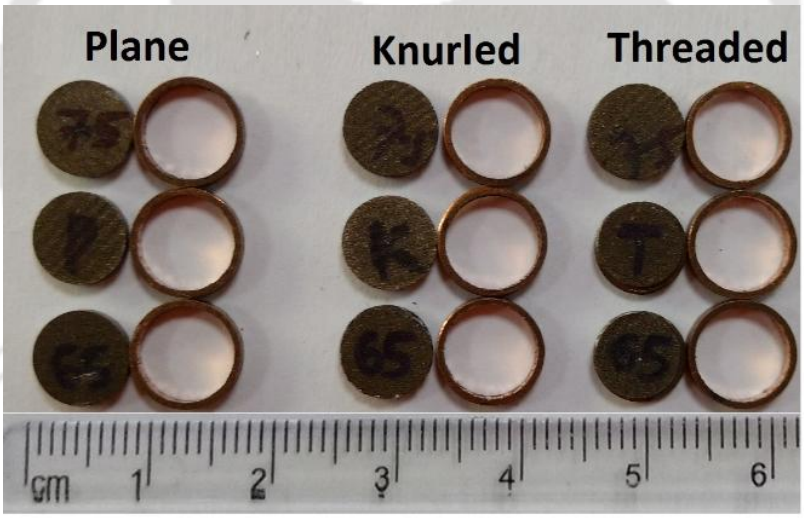

Fig. 4.10 Samples obtained after compression-shear test with three different profiles and three different energy level

In Fig. 4.12 (a), the failure of the joint in pull-out test for threaded profile, follows a zig-zag i.e. increasing and decreasing pattern after maximum load applied because sticking of the copper tube in the crest and the root of the thread created on the steel rod. The joint failure in pull-out test for knurled profile also follows the zig-zag pattern due to sticking of the copper tube inside the knurled profile as shown in Fig. 4.12 (b), whereas it has smooth pattern for plain profile as shown in Fig. 4.12 (c).

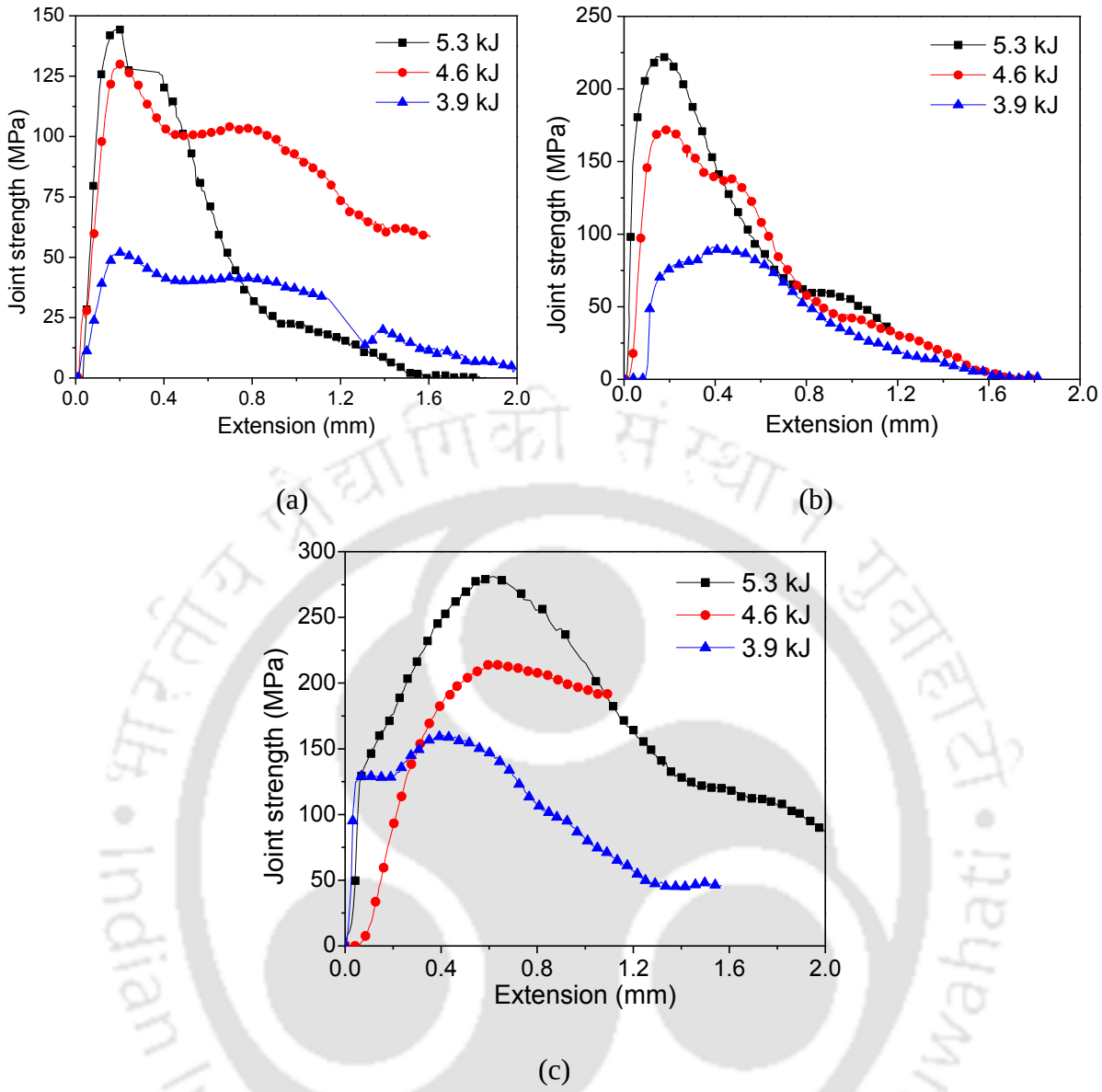

Fig. 4.11 Average strength-extension plot for (a) plain, (b) knurled, and (c) threaded profile at three level of energies

The cut samples were compression-shear tested by keeping it into the holder and applying the load through the indenter. The variation in the maximum compressive load applied with the discharge energy for three types of the surface profiles is shown in Fig. 4.12 (d). Joint formed with the threaded profile produce better strength in comparison to the plain as well as knurled profile because of the flow of the crest of the thread inside the tube. The crest of the thread get inserted inside the tube resists the applied load while failure. The joint formed with knurled profile give better strength than plain due the flow of profile inside the copper tube, which was not possible for the plain profile.

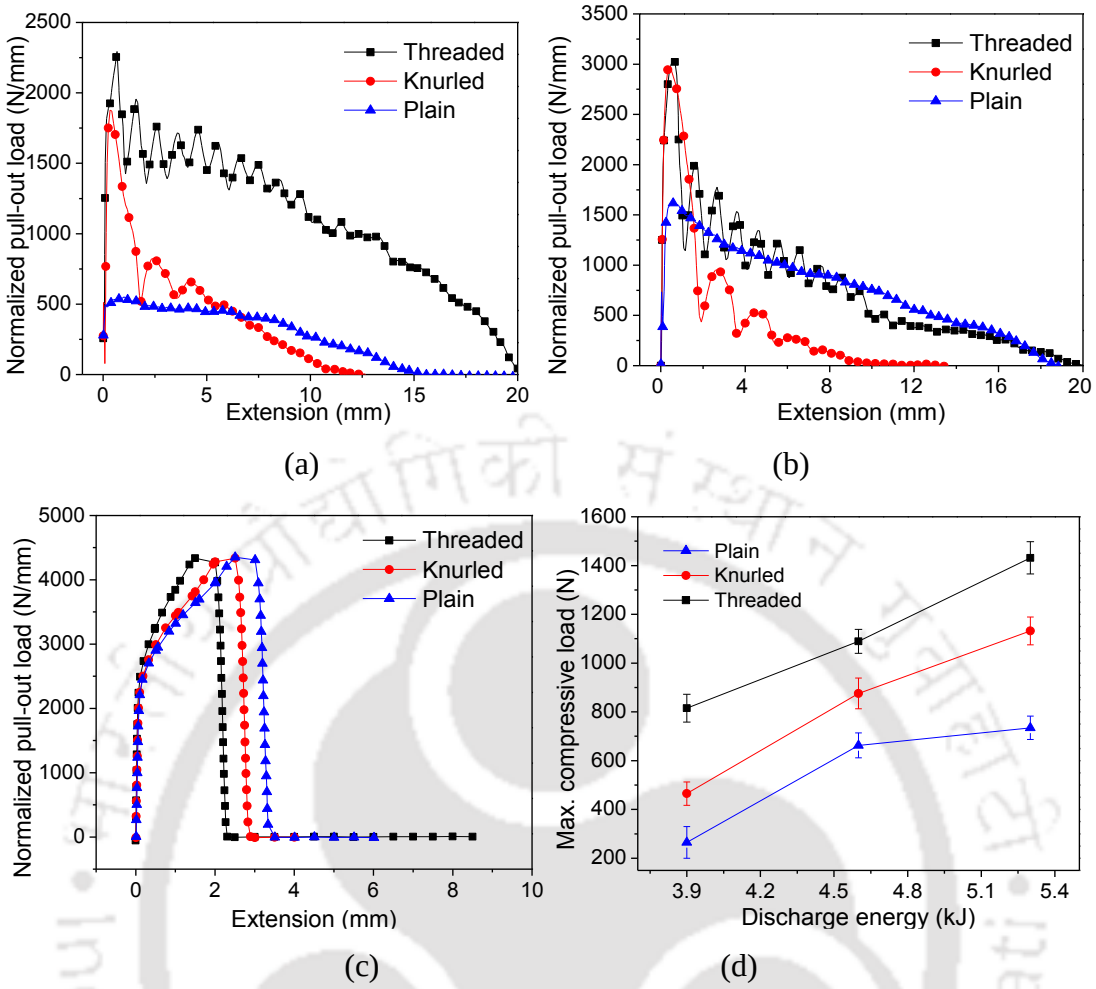

Fig. 4.12 Average load-extension plot for plain, knurled and threaded profile at (a) 2.7 kJ, (b) 3.3 kJ, (c) 3.9 kJ, and (d) variation in the maximum compressive load with the energy for three types of profiles

4.2.4 Characterization of the crimped joint

The crimped samples at 5.3 kJ of discharge energy were cut along the transverse direction of the central axis with a wire electric discharge machine under distilled water cooling, to avoid possible microstructural change. Samples were ground to the finishing step with 300, 600, 1200, 1500, and 2000-mesh metallurgical sand chapter under water cooling, followed by cloth polishing to 0.05 μm Al_2O_3 powder abrasives water suspension in the finishing pass. For each combinations, the sample prepared at 5.3 kJ energy, the crimped zone was photographed with a digital microscope (for low magnification image) with image software and with an optical microscope (for high magnification image).

The outer diameter of the successfully crimped samples with three types of profile on the steel rod was measured at three discharge energy 3.9 kJ, 4.6 kJ and 5.4 kJ. The cross-sectional view

and their dimensions of the Cu-steel composite rods after crimping at 5.3 kJ discharge energy is shown in Fig. 4.13. The measured outer diameter of the composite rods comparison at three different discharge energies was plotted and it is shown in Fig. 4.14.

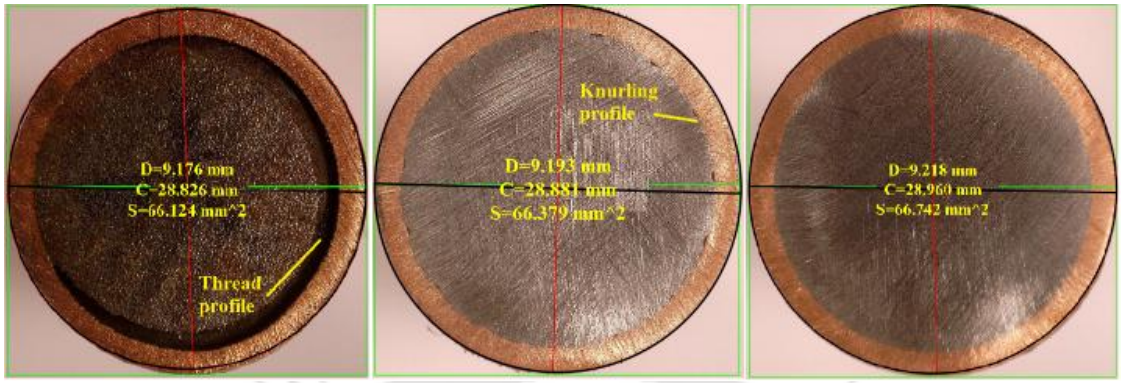

Fig. 4.13 Digital microscope images of the cross-section of the composite rods with measured outer diameter with (a) threaded, (b) knurled, and (c) plain profile at 5.3 kJ

The microscopic images of the successfully crimped samples with three types of surface profiles on the steel rod are shown in Fig. 4.15. It can be observed from the microscopic images that there was negligible gap at the interface of the copper tube crimped on the plain profile steel rod at 5.3 kJ of discharge energy. Neither metallurgical bond nor interlayers was observed in the microscopic images of the electromagnetic crimped composite rods.

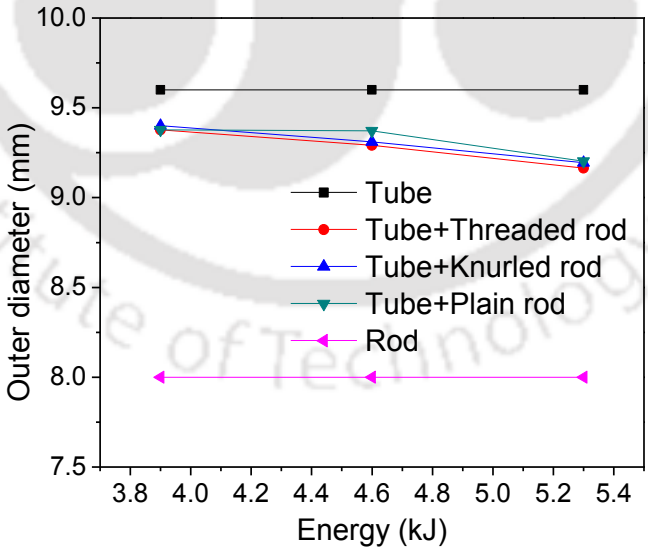

Fig. 4.14 Outer diameter of the composite rods comparison measured at three different energy with Cu tube and steel rod

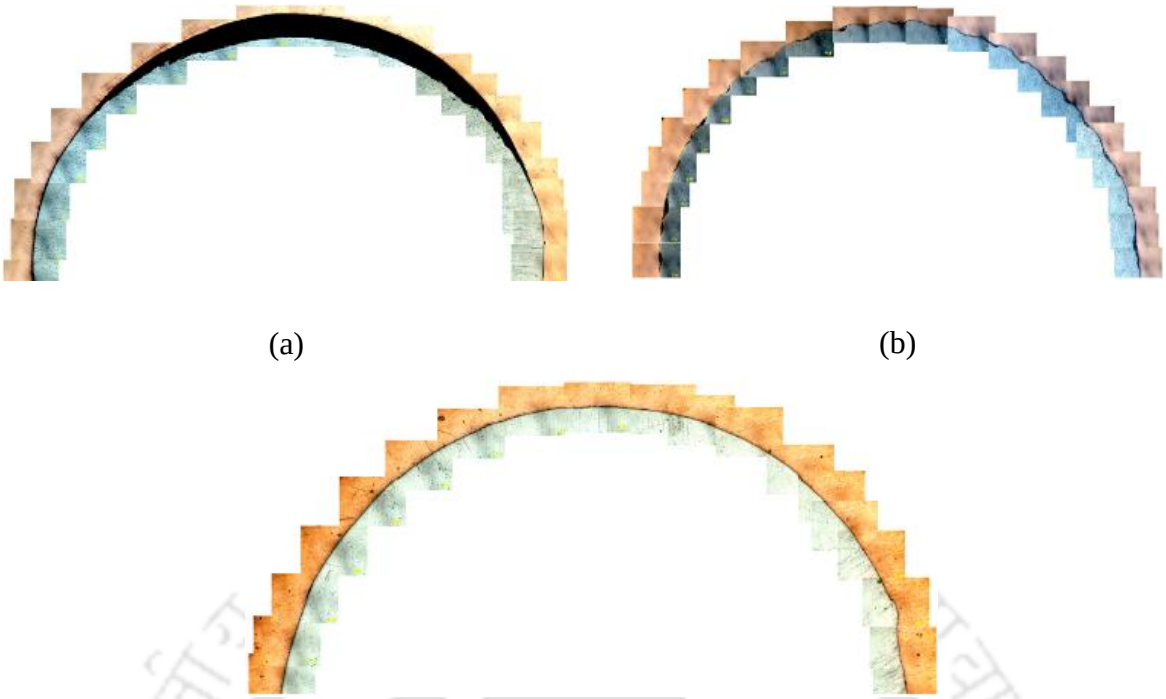

(a) (b)

(c)

Fig. 4.15 Microscopic images of the electromagnetic crimped samples with (a) threaded, (b) knurled, and (c) plain profile at 5.3 kJ

4.2.5 Surface roughness analysis

Surface roughness of the electromagnetic crimped samples with three types of the surface profiles on the steel rod was analyzed by using high precision non-contact computerized surface profilometer. The maximum area that can be captured with the help of non-contact 3D profiler was 0.825 mm × 0.825 mm. The focal length of the profiler was 4.7 mm. Surface roughness of the samples crimped at 5.3 kJ of discharge energy with three types of surface profiles of the steel rod was analyzed. The R_a values were measured at three locations, and the average R_a values were calculated. The average surface roughness values were normalized with the sheet thickness (0.5 mm). The normalized surface roughness values with three types of surface profiles on the steel rod was tabulated in Table 4.5.

From this study, it can be concluded that the surface roughness value of the crimped sample with threaded profile on the steel rod was highest among three profiles threaded, knurled and plain on the steel rod. 3D fringe pattern of the surface roughness with varying R_a values for all three types of the surface profiles on the steel rod at 5.3 kJ of the discharge energy is shown in Fig. 4.16.

Table 4.5 Average normalized surface roughness at 5.3 kJ

Profile	**Plain**	**Knurled**	**Threaded**
Normalized R_a	0.82×10^{-3}	1.2×10^{-3}	1.60×10^{-3}

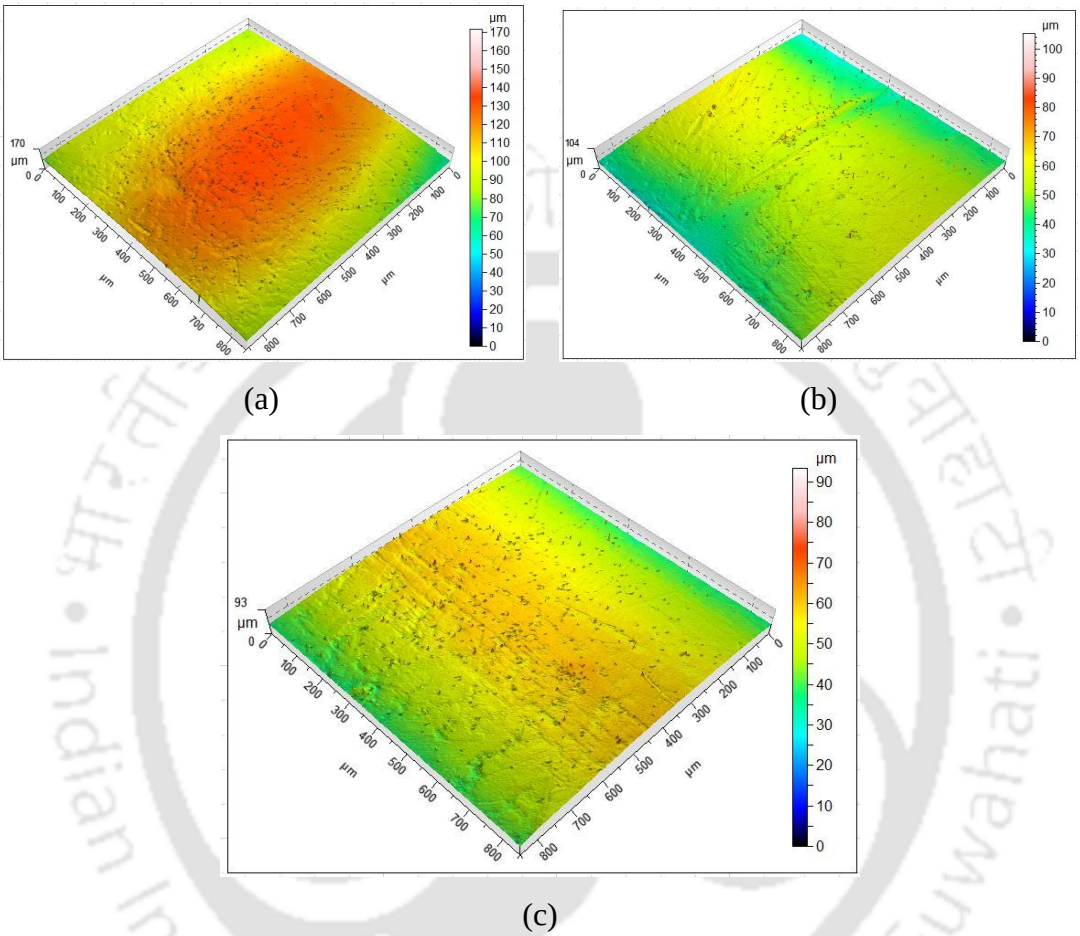

Fig. 4.16 3D surface profile of electromagnetic crimped samples with (a) threaded, (b) knurled, and (c) plain base

4.3 Summary

In this study, it was found that the strength of the joint increases significantly with the increase in the amount of discharge energy from the capacitor bank. Pull-out test and compression-shear test results were revealed that the joint strength obtained with the threaded profile on the steel rod was strongest among threaded, knurled and plain surface profile on the steel rod. The EMC of the Cu-Steel composite rods have resulted in an increase in the hardness values of the each component with their base parts. The increase in the hardness values were due to crimping layer deformation and their strain hardening at the time of high-velocity impact. Surface

profiles of the crimped samples with three types of profiles on the steel rod at 5.3 kJ of discharge energy was analyzed. It was found that surface roughness (R_a in μm) values of the crimped samples on the threaded base was highest among threaded, knurled and plain surface profile steel rod sample. Hence, composite rods produced with threaded type of surface profile on the steel rod can be recommended for higher strength with marginal high surface roughness. But, plain surface profile can be recommended for better surface finish with very low mechanical strength. Knurled surface profile on the steel core can be recommended for good strength as well as good surface finish.

.----------*----------*----------.

भारतीय प्रौद्योगिकी संस्थान गुवाहाटी
Indian Institute of Technology Guwahati

5 Influence of the Base Profiles on Aluminum-Steel Joint Quality

OVERVIEW

This chapter describes the analysis of the properties and shape of a joint of semi-finished products in the form of aluminum crimped steel rods obtained by the electromagnetic crimping technique. For this study three types of profiles, namely threading, knurled, and plain profiles were created on the steel 1020 base. The variation in the joint strength and the microstructure of the joint with the change in profile was analyzed and compared. The effect of type of profiles as well as other main process parameters such as discharge energy, radial gap on the joint strength was studied. The crimped interface was observed and analyzed by using optical microscopy images. The mechanical strength of the bond was evaluated by pull-out test. The results of the pull-out test revealed that the threaded profile on the steel rod gives the highest strength in comparison to the other profiles. The microstructure of the obtained joint showed that there was no gap between the Al tube and the steel rod at 5.3 kJ of discharge energy. There was an increase in the micro-hardness of the analyzed layers compared to the base materials, the reason for the increase is probably due to deformation of the tube layer during electromagnetic crimping and their strain hardening. Surface roughness (R_a) values of the crimped samples at 5.3 kJ was analyzed and it was found that the R_a value of the sample crimped on the threaded base was highest among threaded, knurled, and plain base samples. Vicker's micro-hardness tests were also done to analyze the change in hardness due to high velocity collision.

5.1 EMC of Al-Steel Bimetallic Rods

An aluminum alloy having a thickness of 0.6 mm is used for the flyer tube, and steel 1020 is used as the material for inner rod. The 10 kJ electromagnetic processing system with a capacitance of 90 μF and a maximum discharge voltage of 15 kV was used for the experiments. The coil is twined using circular wire having an outer diameter of 5 mm. The initial dimensions of tubes and rods used for EMC are summarized in Table 5.1.

Table 5.1 Dimensions of the tube and rods used for EMC

No. of set/sample	Outer diameter of Al tube [mm]	Length of Al tube [mm]	Wall thickness [mm]	Diameter of Steel rod [mm]	Length of Steel rod [mm]	Stand-off distance [mm]
01	10.5	80	0.6	8.5	50	0.4

Only the profile on the inner rod was varied in the experiments, and the other dimensions were kept constant. The wall thickness of the flyer tube and the gap between the flyer tube and the base rod is 0.6 mm and 0.4 mm, respectively.

In the majority of published literature [27], plain profile on the base was used for EMC of bimetallic tubes or rods. In the present study plain profile, threaded and knurled profiles on the base were produced for EMC. Field shaper inside the solenoid coil with 11 numbers of turns, with a pitch of 8 mm was used as a working tool. The complete description of the working zone in the EMC to produce bimetallic rods is shown in Fig. 5.1. The dimensions of the stepped type field shaper used in the study are shown in Fig. 5.2. The chemical composition of the materials of Al tube and steel rod was analyzed by energy dispersive X-ray spectroscopy (EDAX). The chemical composition of the Al tube and steel rod in the weight percentages are tabulated in Table 5.2 and Table 5.3 respectively.

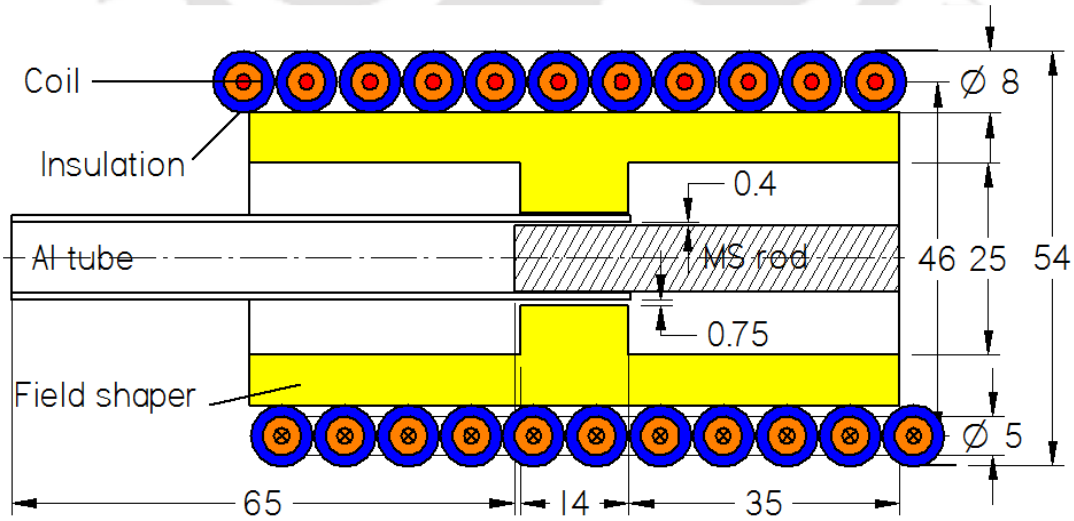

Fig. 5.1 Complete description of working zone of EMC

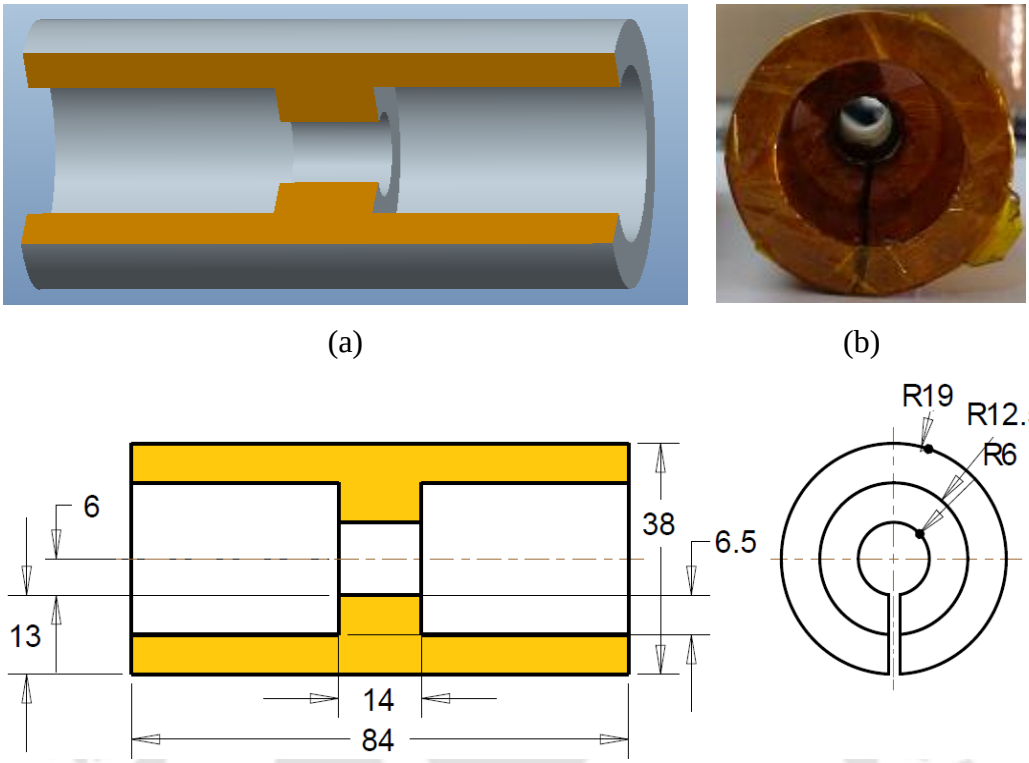

Fig. 5.2 Field shaper used in EMC (a) cross-section of the CAD model, (b) an actual image of the field shaper, and (c) dimensions of the field shaper

Three sets of samples were prepared for testing, each consisting of aluminum tubes and steel rods. The CAD model along with the three types of profiles created on the steel rod is shown in Fig. 5.3. Typical current waveform (first and second current cycle) obtained at three different discharge energies was superimposed and shown in Fig. 5.4. These current signals were measured on the Oscilloscope by using the Rogowski probe inside the working zone. The current signal having a damping and oscillating current flows through a multi-turn solenoid coil for the duration of about 65 μs. The peak current and frequency of the discharge current flowing through the coil corresponding to the six different discharge voltages are tabulated in Table 5.4. Peak values of the first and second current cycle was studied. The measured discharge current's first and second peak value for different discharge energy obtained from the oscilloscope is shown in Fig. 5.5. An increase in discharge energy leads to an increase in the peak current. Although, the frequency of the circuit remains almost constant with the increase in the discharge energy.

Table 5.2 Chemical composition of the Al tube

Alloy	Analysis (wt. %)						
	Al	Fe	Mn	Ti	Zn	Si	Cu
Al 1050	Balance	1.1	0.1	0.1	0.1	0.5-0.6	0.1-0.2

Table 5.3 Chemical composition of the steel 1020 rod

Alloy	Analysis (wt. %)								
	C	Cr	Mn	Cu	Ni	P	Si	S	Fe
Steel 1020	0.16-0.25	0.15-0.25	0.3-0.4	0.1-0.2	≤0.1	≤0.1	0.2-0.3	0.1-0.4	Balance

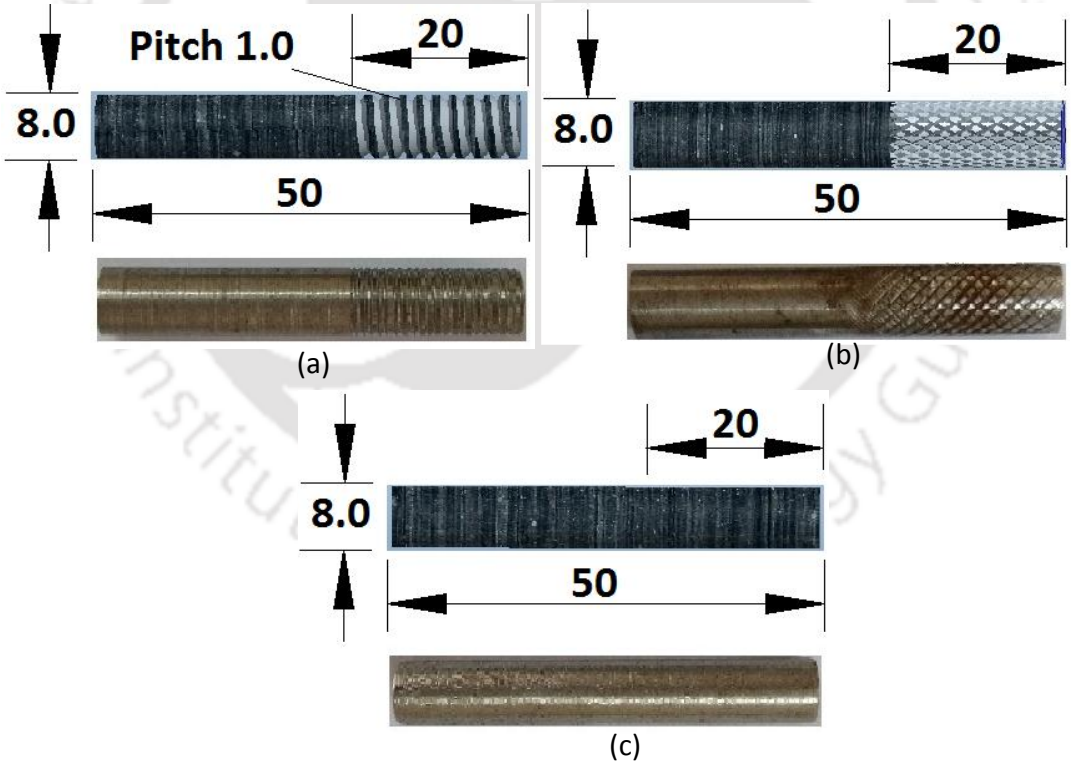

Fig. 5.3 CAD model along with the actual picture of the three types of profiles (a) threaded profile, (b) knurled profile, and (c) plain profile created on the base

Table 5.4 Process parameters used in the experiments

S No	Voltage (kV)	Energy (kJ)	Peak current (kA)	Time-period (µs)	Frequency (Hz)
1.	7.1	2.3	53.76	65.6	15244
2.	7.8	2.7	57.60	65.2	15337
3.	8.6	3.3	67.20	64.6	15480
4.	9.3	3.9	71.04	64.4	15528
5.	10.1	4.6	76.80	64.2	15576
6.	10.9	5.3	84.48	64.0	15625

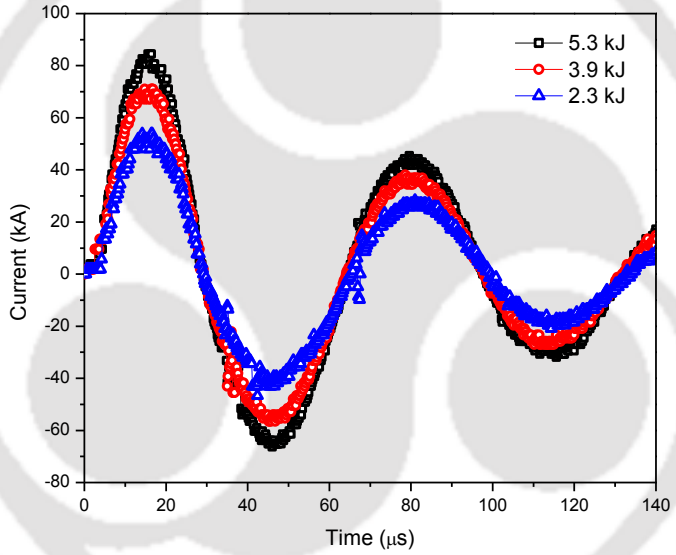

Fig. 5.4 First and second current cycle of the measured discharge current waveform at three different energy level

5.2 Investigation of Geometric Changes and Quality of the Bimetallic Rod after EMC

After discharge of energy from the capacitor bank, straight bimetallic rods with a durable joint without any metallurgical bond over the feed length was obtained, without necking and curving. Successfully crimped samples with three profiles threaded, knurled and plain at six various discharge energies are shown in Fig. 5.6. The EMC resulted also in a slight reduction of the aluminum tube length, with a simultaneous slight thickening of the aluminum layer in

the samples. Mroz et al. have also found that there is an increase in the thickness in the explosive crimping with a simultaneous reduction in the length of the tube [65].

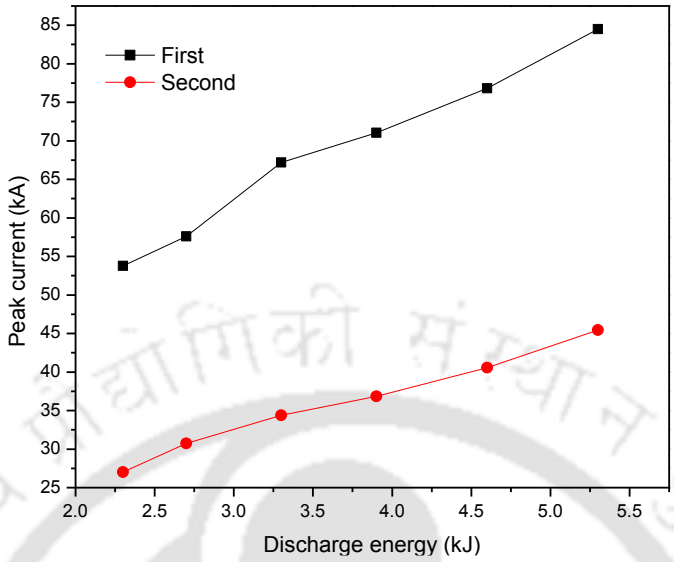

Fig. 5.5 Measured discharge current first and second peak value at different discharge energy

Fig. 5.6 Electromagnetic crimped samples with (a) threaded profile, (b) knurled profile, and (c) plain profiles on the base

The cross-section of the crimped samples at three discharge energies 3.9 kJ, 4.6 kJ and 5.4 kJ with three profiles was cut and its diameter was measured. The cross-sectional view and their dimensions of the Al-steel bimetallic rods after EMC are shown in Fig. 5.7. In Fig. 5.7 D is the outer diameter of the bimetallic rod, C and S is the circumference and cross-sectional area of

the bimetallic rods, respectively. It has been observed from the Fig. 5.7 that plain rod profile resulted in the complete crimping of Al tube on the circumference of steel rod. Whereas threaded and knurled profiles show profile gap in the crimped bimetallic rod. Plain profile resulted in smooth surface, whereas threaded and knurled profile resulted in wavy surfaces.

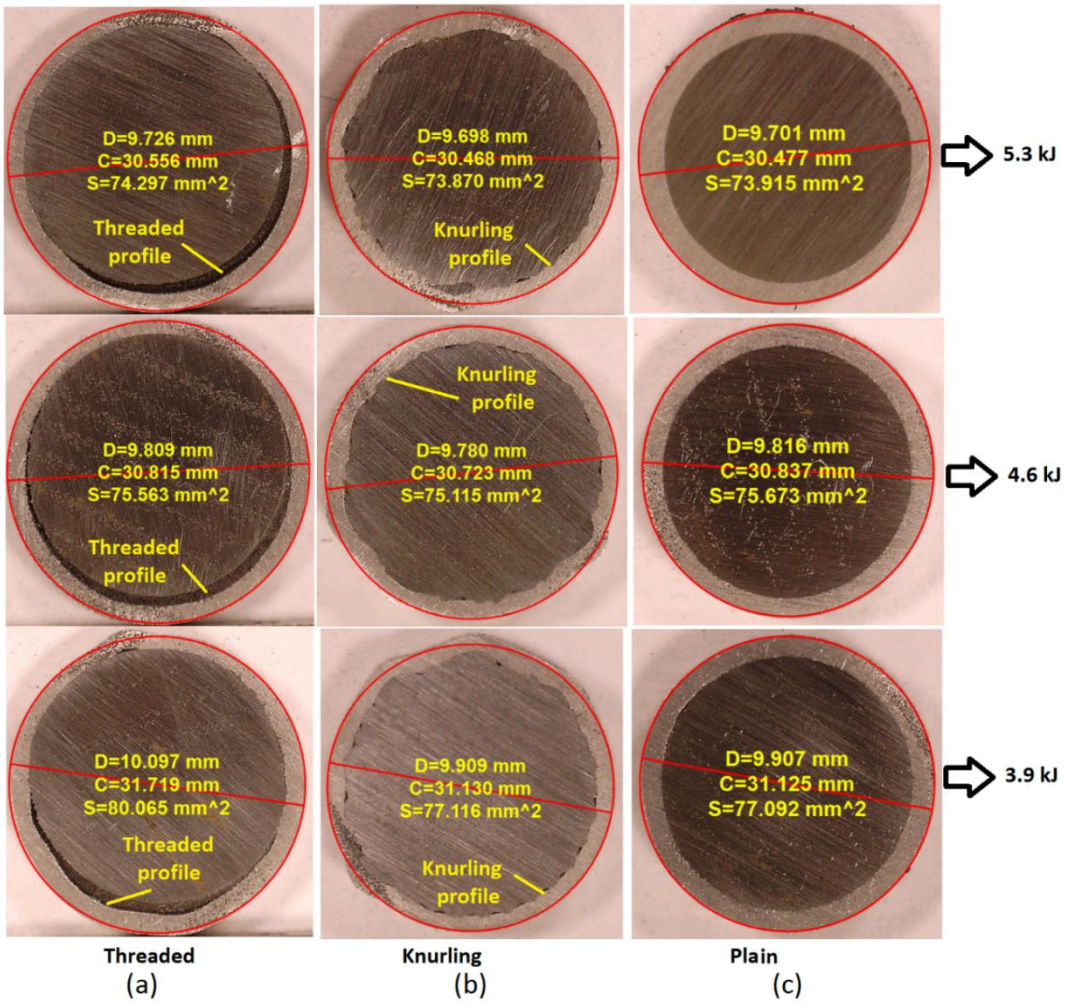

Fig. 5.7 Shape and dimensions of bimetallic rods after EMC with (a) threaded profile, (b) knurled profile, and (c) plain profile on the base

At lower values of discharge energy the outer diameter of the bimetallic rod was found to be larger as compared to that of outer diameter of the bimetallic rod at higher discharge energies. Higher energy led to maximum magnetic pressure acting on a tube and resulted in the full crimping of tube with an optimum crimped diameter, which was almost equal to the rod diameter plus tube thickness i.e. 9.7 mm. The measured diameter and original diameter of the flyer tube for three profiles and at three discharge energy values are shown in Fig. 5.8.

5.3 Joint Regions Structure

The mechanical properties of the joints are examined by the pull-out testing of the joints and the nature of the joining of the bimetallic rod layers. Pull-out tests were carried out for the crimping joints under six different discharge energies of 2.3 kJ, 2.7 kJ, 3.3 kJ, 3.9 kJ, 4.6 kJ, and 5.3 kJ. The profiles made on the steel rods are plain, threaded and knurled. Two failure modes of the joints during pull-out tests are shown in Fig. 5.9. Failure separation mode, which is defined by the failure of the joint due to separation of the tube and rod and failure crack mode is defined by the crack failure in the weak stock material i.e. aluminum.

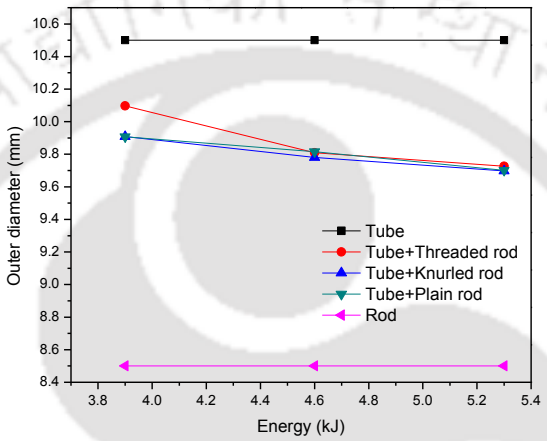

Fig. 5.8 Comparison of outer diameter of the bimetallic rods measured at three different discharge energies with Al tube and steel rod

The normalized load-extension curves for the specimens with three profiles at different energies are shown in Fig. 5.10. In the first case, the joints made with plain profile, and for six different energies, the joints were failed with separation mode. For the second case, the joints made with knurled profile and having energies 2.3 kJ, 2.7 kJ, 3.3 kJ and 3.9 kJ the joints were failed with separation mode whereas, for energies 4.6 kJ and 5.3 kJ the joints were failed with crack mode. In third case, the joints made with threaded profile and having energies 2.3 kJ and 2.7 kJ the joints were failed with separation mode but for energies 3.3 kJ, 3.9 kJ, 4.6 kJ and 5.3 kJ the joints were failed with crack mode. When the discharge energy reaches to a particular value, for a specified profile, the fracture of the Al tube would take place. The fracture in the Al tube shows that the pull-out strength of the joints is greater than that of the parent aluminum alloy, and an effective crimping is therefore achieved.

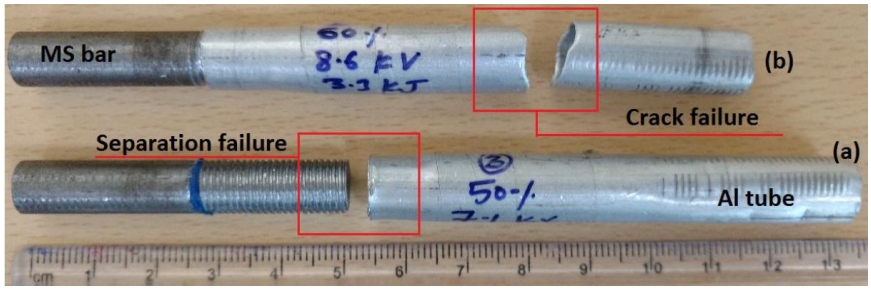

Fig. 5.9 Two failure modes of the joints in pull-out tests (a) separation mode separation failure, (b) crack mode crack failure

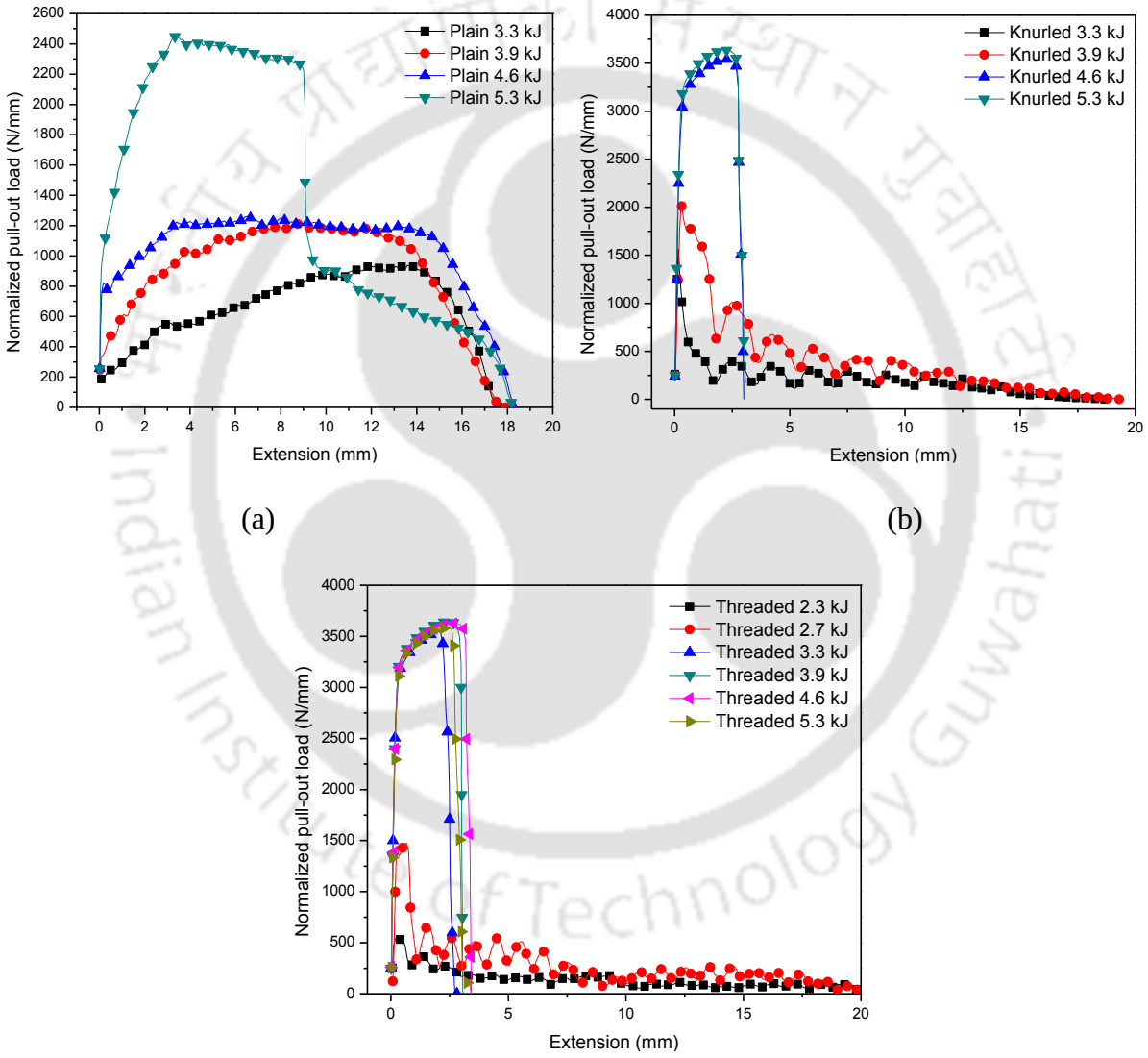

Fig. 5.10 Load-extension plot for (a) plain profile, (b) knurled profile, and (c) threaded profile made on the rod at different energies

Fig. 5.11 shows the load-extension plots comparison of the specimens with three different profile and at same discharge energies. In the first case, the joints produced at 3.3 kJ with plain, threaded and knurled profiles and the joints were failed with separation mode for plain and knurled profiles whereas with crack mode for threaded profile.

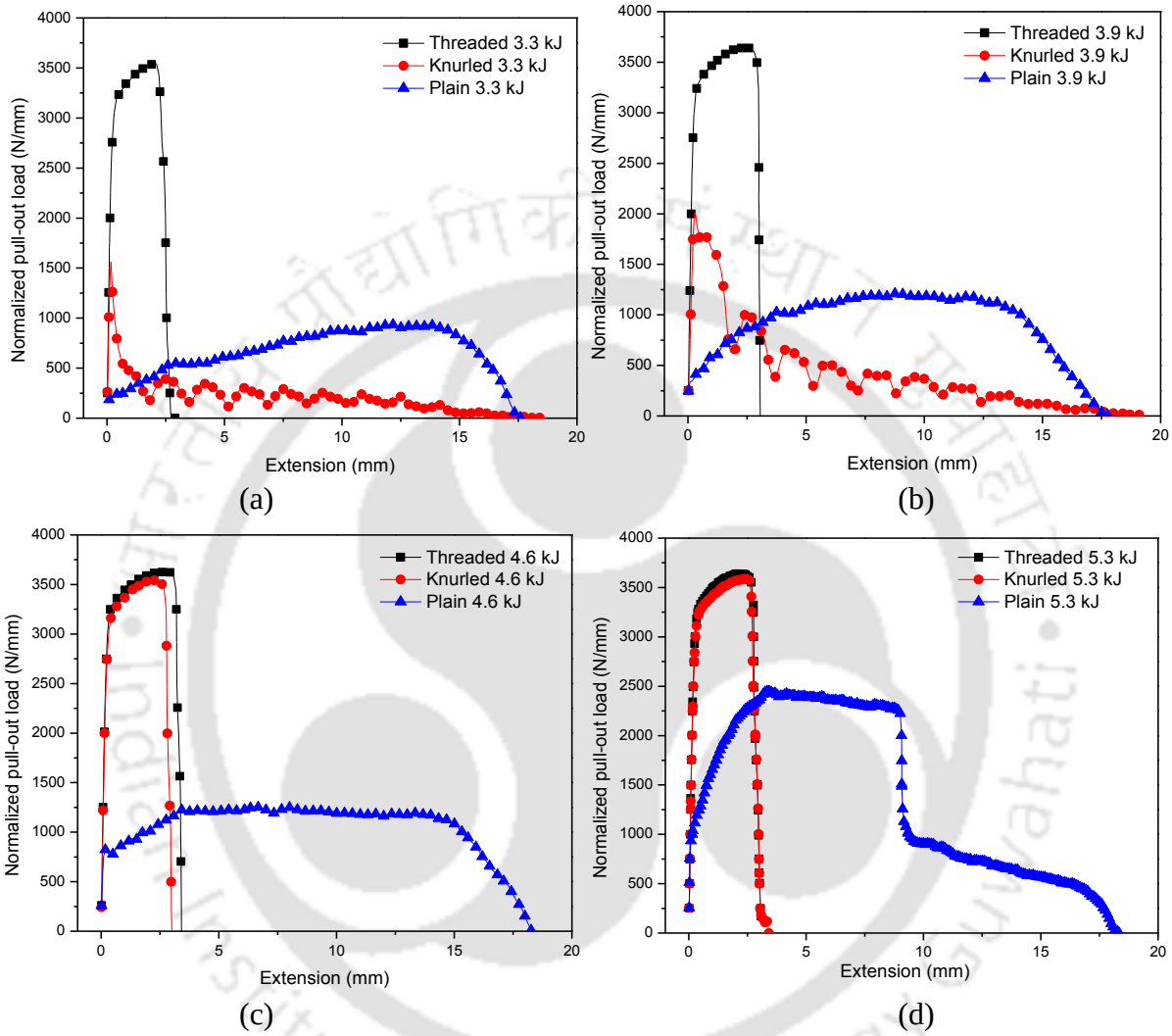

Fig. 5.11 Load-extension plot with three different profile and at four different discharge energies (a) at 3.3 kJ, (b) 3.9 kJ, (c) 4.6 kJ, and (d) 5.3 kJ

In the second case the joints produced at 3.9 kJ with plain, threaded and knurled profiles and the joints were failed with separation mode for plain and knurled profiles whereas with crack mode for threaded profile. In the third and fourth conditions the joints were produced at 4.6 kJ and 5.3 kJ respectively, and the joints were failed with separation mode for plain profile whereas with crack mode for threaded and knurled profiles. The fracture in the Al tube in the tests shows that the pull-out strength of the joints are greater than that of the parent aluminum tube, and an effective crimping is therefore achieved.

The samples failed after the pull-out test with six different discharge energies and having three profiles on the base threading, knurled and plain are shown in Fig. 5.12 (a), (b), and (c) respectively. In the pull-out tests it was found that for the plain profile on the base, the failure of the joint took place with separation mode till 5.3 kJ energy. But, when the profiles created on the base either threading or knurled the failure took place with crack failure mode for more than 3.3 kJ and 4.6 kJ for threaded and knurled profiles respectively.

The normalized maximum pull-out load required in the pull-out tests of the crimped samples for three profiles at 3.6 kJ, 3.9 kJ, 4.6 kJ and 5.3 kJ is plotted in Fig. 5.13(a) and the variation in the normalized maximum pull-out load with the discharge energy is shown in Fig. 5.13(b). Based on the results of the pull-out test it can be concluded that threaded profile made on the steel rod gives better joint strength among plain profile, knurled profile and threaded profile.

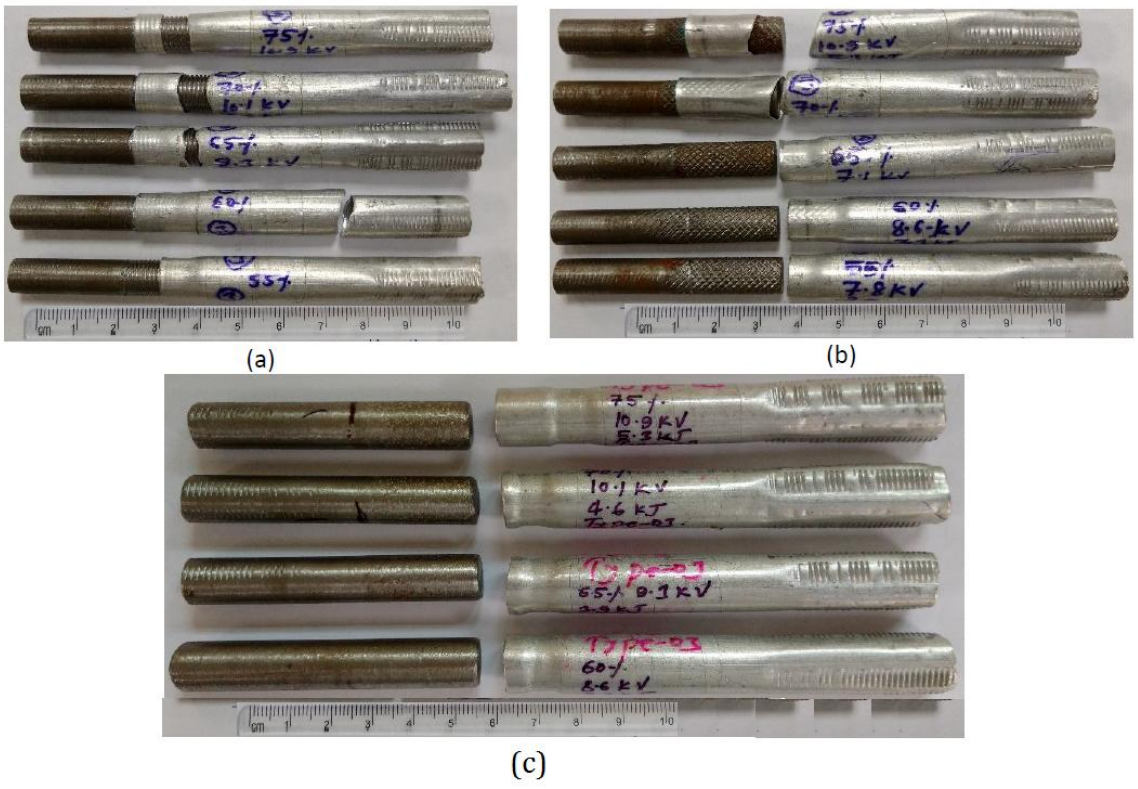

Fig. 5.12 Pull-out test failed samples with (a) threaded profile, (b) knurled profile, and (c) plain profile on the base at five different discharge energies

Fig. 5.14(a) shows the four positions were the Vicker's micro-hardness tests were performed and corresponding results of the micro-hardness value is plotted in Fig. 5.14 (b). Vicker's micro-hardness tests demonstrate that the micro-hardness of aluminum and steel 1020 generally decreases as the distance from the interfaces were increased, which was attributed to

the intense plastic deformation at the interface or near to the interface. The result was rational with the previous works carried out by another researcher [28]. The microscopic images of the hardness measurement is shown in Fig. 5.15.

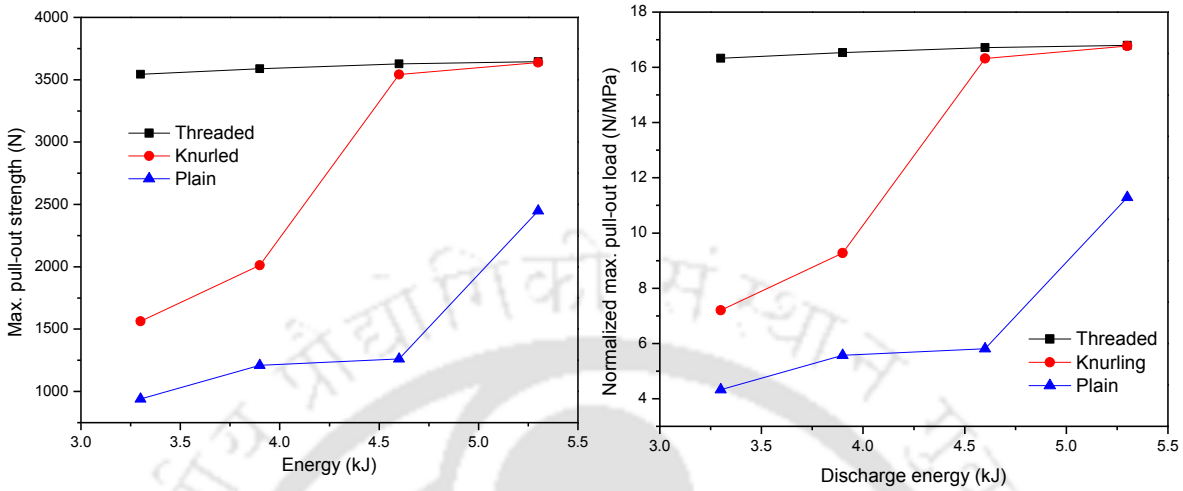

(a) (b)

Fig. 5.13 (a) Variation in the maximum pull-out strength and (b) variation in the normalized maximum pull-out load with the discharge energy plot for three different profiles

Crimped specimen, representative of the successful crimping experiments, was regarded on the micro scale. In the micro-section, it can be seen in Fig. 5.16(a) that there were no gap, where the flyer was actually crimped on the base with plain profile.

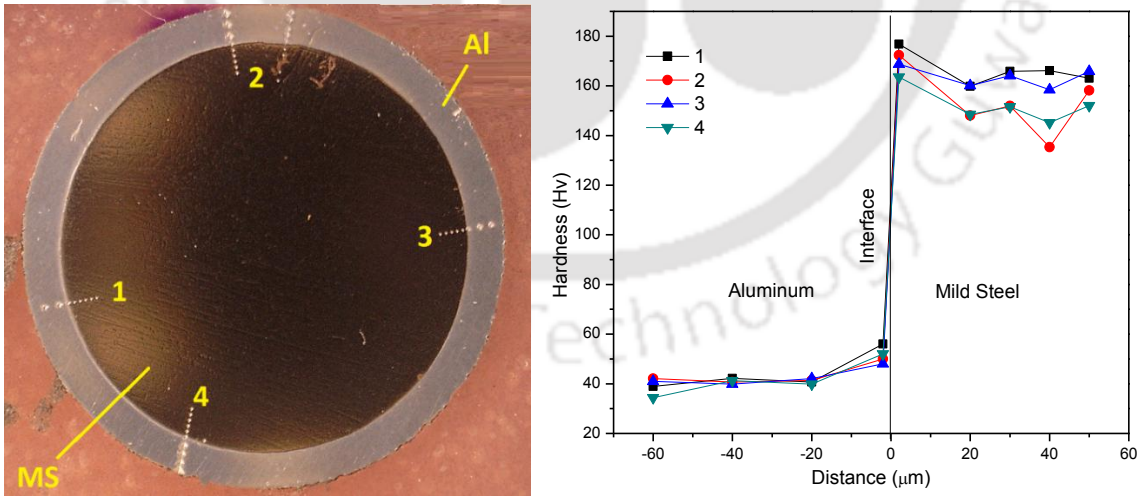

(a) (b)

Fig. 5.14 (a) Hardness measured at four different locations and, (b) hardness variation vs. distance plot at four different locations on crimped sample

Whereas in case of threaded and knurled profile, there was a gap of size equal to the thread size and knurl size at 5.3 kJ of discharge energy. Microscopically, neither metallurgical bond nor the interlayer was observed at the interface and a mechanical joint was obtained by EMC.

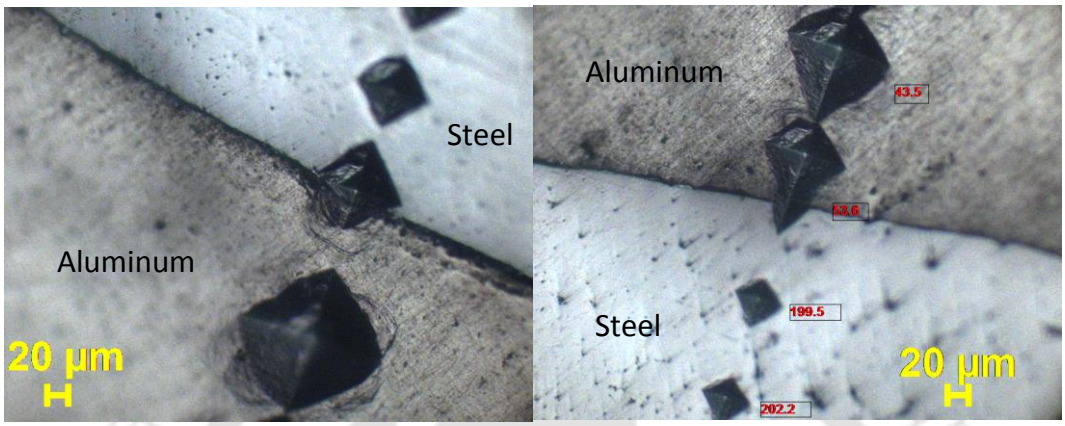

Fig. 5.15 Microscopic image of location of hardness measurement

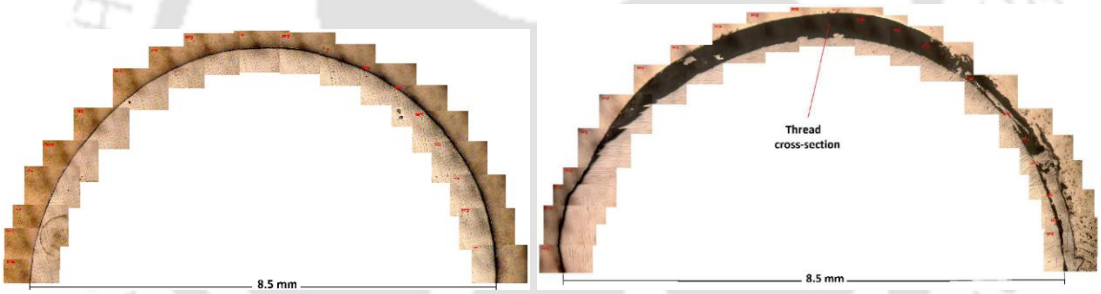

(a) (b)

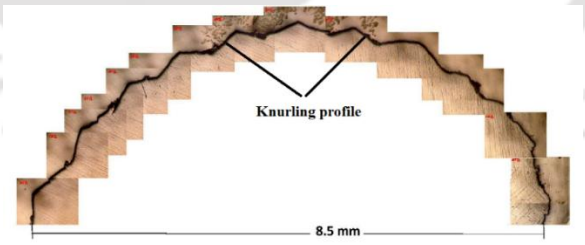

(c)

Fig. 5.16 Optical microscope images at the interface of the electromagnetic crimped sample having (a) plain profile, (b) threaded profile, and (c) knurled profile at 5.3 kJ energy

Surface profile of the electromagnetic crimped samples with base having three types of profiles was analyzed using high precision non-contact computerized surface profilometer. The field of

view of a non-contact 3D profiler was 0.825 mm × 0.825 mm and focal distance was 4.7 mm. Surface roughness values of the crimped sample at 5.3 kJ of discharge energy with three types of profiles on three elementary areas are tabulated in Table 5.5 and the normalized surface roughness with the thickness of the tube is shown in Table 5.6. It was found that the Ra value of the sample crimped on threaded base was larger than knurled base and that of plain base. The three-dimension surface profile of electromagnetic crimped samples at 5.3 kJ with (a) threaded base, (b) knurled base, and (c) plain base are shown in Fig. 5.17. It has been observed that plain profile resulted in the smooth surface of the bimetallic tube. Threaded profile resulted in highest surface roughness among the plain, threaded and knurled profiles. It can be concluded from the surface roughness measurement that plain profile shows best surface finish among the plain, threaded and knurled profiles.

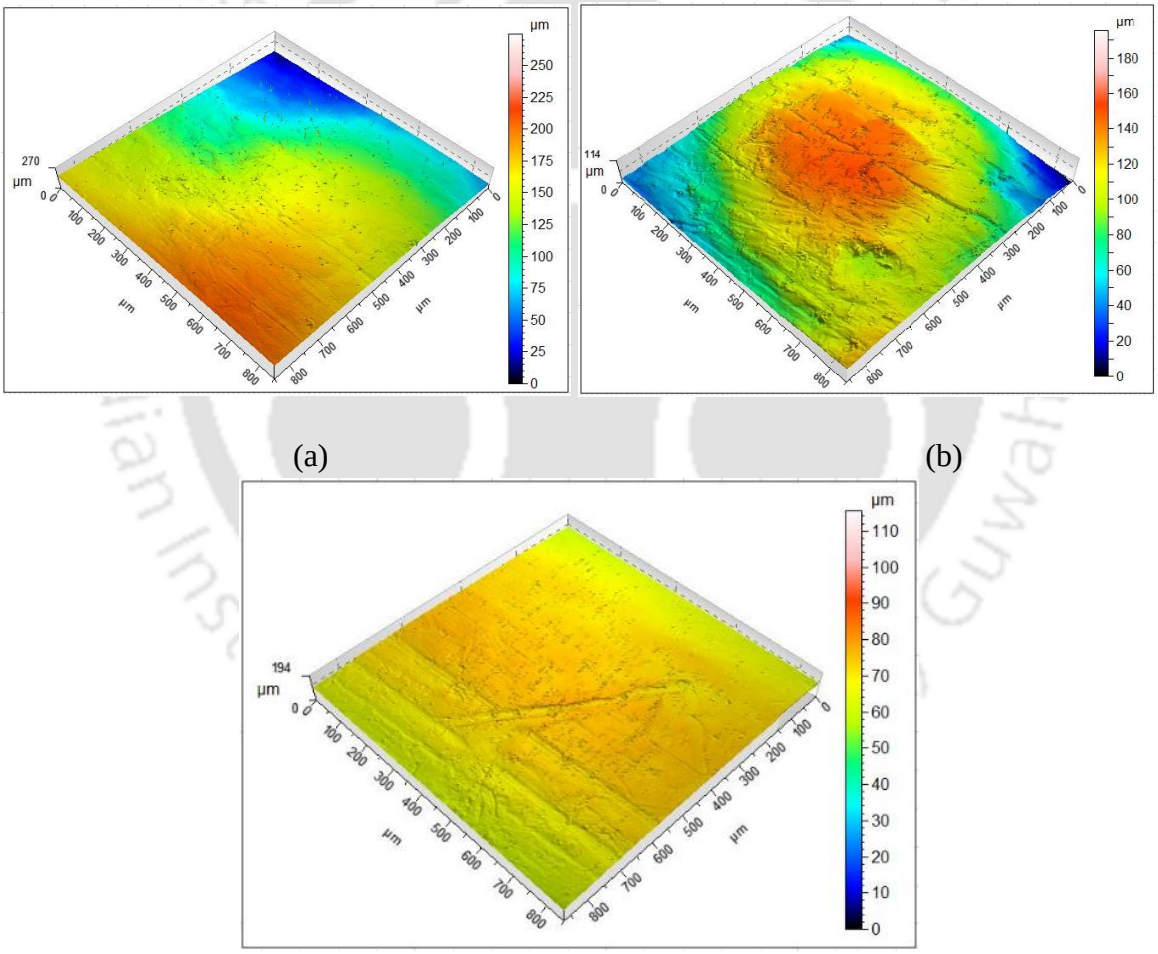

Fig. 5.17 Surface profile of electromagnetic crimped samples at 5.3 kJ with (a) threaded base, (b) knurled base, and (c) plain base

Table 5.5 Surface roughness (μm) values of the EMC samples at 5.3 kJ

	Threading				Knurled				Plain			
	1	**2**	**3**	**Avg.**	**1**	**2**	**3**	**Avg.**	**1**	**2**	**3**	**Avg.**
R_a (µm)	1.50	1.38	1.44	1.44	1.01	1.04	0.97	1.01	0.59	0.76	0.81	0.72

Table 5.6 Normalized surface roughness values of the EMC samples at 5.3 kJ

	Threading				Knurled				Plain			
	1	**2**	**3**	**Avg.**	**1**	**2**	**3**	**Avg.**	**1**	**2**	**3**	**Avg.**
Noramalized R_a (10^{-3})	3.0	2.76	2.88	2.88	2.02	2.08	1.94	2.02	1.18	1.52	1.62	1.44

5.4 Summary

The application of the EMC method has resulted in a semi-finished product in the form of Al-Steel bimetallic rod, which is characterized by a uniform distribution of the crimping layer on the core perimeter and a negligible ovality in the cross-section. The discharge energy through the capacitor bank significantly increases the strength of the joints of the individual layers. Al tubes were successfully crimped on the steel rod having three types of profiles threaded, knurled and plain respectively. The joints obtained with a threaded profile on the base give strongest joint strength among threaded, knurled and plain profiles on the base. The EMC of Al-steel bimetallic rods has resulted in an increase in the micro-hardness of the layers analyzed compared to the base materials, the reason for the increase is probably due to crimping layer deformation during EMC and their strain hardening. Surface roughness (R_a) values of the crimped samples with three types of profiles on the base at 5.3 kJ were analyzed and it was found that the R_a value of the sample crimped on the threaded base was highest among threaded, knurled and plain base sample. Hence, bimetallic rods obtained with a threaded profile on the base can be recommended for higher strength with marginal high surface roughness as compared to the plain and knurled profile. Whereas bimetallic rods produce with the plain profile on the base can be recommended for better surface finish with very low joint strength as compared to threaded and knurled profiles. Knurled profile can be recommended for combined advantages of increase strength with better surface finish.

.----------*----------*----------.

भारतीय प्रौद्योगिकी संस्थान गुवाहाटी
Indian Institute of Technology Guwahati

6 Effect of Field Shaper Geometry on EMC

OVERVIEW

The objective of this work was to examine the effect of field shaper geometry used to manufacture the composite rods. Copper-Aluminum composite rods is a substitution for copper rods, result in both cost and weight reduction. An attempt was made to concentrate the distribution of the electromagnetic pressure, fulfilled by modifying the geometry of the field shapers. The application of field shaper in the process not only increases the effectiveness of the process but also increases the life or strength of the working coil. The effect of geometry of three types of field shaper on the plastic deformation of the composite rod was investigated to facilitate the field shaper design. The field shaper variation was done by changing the cross-section namely tapered, step-tapered and stepped. The microstructure of the crimped joint interface was analyzed. The mechanical properties of the crimped joint were evaluated by compression-shear test, pull-out test, leak test, and joint resistance. It was found that the step-tapered field shaper results better in terms of uniformity in crimp quality, joint strength in compression, joint strength in tension, joint resistance, joint leakage and surface finish of the crimped sample among the three types of field shaper. This work will be of use for designing of field shaper for producing joint by electromagnetic crimping.

6.1 Methodology

EMC uses Lorentz force to accelerate flyer tube on the stationary base rod. The sudden discharge of current cause's electromagnetic field having high magnitude and being cut by flyer tube, then the induced current or eddy current in the flyer tube also develops electromagnetic field having opposite direction. The result of two opposing magnetic field causes a Lorentz force or magnetic force on the flyer tube. As a result flyer tube was accelerated away from the field shaper or coil tool and collides with the base rod with very high velocity. The high-velocity impact of the flyer tube on the base rod causes the crimping of a tube on the rod. The initial and final stages of the process involved in the EMC are shown in Fig. 6.1.

6.1.1 Materials and equipment

The EMC experiments were performed on the tube to rod assembly by using an electromagnetic processing system (EMPS). The EMPS used have two capacitors of 45 μF with total discharge energy of 10 kJ. The EMPS transforms the low-voltage power supply 440 V, having 50 Hz frequency into a high voltage power supply having a range of 0-15 kV, with 16 kHz frequency. The discharge current with peak current 100-150 kA, passes through a multi-turn solenoid coil, which produces an eddy current in the field shaper. The produced eddy current provides a Lorentz force that causes the collision of the flyer copper tube onto the stationary inner aluminum rod. The effective length or working length was 14 mm which causes deformation in the flyer tube.

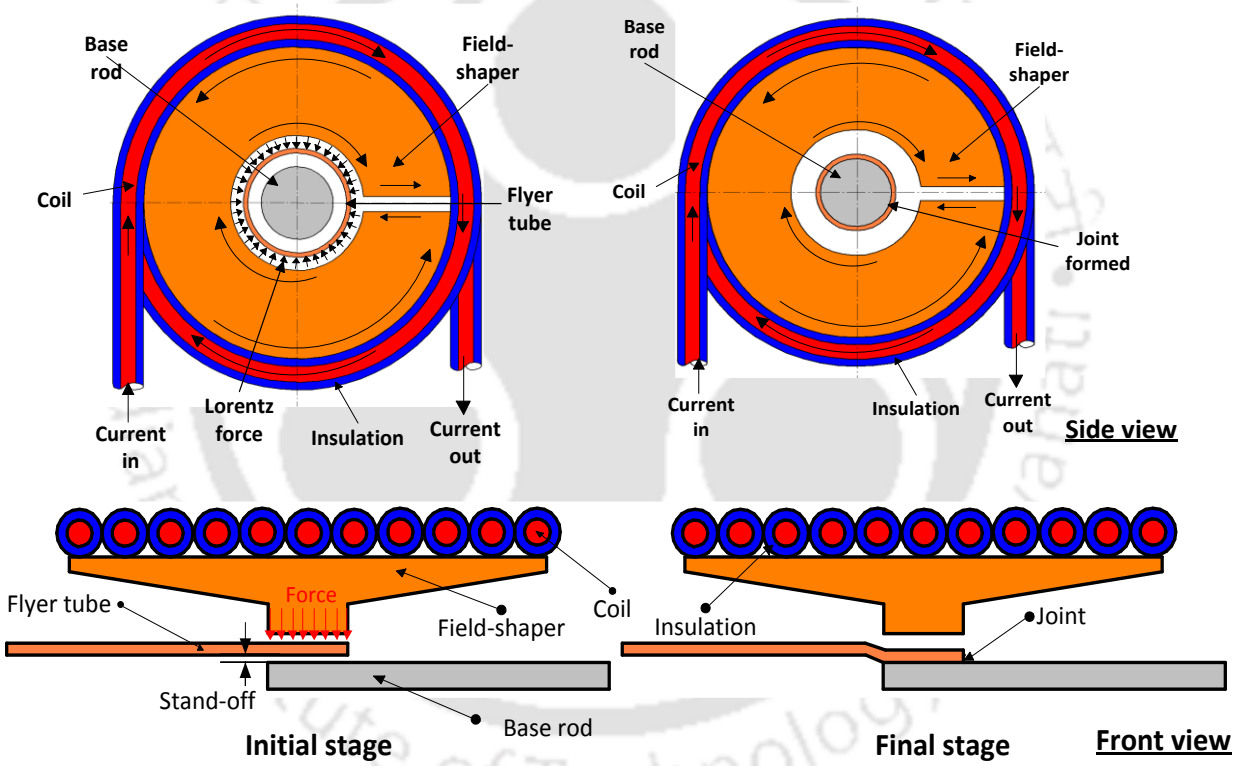

Fig. 6.1 Initial and final stages of the EMC process (side view and front view)

In experiments, a copper tube having a thickness of 0.64 mm was used as a flyer tube and aluminum rod was used as a stationary base material. The materials used was standard commercially available materials and their standard available chemical composition was compared with the analyzed one by using EDX. Chemical compositions of Cu flyer tube and aluminum 1050 base rod is given in Table 6.1. . The actual image of the cross-section of three

field shapers are shown in Fig. 6.2 and the detail dimensions of the multi-turn solenoid coil are shown in Fig. 6.3.

The detail dimensions of the flyer tube and base rod used are given in Table 6.2 and the mechanical properties of the materials of flyer tube and the base rod are given in Table 6.3. The gap of 1.50 mm between the coil and the field shaper was maintained. The standoff between the flyer tube and the base rod was 0.27 mm, which is about half of the thickness of the flyer tube.

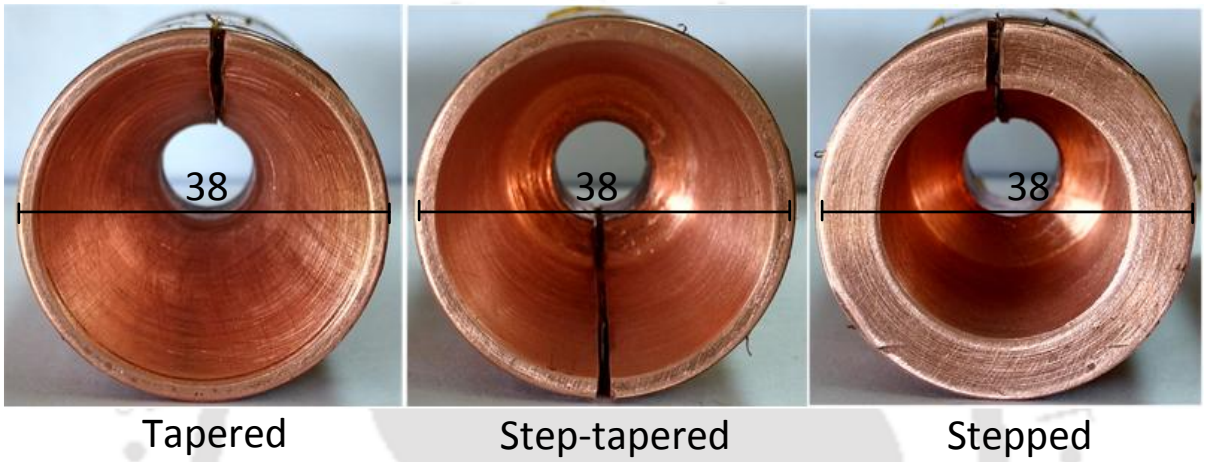

Fig. 6.2 Cross-section of the tapered, step-tapered and stepped types of field shaper

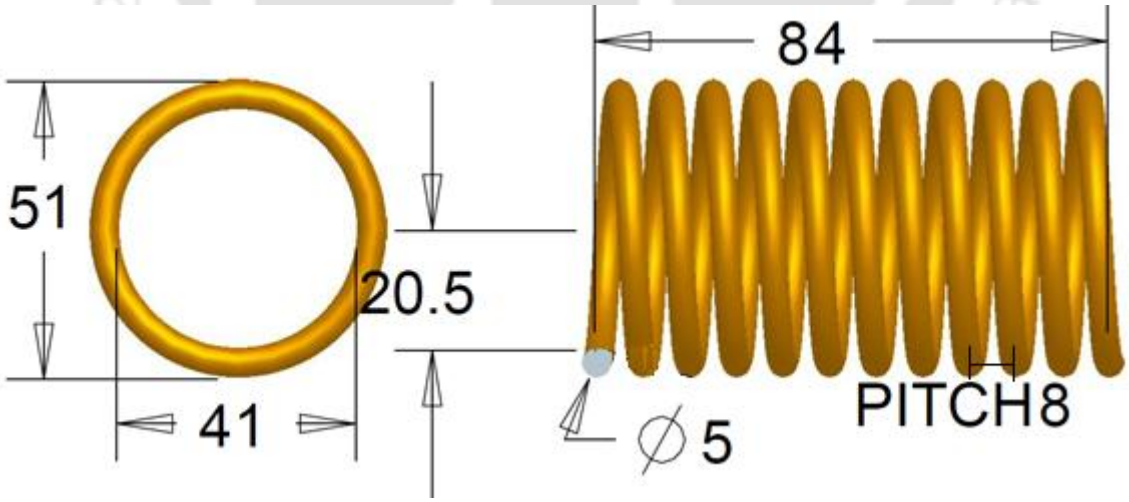

Fig. 6.3 Detail dimensions of the multi-turn solenoid coil used in the experiment

The multi-turn solenoid coil used in the experiments was composed of a total 11 turns and three types of field shaper which focused the electromagnetic field in the 14 mm length

work zone. The inner diameter of all three field shapers was 12 mm and having a total length of 84 mm. The frequency of the discharge pulse current was measured with the help of Rogowski coil into the oscilloscope. Experiments were carried out on samples with Cu flyer tube and aluminum inner rod. The detail dimensions of three types of the field shaper namely tapered, step-tapered and stepped used in the experiment are shown in Fig. 6.4.

Table 6.1 Chemical compositions of copper tube and aluminum rod

Material	**Analysis (wt. %)**								
	Zn	**Pb**	**Cu**	**Fe**	**S**	**Sb**	**P**	**Sn**	**Si**
Copper	0.3	0.1-0.2	Rest	0.1-0.2	0.1	0.1	0.1	0.1	0.1
	Al	Fe	Mn	Ti		Zn		Si	Cu
Al 1050	Balance	1.1	0.1	0.1		0.1		0.5-0.6	0.1-0.2

6.1.2 Pull-out test

The successfully crimped samples at five different discharge energy 3.3 kJ, 4.0 kJ, 4.6 kJ, 5.3 kJ, and 6.2 kJ with three types of field shaper are shown in Fig. 6.5. To evaluate the joint strength in tension, the pull-out test of the crimp interface of the Cu tube crimped on the aluminum rod was subjected to a pulling load or tensile load. A total 15 samples at five different values of discharge energies with three types of field shaper were tested.

Table 6.2 Dimensions and materials of the tube and rod

Specimen	**Materials**	**Outer diameter**	**Inner diameter**	**Length**	**Thickness**	**Stand-off**
Flyer tube	Copper	9.52 mm	8.24 mm	60 mm	0.64 mm	-
Base rod	Al 1050	7.70 mm	-	60 mm	-	0.27 mm

Finally, the joint strength was evaluated by performing the tests using a UTM at a speed of 0.5 mm/min. Initial and final stages of the pull-out test performed on the UTM is schematically shown in Fig. 6.6 (a) and the arrangement made for the performance of the pull-out test is shown in Fig. 6.6 (b). In this test, crimped length was 14 mm and gripping length was about 25 mm in the UTM jaw.

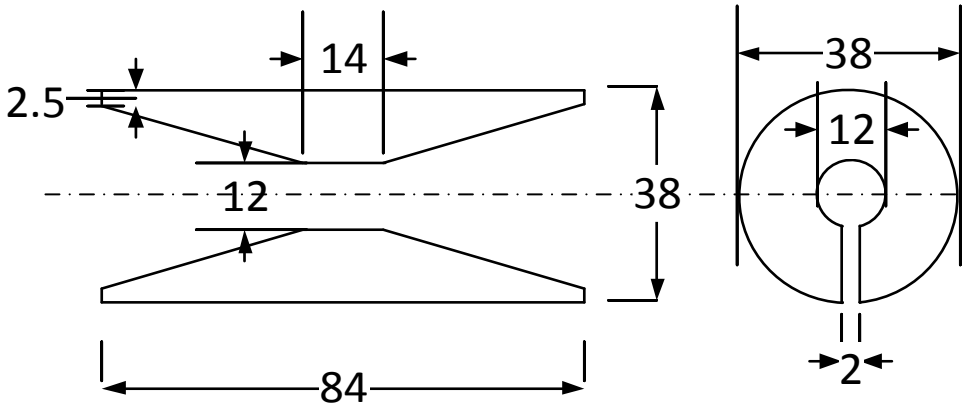

(a) Tapered

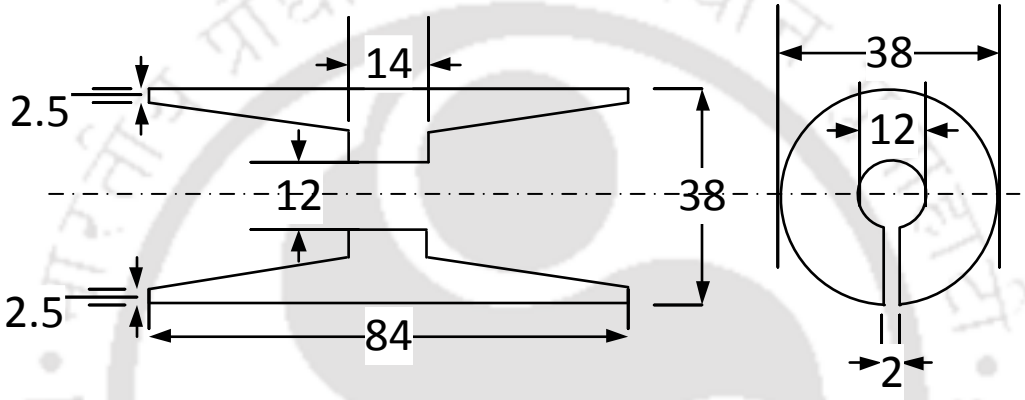

(b) Step-tapered

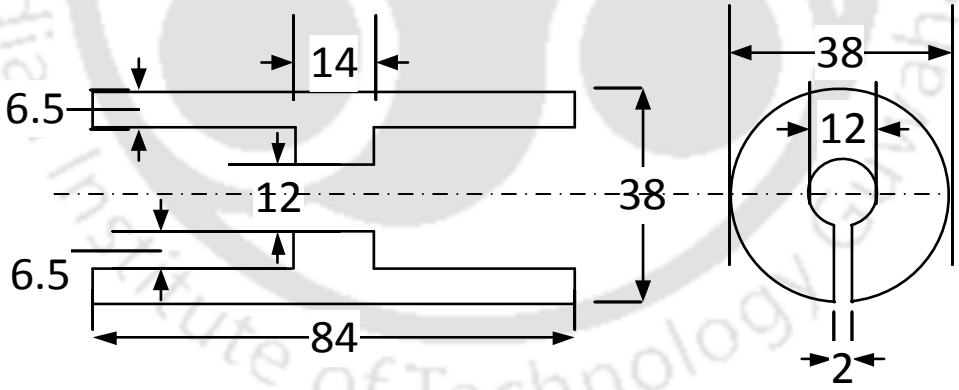

(c) Stepped

Fig. 6.4 Dimensions of the tapered, step-tapered and stepped types of field shaper

6.1.3 Compression-shear test

To evaluate the strength of the joint in compression, the compression-shear test was performed. In this test, the crimp interface of the Cu tube crimped on the aluminum rod was subjected to compressive load with the help of indenter. The samples crimped at five different energies were cut continuously by using wire electric discharge machine (WEDM), in the perpendicular

direction of the length. A total 30 samples at five different values of discharge energies, two samples from each field shapers were tested. The joint strength was evaluated by applying compressive load using a UTM at a speed of 0.5 mm/min. Initial and final stages of the compression-shear test performed on the UTM is schematically shown in Fig. 6.8. In compression-shear tests, the thickness of the sample was 1.5 mm.

Table 6.3 Mechanical properties of the materials

Part	**Tube**	**Rod**
Material	Copper 1010	Al 1050
Density (kg/m^3)	8940	2705
Young's modulus (GPa)	54	69
Poisson's ratio	0.31	0.33
Ultimate tensile strength (MPa)	227	76

Fig. 6.5 Sample manufactured by tapered, step-tapered and stepped field shapers

Thereby, the joint strength in shear (S_{sy}) of the crimped joint, which according to equation (6.1) can be calculated from the maximum compressive load (F_{max}) in the load-extension plot and crimping area (A). The crimping area (A) can be calculated by multiplication of circumference of the rod (πd) and thickness of the sample (t).

$$S_{sy} = \frac{F_{max}}{A} = \frac{F_{max}}{\pi dt} \tag{6.1}$$

For the compression-shear test to perform, an indenter and a holder was manufactured. First, the samples were kept in the holder and then compressive load was gradually applied with the help of an indenter. Because of the load, the copper tube gets separated from the aluminum rod, shown in Fig. 6.8.

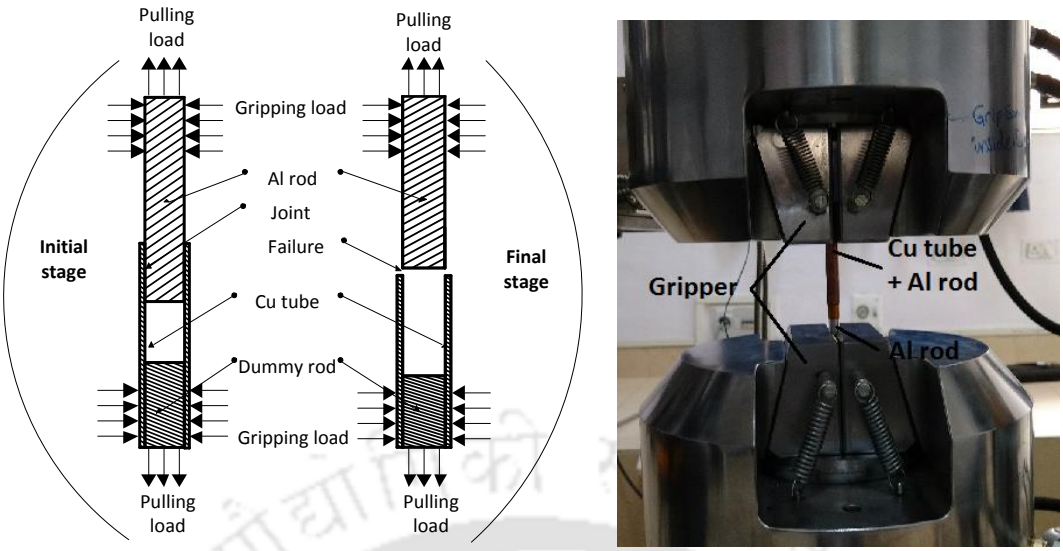

(a) (b)

Fig. 6.6 (a) Initial and final stages of the pull-out test, (b) arrangement for pull-out test at UTM

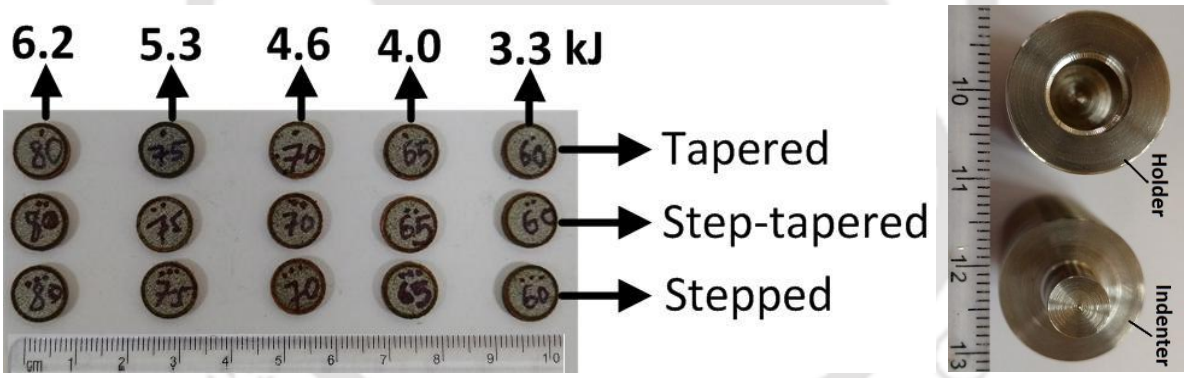

(a) (b)

Fig. 6.7 (a) Compression-shear test samples prepared by three types of field shaper tapered, step-tapered, and stepped (b) fixture for compression-shear test

6.2 Results and discussion

6.2.1 Discharge current measurement

First of all the discharge current passing through the multi-turn solenoid coil was measured experimentally by a Rogowski coil and oscilloscope to analyze the parameters. Figure 6.9 shows the discharge current curve at five different values of discharge energy. Different Process parameters associated with the experiments are tabulated in Table 6.4.

6.2.2 Change in thickness of the crimped tube

The thickness of the copper tube in the crimped samples was measured by using a digital microscope. The thickness of the successfully crimped samples at 6.2 kJ with three types of field shaper was measured. The cross-sectional view and the values of the maximum and the minimum thickness at different positions of the copper tube in the crimped samples are shown in Fig. 6.10. The initial thickness of the copper tube was subtracted from the measured thickness of the tube and change in the thickness of the tube at different positions was plotted. The position where the thickness was measured and the variation of the change in thickness is shown in Fig. 6.11 (a) and (b). Except for one position where the change in the thickness is negative, the thickness of the copper tube got increased. It can be concluded from this observation that the thickening of the tube will happen due to the EMP crimping process.

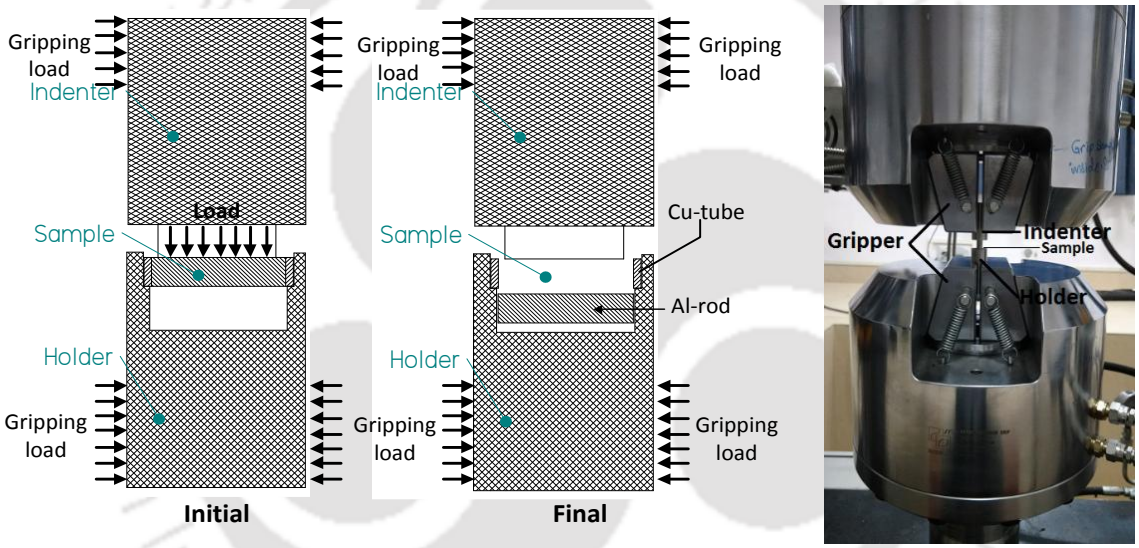

(a) (b)

Fig. 6.8 (a) Initial and final stages and (b) arrangement for compression-shear test on UTM

6.2.3 Effect of discharge energy on joint strength

The discharge energies used were 3.3 kJ, 4.0 kJ, 4.6 kJ, 5.3 kJ and 6.2 kJ for assessing the effect of discharge energy on joint strength with a standoff 0.27 mm and feeding length 14 mm. The joint strength of the crimped samples is examined by pull-out tests. In the pull-out test, it was found that crimped samples failed with separation failure mode. In separation failure mode, the two parts crimped together were separated. The pull-out load variation with the elongation for three types of field shaper tapered, step-tapered and stepped are shown in Fig. 6.12 (a), (b), and (c).

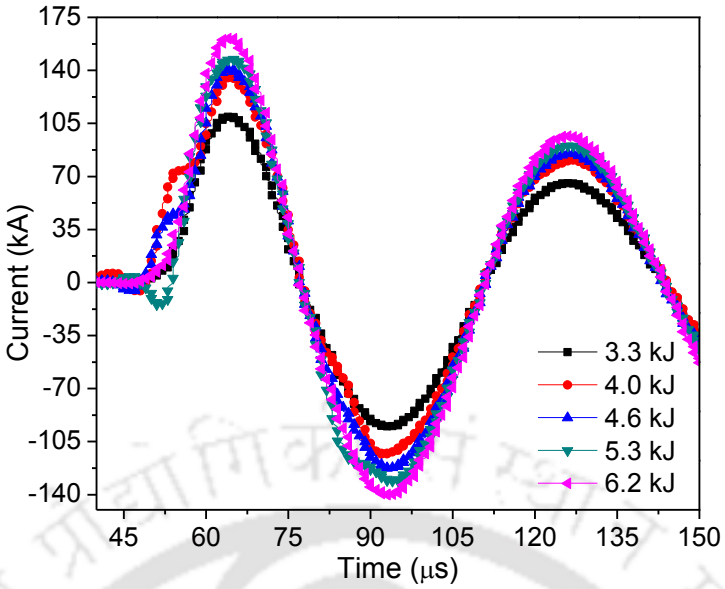

Fig. 6.9 Discharge current waveform at different energies

Table 6.4 Process parameters in the experiments

S No	Voltage (kV)	Energy (kJ)	Discharge current amplitude (kA)	Time-period (μs)	Frequency (kHz)
1.	8.6	3.3	109.3	60.4	16.56
2.	9.4	4.0	135.5	60.4	16.56
3.	10.2	4.6	140.9	60.2	16.61
4.	10.9	5.3	147.3	60.2	16.61
5.	11.7	6.2	161.0	60.0	16.67

From Fig. 6.12 (a), (b) and (c), it can be concluded that with the increase in discharge energy joint strength also increases. The variation in the maximum pull-out load with the discharge energy for three types of field shaper is shown in Fig. 6.12 (d). It was found that the strength of the joint obtained with step-tapered field shaper was better in comparison to that of stepped and which was better than that of tapered field shaper. The reason for the increase of the joint strength in case of step-tapered field shaper was due to better confinement of the magnetic field near the effective length.

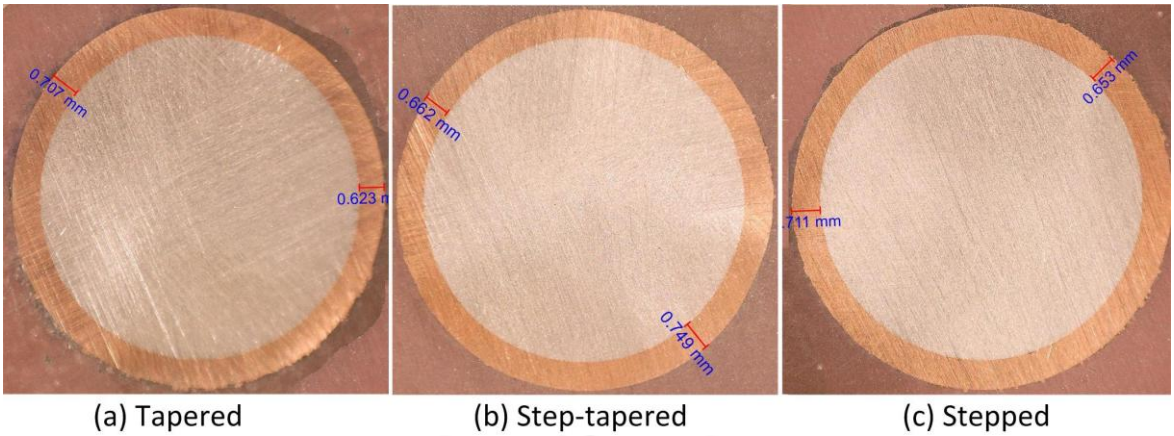

Fig. 6.10 Maximum and minimum thickness of the flyer copper tube for different field shapers

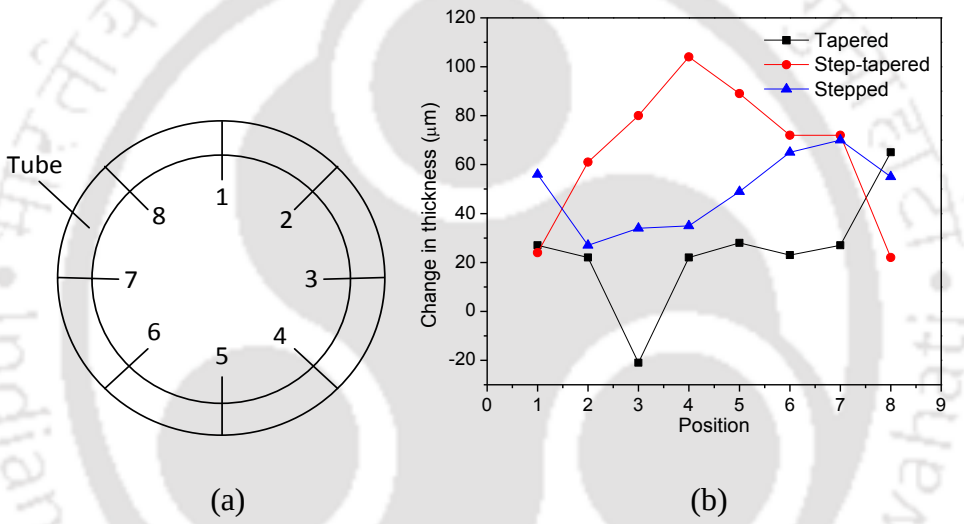

Fig. 6.11 (a) Position of thickness measurement, and (b) change in the thickness of the tube at different position

Successfully crimped samples prepared at five different discharge energies were tested for a compression-shear test. The variation in the joint strength at five different discharge energies with three types of field shapers namely tapered, step-tapered and stepped are shown in Fig. 6.13 (a), (b) and (c). From Fig. 6.13 (a), (b) and (c), it can be concluded that with the increase in discharge energy joint strength also increases. The variation in the maximum compressive joint strength with the discharge energy for three types of field shaper is shown in Fig. 6.13 (d). Compression-shear tests result revealed that the compressive joint strength obtained with step-tapered field shaper was maximum among the three field shapers.

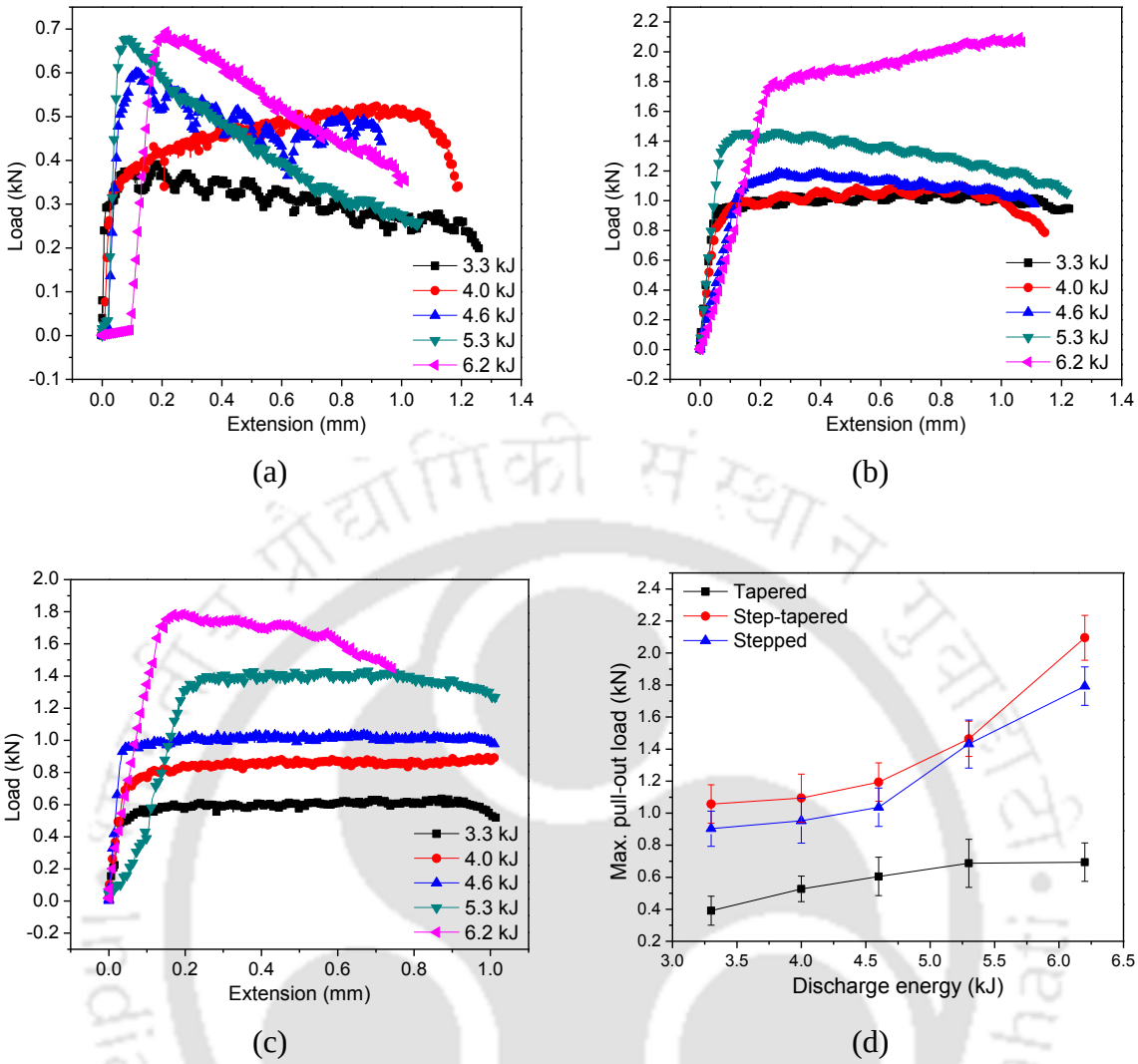

Fig. 6.12 Pull-out test results for (a) tapered, (b) step-tapered and (c) stepped field shaper at different energy, and (d) variation in maximum pull-out load with energy

6.2.4 Effect of field shaper geometry on joint strength

The comparison of pull-out test and compression-shear test results revealed that joint strength obtained by step-tapered field shaper was better than that of stepped and tapered field shaper. Also, the joint strength obtained with the stepped field shaper was better than that of tapered field shaper. The compared pull-out test results of the three field shapers at 3.3 kJ, 4.6 kJ, and 6.2 kJ is shown in Fig. 6.14. The required maximum pull-out load for tapered, step-tapered and stepped field shaper was 0.694 kN, 2.095 kN, and 1.793 kN respectively at 6.2 kJ of discharge energy.

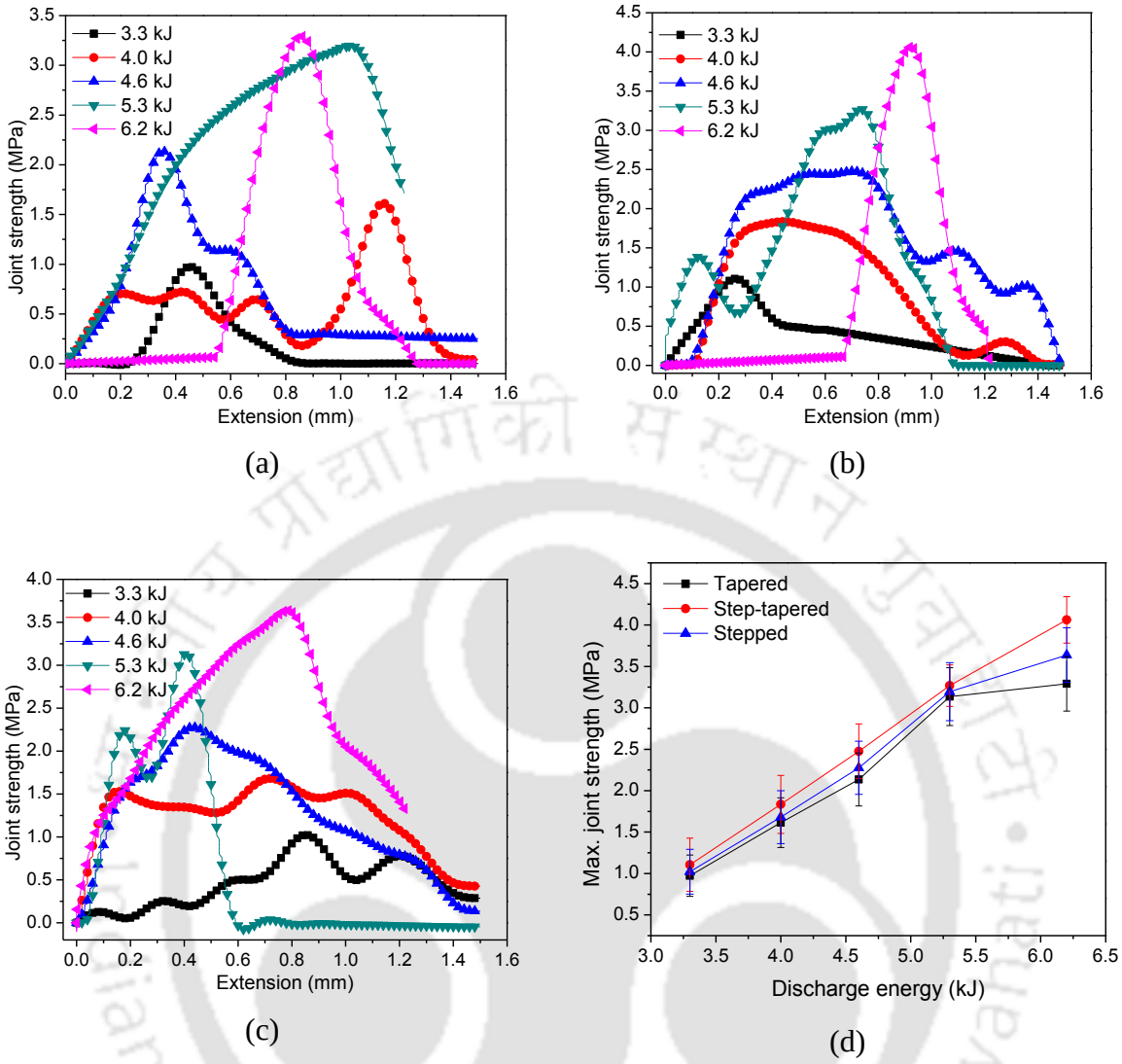

Fig. 6.13 Compression-shear test results for (a) tapered, (b) step-tapered and (c) stepped field shaper at different energy, and (d) variation in maximum joint strength with energy

The compared compression-shear test results of the three field shapers at 3.3 kJ, 4.6 kJ, and 6.2 kJ is shown in Fig. 6.15. The maximum compressive shear strength of the joint produced with tapered, step-tapered and stepped field shaper was 3.29 MPa, 4.062 MPa, and 3.64 MPa respectively at 6.2 kJ of discharge energy.

The step-tapered field shaper results in higher join strength, both in pull-out tests as well as a compression-shear test due to the lower mass volume of the field shaper compared to other two field shaper. Here, higher energy will be concentrated in the effective area of the field shaper which has lower mass volume for the same effective area of the field shaper and discharge energy. In the step-tapered field shaper case as the mass volume for the field shaper

is lower, hence higher force was produced due to lower electromagnetic inductance loss and consequently better joint strength was obtained.

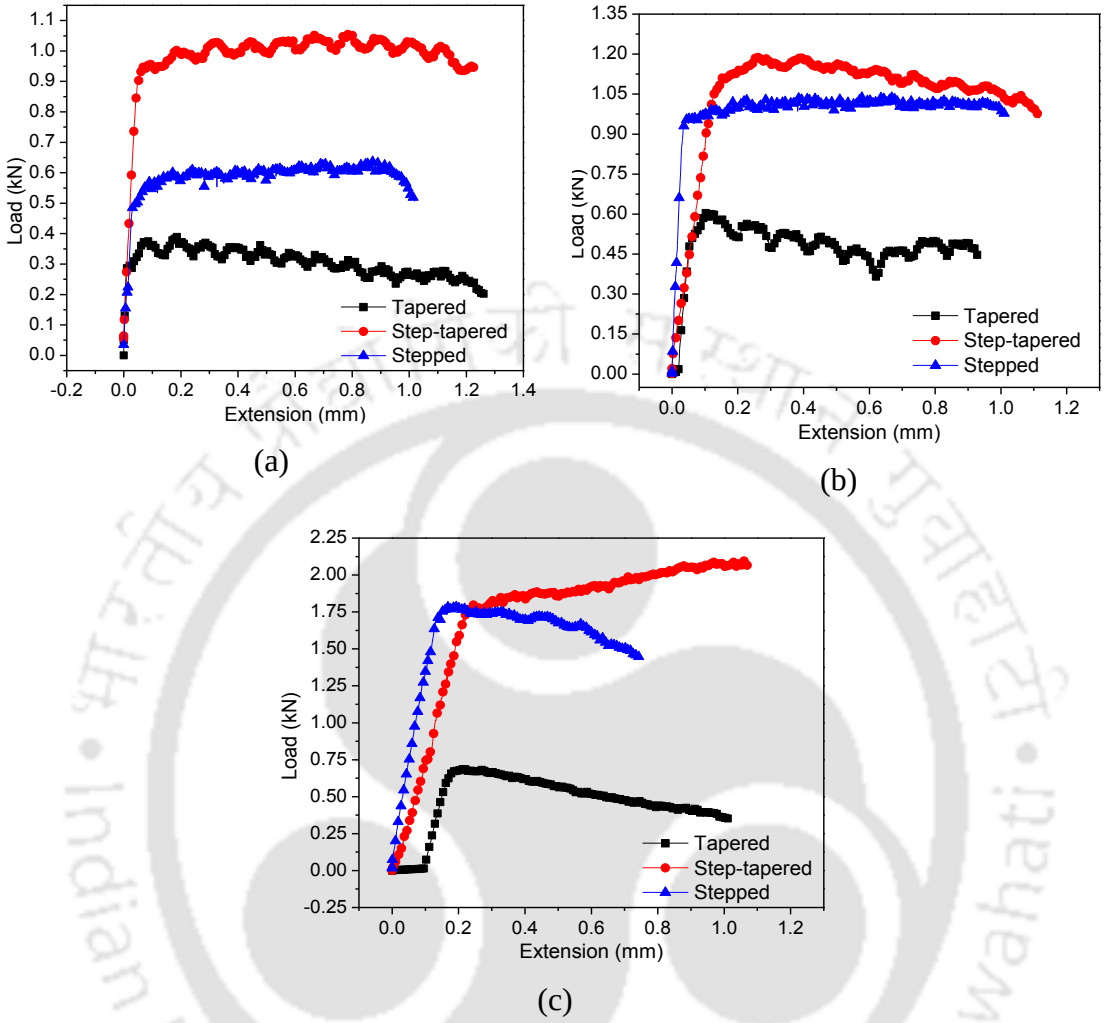

Fig. 6.14 Pull-out test results comparison at (a) 3.3 kJ, (b) 4.6 kJ and (c) 6.2 kJ discharge energies

6.2.5 Effect of field shaper geometry on joint electrical resistance

The electrical resistance of the EMP crimped samples was measured by using LCR meter. The complete set-up with input alternating current (AC) used to measure the electrical resistance is shown in Fig. 6.16. When two terminals of the LCR meter were connected to the two ends of the crimped sample and current (*I*) was passed through the circuit and electrical resistance was measured. A wire was used to complete the circuit and the electrical resistance of the wire was subtracted from the measured value. The variation in the electrical resistance of the crimped samples with the discharge energy for three types of field shaper is shown in Fig. 6.17. The results of the electrical resistance measurement revealed that with the increase in the discharge

energy the electrical resistance or joint electrical resistance decreases. The value of the electrical resistance obtained by the step-tapered field shaper was lesser in comparison to the other two field shapers. The reason for the lesser joint electrical resistance was due to better contact of the tube with the rod.

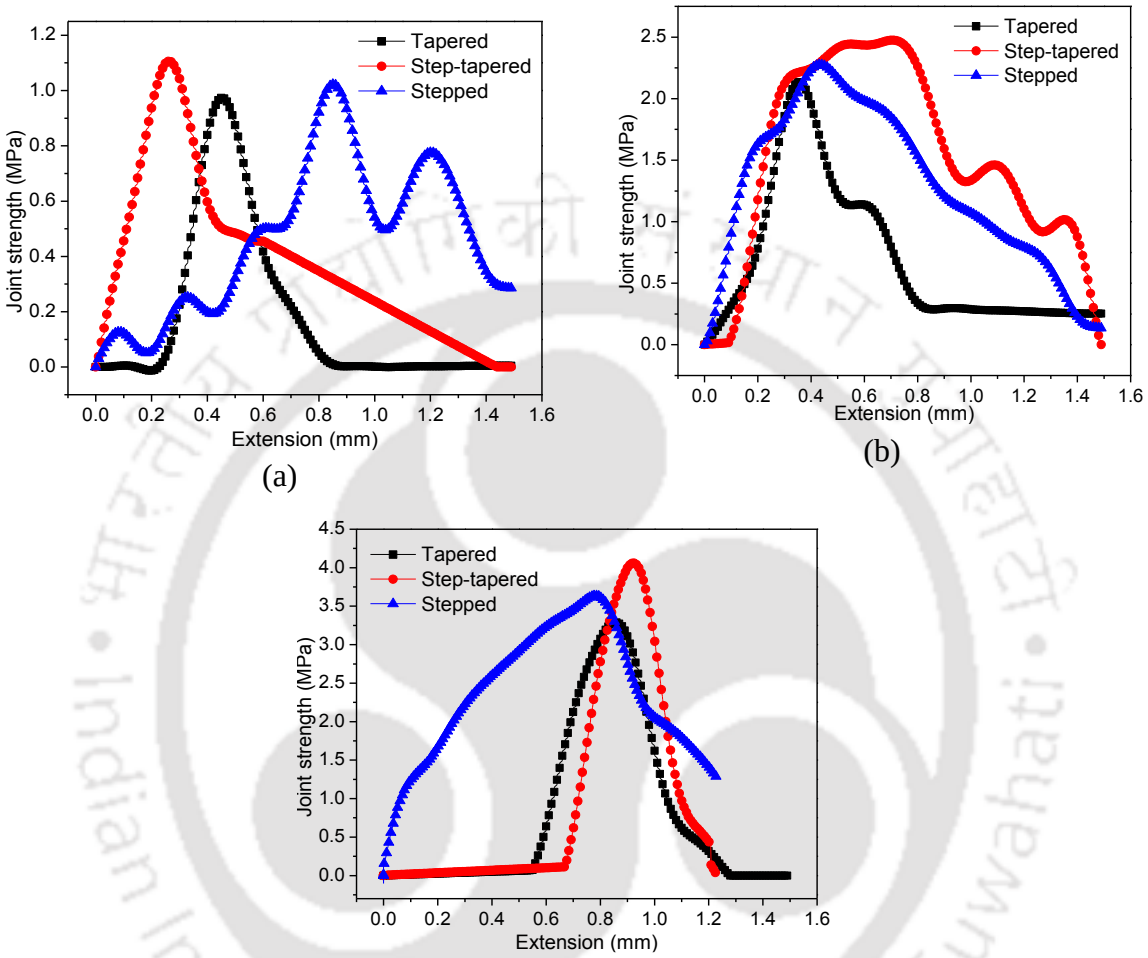

Fig. 6.15 Compression-shear test results comparison at (a) 3.3 kJ, (b) 4.6 kJ and (c) 6.2 kJ discharge energies

The step-tapered field shaper results in lesser joint electrical resistance due to a lower mass volume of the field shaper leading to low inductance compared to other two field shaper. In the step-tapered field shaper case as the mass volume for the field shaper is lower. Therefore, it resulted in lower electromagnetic loss and consequently better connection and lower electrical resistance.

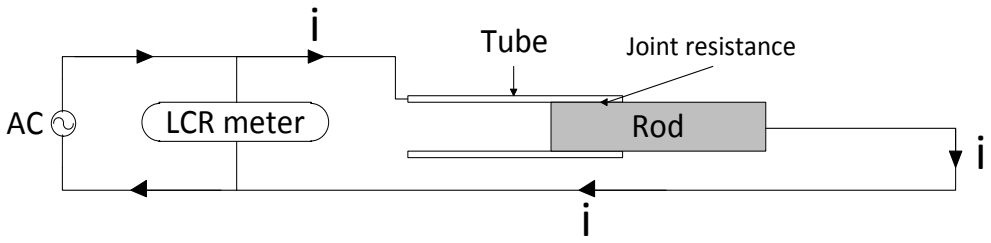

Fig. 6.16 Joint electrical resistance measurement set-up

6.2.6 Effect of shaper geometry on joint leakage

Leak test was performed on the crimped samples with compressed air. The complete arrangement made to perform the leak test is shown in Fig. 6.18. The arrangement comprised of an air-compressor with mounted pressure gauge, water tube, and connecting pipe. Compressed air was allowed to pass through the connecting pipe to the sample to has to test. An air bubble was produced in the water because of the leakage of the joint. The successfully crimped samples at 6.2 kJ with three type of field shapers were tested on the air-bubble leak test. The leak rate was measured by dividing the pressure drop with the time duration which was 3600 s. For the samples crimped with tapered, step-tapered and stepped field shaper the leak rate was found to be 3.33×10^{-4} bar s^{-1}, 2.22×10^{-4} bar s^{-1} and 2.78×10^{-4} bar s^{-1} respectively at 10 bar pressure of the air compressor. Hence, it can be concluded that the strength of the joint obtained by step-tapered field shaper was better than that of stepped and tapered.

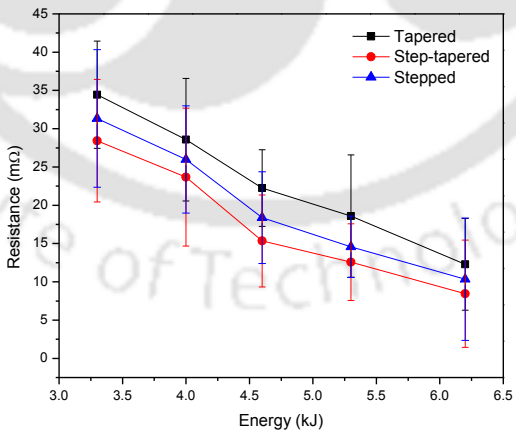

Fig. 6.17 Variation in electrical resistance with the discharge energy

6.2.7 Effect of shaper geometry on surface finish

The surface finish of the crimped samples with three field shapers was studied by using high precision contactless computerized surface profilometer. The maximum area that can be captured with the help of contactless three-dimensional profilometer was 0.825 mm × 0.825 mm. The focal length of the profilometer was 4.7 mm. The surface finish of the samples crimped at 6.2 kJ of discharge energy with three types of field shaper was analyzed. The R_a values were measured at three locations, and the average R_a values were listed in Table 6.5.

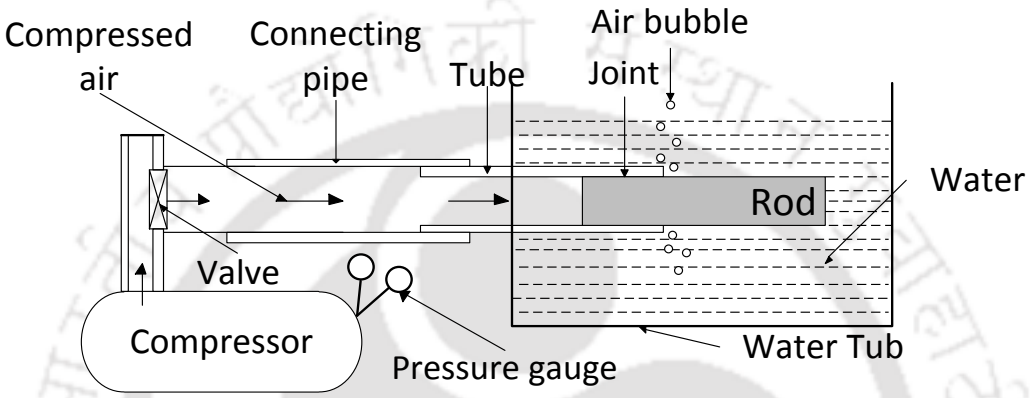

Fig. 6.18 Compressed air leak test arrangement

Table 6.5 Surface finish of crimped samples with three field shapers at 6.2 kJ

	Tapered				**Step-tapered**				**Stepped**			
	1	**2**	**3**	**Avg.**	**1**	**2**	**3**	**Avg.**	**1**	**2**	**3**	**Avg.**
R_a (µm)	0.47	0.49	0.54	0.50	0.38	0.44	0.41	0.41	0.40	0.44	0.48	0.44

The surface finish results revealed that the surface finish value of the crimped samples with step-tapered field shaper was better or R_a value was lesser than that of the tapered and stepped field shapers. Three-dimensional fringe patterns of the surface finish with varying R_a values for all three types of the field shaper at 6.2 kJ of the discharge energy are shown in Fig. 6.19.

The summary of the different tests at 6.2 kJ of the discharge energy with three field shapers is shown in Table 6.6.

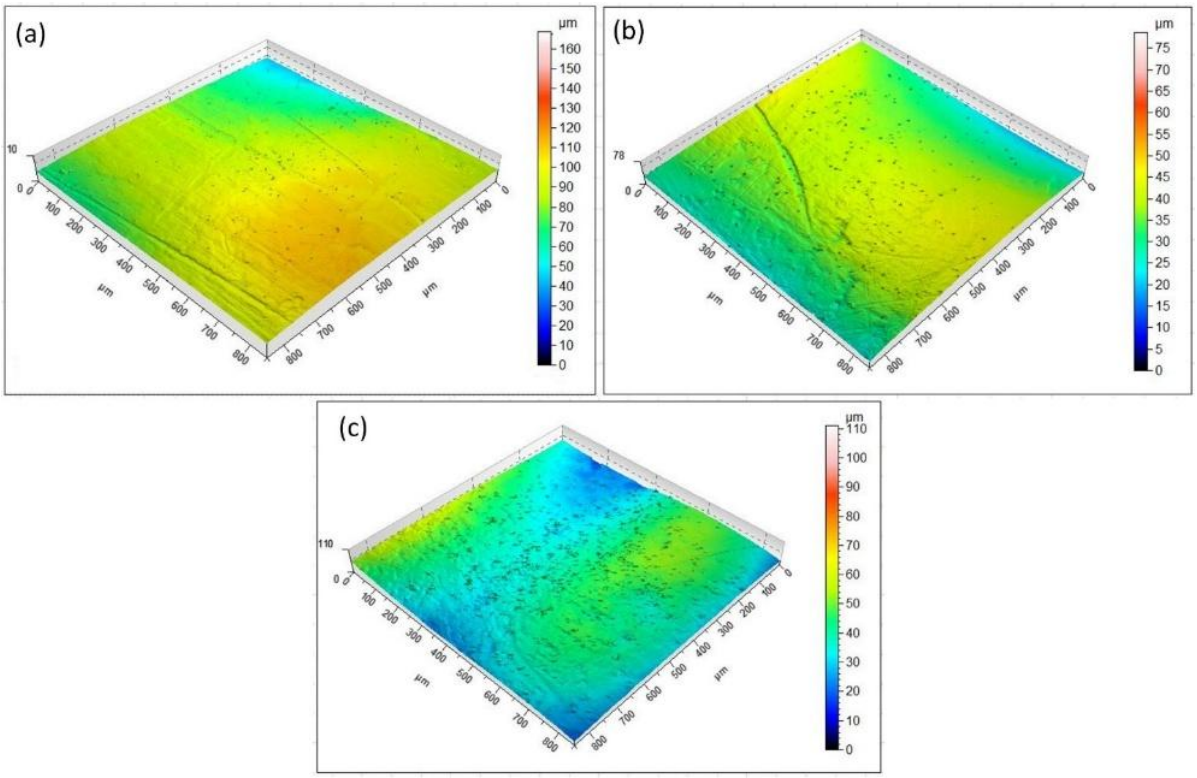

Fig. 6.19 3D surface profile with (a) tapered, (b) step-tapered, and (c) stepped field shaper at 6.2 kJ

Table 6.6 Summary of the outputs of different tests at 6.2 kJ

Field shaper type	**Max. Pull-out strength (kN)**	**Max. Compressive shear strength (MPa)**	**Leak rate (bar s^{-1})**	**Electrical joint resistance (mΩ)**	**Surface finish (R_a, in μm)**
Tapered	0.694	3.29	3.33×10^{-4}	12.29	0.50
Step-tapered	2.095	4.062	2.22×10^{-4}	8.45	0.41
Stepped	1.793	3.64	2.78×10^{-4}	10.34	0.44

6.3 Summary

EMC method was used to produce Copper-Aluminum crimp rods or composite rods. This technique has special characteristics that it produces a uniform distribution of the copper tube on the circumference of the aluminum rod with a complete circular cross-sectional area. The increase in the amount of discharge energy from the capacitor bank will increase the strength

of the joint. The results of the pull-out test and the compression-shear test revealed that the joint strength obtained with the step-tapered field shaper was better than that of stepped field shaper which was better than the tapered field shaper. The required maximum pull-out load for tapered, step-tapered and stepped field shaper was 0.694 kN, 2.095 kN, and 1.793 kN respectively at 6.2 kJ of discharge energy. The joint electrical resistance of the crimped samples decreases with the increase in the discharge energies of the process. Joints minimum electrical resistance, joint leakage proof and surface finish of the crimped samples with three types of field shaper at 6.2 kJ of discharge energy were analyzed. The results showed that the samples produced with the step-tapered field shaper was better in favor among the tapered, step-tapered and stepped field shapers. Copper crimped aluminum rod can be used in electrical applications wherever aluminum rod was used for better electrical conductivity and minimum loss due to resistance.

7 Study of the Temperature Generation with Various Field Shaper Geometries

OVERVIEW

The prime objectives of this investigation are to studying the variation in the geometry of the field shaper to concentrate the electromagnetic pressure at the desired location to produce an effective joint with better mechanical strength. Finite element analysis as well as experimental study was carried out on three types of field shaper namely tapered, taper-stepped and stepped. In all three field shapers the effective length, outer diameter, inner diameter, total length, materials properties were constant. These field shapers were kept inside the same multi-turn solenoid coil for all the experiments. It was found that the taper-stepped field shaper results better in terms of impact velocity, Lorentz force, temperature generation, less heating, uniformity in crimping among the three types of field shaper. The effectiveness of the taper-stepped field shaper was found to be higher compare to stepped field shaper than that of tapered field shaper. The proposed explanations regarding the joint formation is mechanical joining and the joint formation takes place based on pressure because of high strain rates and plastic deformation of the flyer causes a solid state crimped joint. Joule heating will also takes place in all the parts such as coil, field shaper, flyer tube, and the base rod. The numerical study was carried out by using LS-DYNA electromagnetism (EM) module which includes the electromagnetic/thermal /mechanical/structural coupled solver. This module helps in linking the source electrical current into the conductors as well as develops an interface between mechanical and electromagnetic solver.

7.1 Experimentation

7.1.1 Machine and materials

A circular cross-section copper wire was used to manufacture the multi-turn solenoid coil. The diameter of the circular cross-section was 5 mm. The pitch of the coil used was 8.0 mm and the number of turns on the solenoid coil was 11. The materials of the coil and field shaper used

was copper-beryllium alloy. The materials properties of the copper and the aluminum used for tube and rod is given in Table 7.1.

The dimensions of the tube and the rod used for the experiment is listed in the Table 7.2. The copper tube used was of 0.64 mm thickness. The standoff used was of 0.27 mm in the entire experiment. In the experiments helical solenoid coil having 11 number of turns and of 8.0 mm pitch was used. Three types of field shapers were used namely tapered, taper-stepped and stepped. The actual image along with the three dimension model of the three types of the field shapers used is shown in Fig. 7.1. The actual image along with the three dimension model of the three types of the field shapers used is shown in Fig. 7.2.

7.1.2 Finite element modelling

The Maxwell's equations are the governing equation for the electromagnetic field. The Maxwell's equations in the simplified version can be expressed by equations (7.1) to (7.4). In Maxwell's equations, equation (7.1) summarises the effects of matter plus Coulomb's law of forces. The equation (7.2) represents an extension of Ampere's circuital law, the equation (7.3) proclaims Faraday's law of induction and equation (7.4) represents the non-existence of magnetic monopoles.

$$\nabla \cdot \vec{\mathrm{D}} = \rho \tag{7.1}$$

$$\nabla \times \vec{H} = \vec{J} + \frac{\partial \vec{D}}{\partial t} \tag{7.2}$$

$$\nabla \times \vec{E} = -\frac{\partial \vec{\mathrm{B}}}{\partial \mathrm{t}} \tag{7.3}$$

$$\nabla \cdot \vec{B} = 0 \tag{7.4}$$

where the vector functions $\vec{E}$, $\vec{D}$, $\vec{B}$, and $\vec{H}$ are known as

$\vec{E}$: Electric field (V/m)

$\vec{D}$: Electric displacement field (coulomb/m^2)

$\vec{B}$: Magnetic induction (Tesla)

$\vec{H}$: Magnetic field (A/m)

Some sources generate the electromagnetic field and those sources are

$\vec{J}$: Electric current density (A/m^2)

ρ : Electric charge density (C/m^3)

The electric current density and the electric charge density are related through the continuity equation which is given by equation (7.5).

$$\nabla \cdot \vec{J} = -\frac{\partial \rho}{\partial t} \tag{7.5}$$

The EMC is a high strain-rate process and hence Johnson Cook equation was used for the finite element study. The Johnson Cook equation has a special characteristics that it includes the strain rate hardening effect in the flow stress for high strain rates. The mathematical form of the Johnson Cook equation is given by the equation (7.6).

$$\sigma_y = (A + B\varepsilon^n)\left(1 + C\ ln\ \dot{\varepsilon_p}\right)\left(1 - \left(\frac{T - T_r}{T_m - T_r}\right)^m\right) \tag{7.6}$$

Table 7.1 Material properties of Cu 1010 and Al 1050

Properties	**Units**	**Cu 1010**	**Al 1050**
Density (ρ)	Kg/m^3	8940	2705
Modulus of elasticity (E)	GPa	54	69
Poisson's ratio (ν)	-	0.31	0.33
Electrical conductivity (σ)	MS/m	59	37.67
Heat capacity (C)	J/Kg-K	3.94	921
Thermal conductivity (k)	W/m-K	391	231

In equation (7.6), σ_y is flow stress of the material, A, B are the yield strength parameters, ε is equivalent plastic strain, n is the strain hardening index, C is the strain rate sensitivity, $\dot{\varepsilon_p}$ is plastic strain rate, T is absolute temperature, T_r is the room temperature, T_m is the melting temperature of the material and m is the thermal softening index. These parameters have different values for different materials and can be determined experimentally for each materials. The Johnson Cook parameters used in the study are tabulated in Table 7.3.

Table 7.2 Dimensions and materials of the tube and rod

Specimen	Materials	Outer diameter	Inner diameter	Length	Thickness	Stand-off
Flyer tube	Copper	9.52 mm	8.24 mm	60 mm	0.64 mm	-
Base rod	Al 1050	7.70 mm	-	60 mm	-	0.27 mm

In a shock compressed solid analysis, pressure has to be determined. Therefore, an equation of state is required to define the relation between volume and pressure in the Johnson Cook equation. In this study, linear polynomial equation of state given by equation (7.7) was used [66].

$$P = c_o + c_1\mu + c_2\mu^2 + c_3\mu^3 + E_o\,(c_4 + c_5\mu + c_6\mu^2) \tag{7.7}$$

In equation (7.7), P is pressure, $c_o, c_1, \ldots, c_6$ are the constant parameters of linear polynomial equation of state, E_o is the internal energy, and $\mu = \frac{\rho}{\rho_o} - 1$ is compression factor where $\frac{\rho}{\rho_o}$ is the ratio of density of medium and initial density of medium. The constant coefficients of linear polynomial equation of state for copper and aluminum are presented in Table 7.4 [66].

In the simulations, after computing electromagnetic fields by electromagnetic solver at each node the Lorentz force was evaluated and added to the mechanical solver. In the LS-DYNA thermal solver, the electromagnetic fields also added a Joule heating term which is given by equation (7.8).

Table 7.3 Values of Johnson-Cook material constant parameters

Materials	*A (MPa)*	*B (MPa)*	*n*	*C*	T_m *(K)*	*m*
Copper [67]	92	292	0.31	0.025	1338	1.09
Al 1050 [61]	110	150	0.4	0.01	918	1

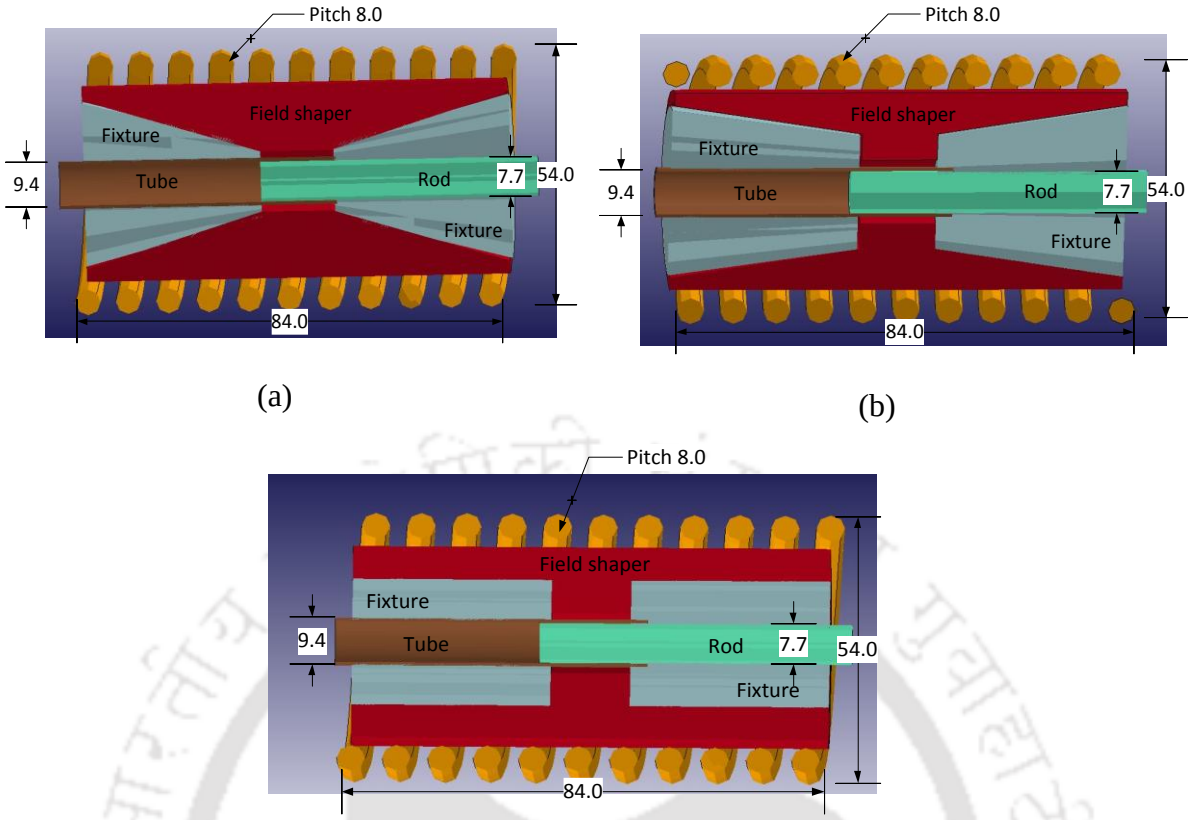

Fig. 7.1 Dimensions of the complete assembly with the (a) tapered, (b) taper-stepped, and (c) stepped field shaper

$$Q = \gamma J^2 \tag{7.8}$$

where Q is the heat generated per unit volume (in W/m^3), J is the current density (in A/m^2), and γ is the specific electrical resistivity (in Ω m). The deformation in the tube was obtained by mechanical model which results in new geometry. The temperature generation in the tube was due to tube deformation by high velocity impact and Joule heating. In the simulated model, mainly two thermal properties were used namely thermal conductivity (k) and the heat capacity (c).

Table 7.4 Values of linear polynomial equation of state

Materials	c_o	c_1	c_2	c_3	c_4	c_5	c_6	E_o	V_o
Copper [68]	0	140	2.8	1.96	0.47	0	0	0	1
Aluminum [69]	0	74.2	60.5	36.5	1.96	0	0	0	1

The input load in the simulation was the discharge current curve, which was measured from the experiment with the help of Rogowski current coil and oscilloscope. The change in the

electrical conductivity of the flyer, coil, field-shaper and the base materials was assumed to be constant in the simulation because it leads to increase in the simulation time as well as the complexity of the problem.

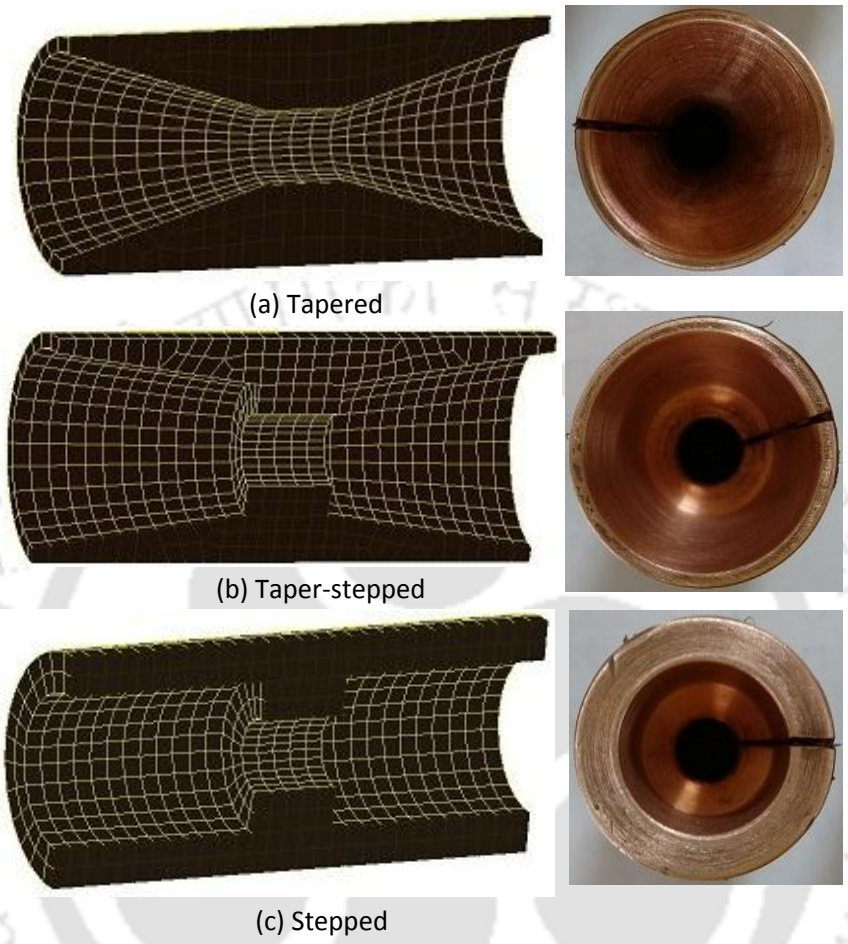

Fig. 7.2 Three types of field shaper used (a) tapered, (b) taper-stepped, and (c) stepped

7.2 Results and Discussion

7.2.1 Discharge current measurement

The discharge current in the EMC process curve is typically a damped sinusoidal waveform. The discharge current in the experiment, passing through the multi-turn solenoid coil was measured by a Rogowski coil and oscilloscope. The waveform of the discharge current at five different values of discharge energy is shown in Fig. 7.3. The values of the discharge energies used were 4.5 kJ, 5.1 kJ, 5.8 kJ, 6.5 kJ and 7.2 kJ for these energies the peak values of the discharge current were 124 kA, 136.4 kA, 148.8 kA, 161.2 kA and 173.6 kA respectively. The measured discharge current was used as input load in the EMC. Only the first peak of the

discharge current was responsible for high-velocity impact of the flyer tube. The high-velocity impact in the flyer tube results in the deformation and joining with the base rod.

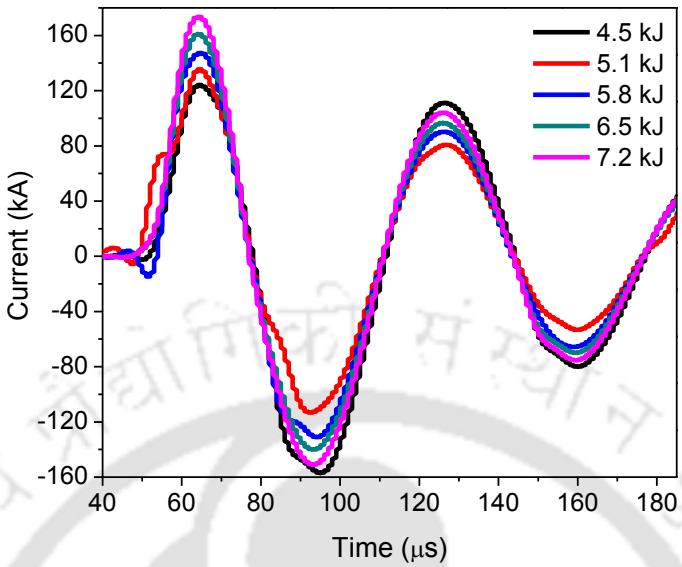

Fig. 7.3 Measured discharge current waveform at five different energies

The discharge current curve which is typically a damped sinusoidal curve can be well expressed by the mathematical relation given by equation (3).

$$I(t) = \frac{V_o}{\omega L} e^{-\beta\tau} \sin(\omega\tau) \tag{7.9}$$

where V_0 is the initial discharge voltage, L is the equivalent inductance of the system, ω is the angular frequency, and β is the damping exponent [70].

The samples crimped by the EMC process are shown in Fig. 7.4. Five different values of the discharge currents were used in the experiments with the three types of the field shapers. The cross-section of the crimped samples were analyzed and compared with the simulated results.

7.2.2 Temperature measurement

The temperature generated in the working zone was studied and the same was also simulated to compare the performance of the three field shapers. The thermographic image of the arrangment of the working zone with three different field shapers is shown in Fig. 7.5. The temperature generated in the working zone in the experiment with three types of field shaper was measured by using infrared thermometer. The infrared thermometer works on the principle that each body with a temperature above the absolute zero emits electromagnetic radiation from its surface, which is proportional to its intrinsic temperature or infrared radiation. At four

different locations P1, P2, P3, and P4, on the tube the current was measured. The temperature was also calculated at four different elements H72357, H72447, H71997, and H72376 in the simulated model. The locations where the temperature was measured in the experiments and in the simulation is depicted in Fig. 7.5. These locations were selected due to visibility while measuring the temperature by the infrared thermometer.

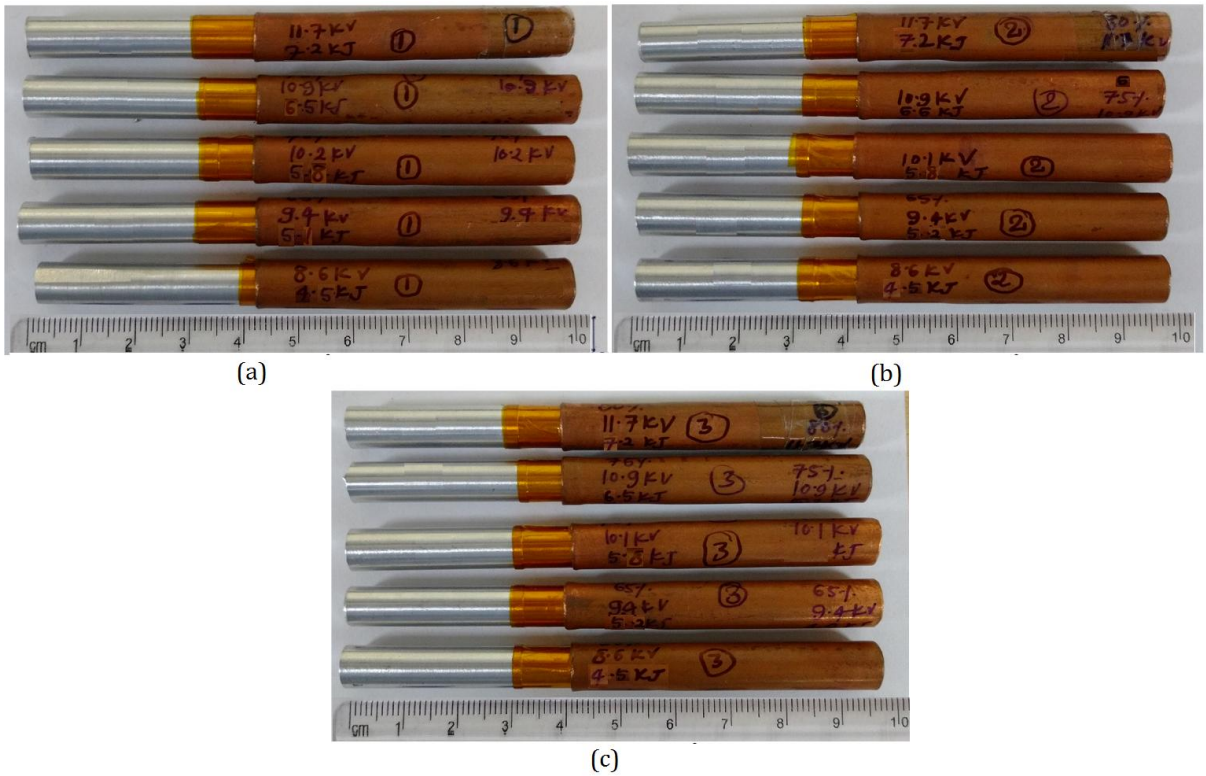

Fig. 7.4 Sample produced by (a) tapered, (b) taper-stepped, and (c) stepped field shapers

The values of the temperature measured at four different locations, both in the experiment as well as in the simulation was plotted. The variation in temperature with discharge energy (a) experimental and (b) simulated results is shown in Fig. 7.6 with tapered, taper-stepped and stepped field shapers.

The temperature changes in the coil and the field shaper was also studied. However, the changes in temperatures in the field shaper as well as in the coil were minimal, and that was below 5 ℃. The temperature generated in the tube with the taper-stepped field shaper is 2.9 % more than stepped and 4.5 % than tapered field shaper. Hence, the detailed study was not reported for this range of the discharge energy. The fringe pattern of the temperature (in K) generated in the tube with three types of field shapers is shown in Fig. 7.7.

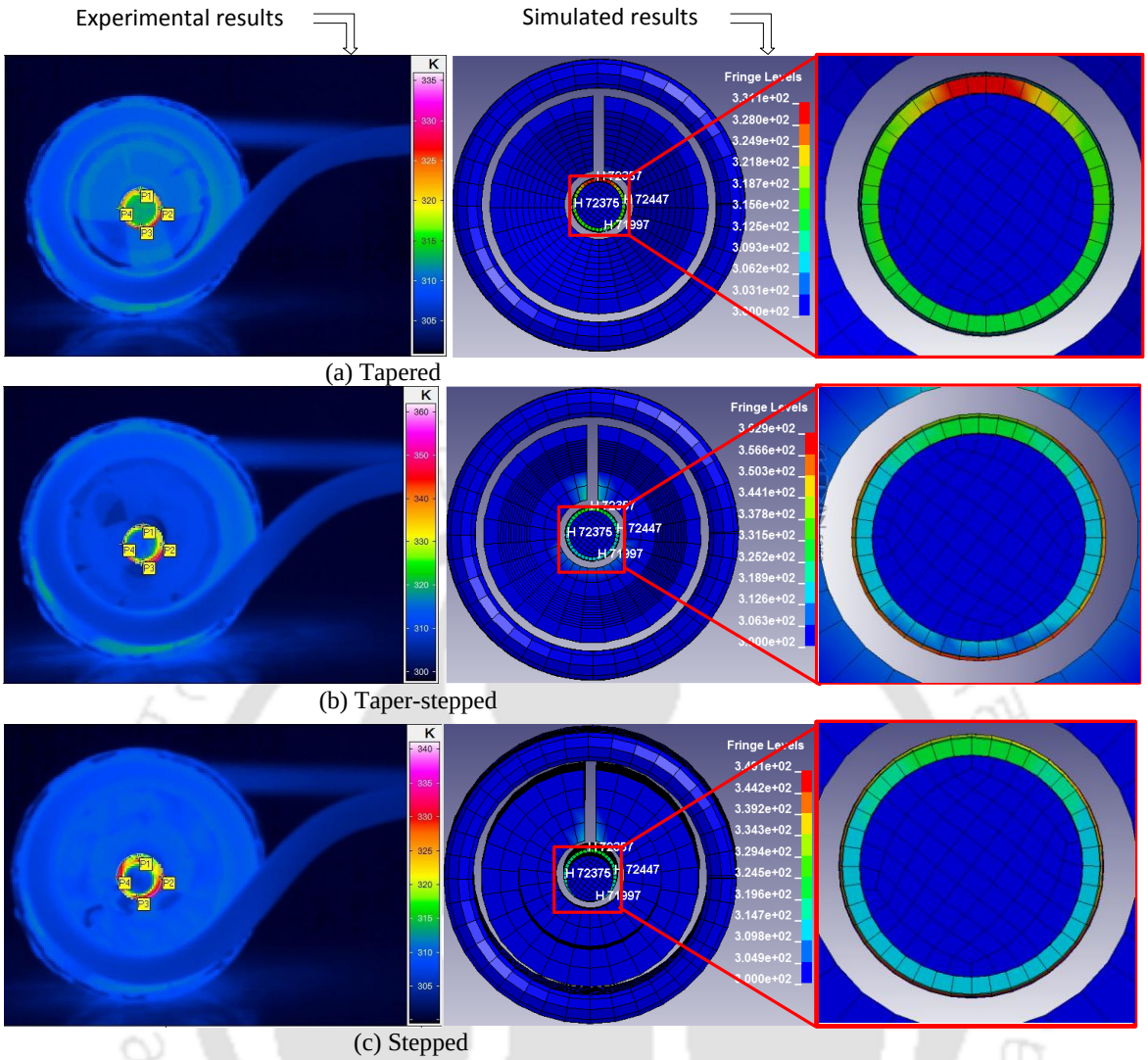

Fig. 7.5 Thermography view of the working zone with (a) tapered, (b) taper-stepped, and (c) stepped field shaper

The comparative plot of simulated values of the maximum temperature with the peak value of the discharge current is shown in Fig. 7.6(b). It was found that the maximum temperature generated in the simulation was more than that of the experimental values. This variation can be due to leakage of the current and losses in the experiment. The maximum variation in the values of the simulated one was found to be 5.4 %.

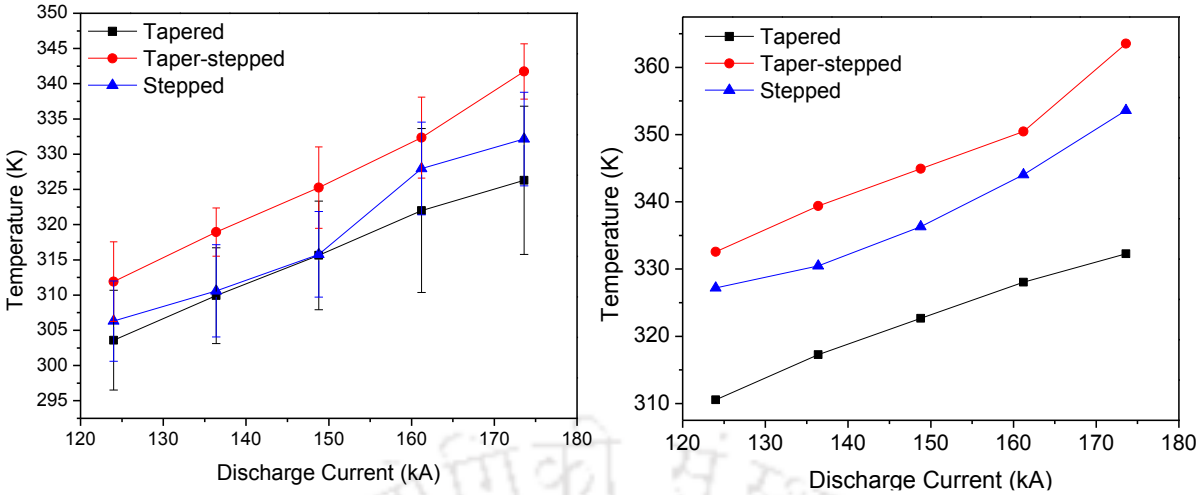

(a) (b)

Fig. 7.6 Temperature (in K) variation with discharge current (in kA) (a) in experiments, and (b) in simulations

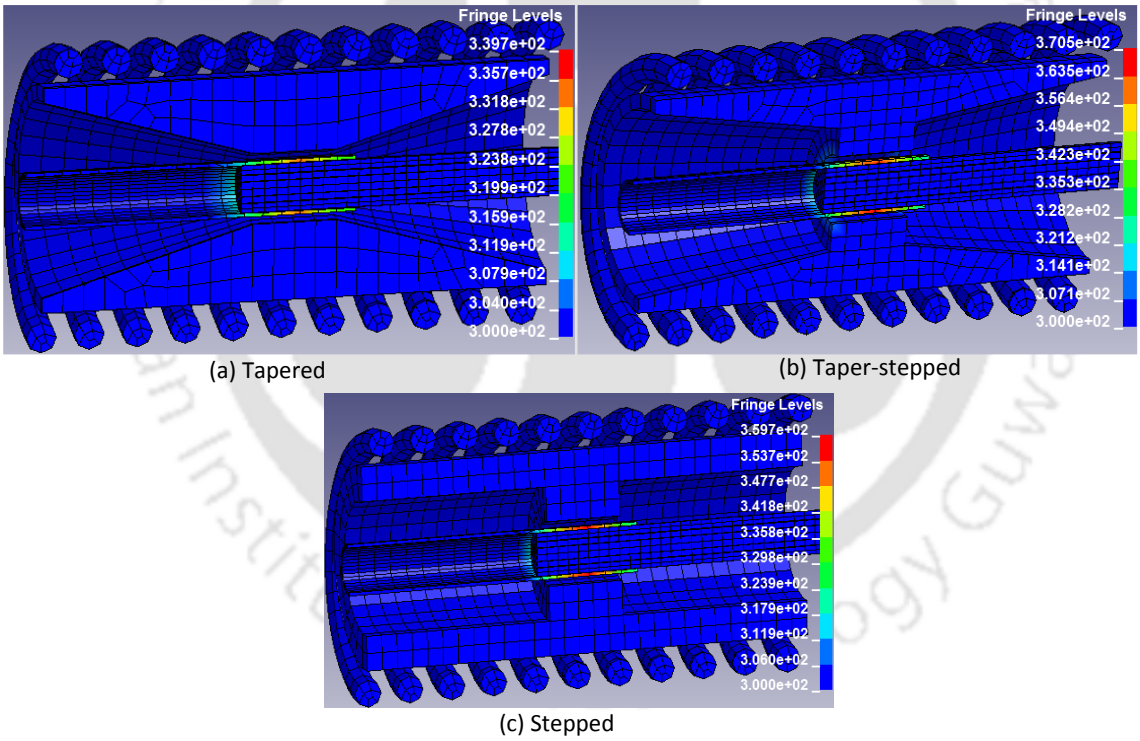

Fig. 7.7 Fringe pattern of the temperature developed with (a) tapered, (b) taper-stepped, and (c) stepped field shaper at 7.2 kJ of discharge energy

The outer diameter of the crimped sample obtained at 6.2 kJ was measured by using digital microscope. The outer diameter of the model obtained from the simulation at the same energy was also measured. The outer diameter of the crimped sample obtained from the experiment simulations was compared with that obtained from the simulations. There was a variation found

in the values obtained from the experimental and simulations and it was around 1.9 %, 2.0 % and 1.8 % respectively for tapered, taper-stepped and stepped field shaper.

The outer diameter of the measured crimped sample, in experiment and from simulations is shown in Fig. 7.8. In the Fig. 7.8, D represents the outer diameter, C is the circumference, and S is the area of the circle. The difference in the outer diameter, from the simulations and that obtained from the experiment was due to coarse mesh of the elements in the simulation. Coarse mesh causes relatively more gap at the interface, due to large element size and hence increase the outer diameter. The element size used in this work was sufficient for the objectives obtained in this work, and hence no finer mesh or mesh refinement was done. Fine mesh leads to higher simulation time as well as complexity in the convergence of the solutions.

The variation in the outer diameter of the crimped sample with the discharge energy from the experiment is shown in Fig. 7.9(a). The variation in the outer diameter of the simulated model with the discharge energy is shown in Fig. 7.9(b).

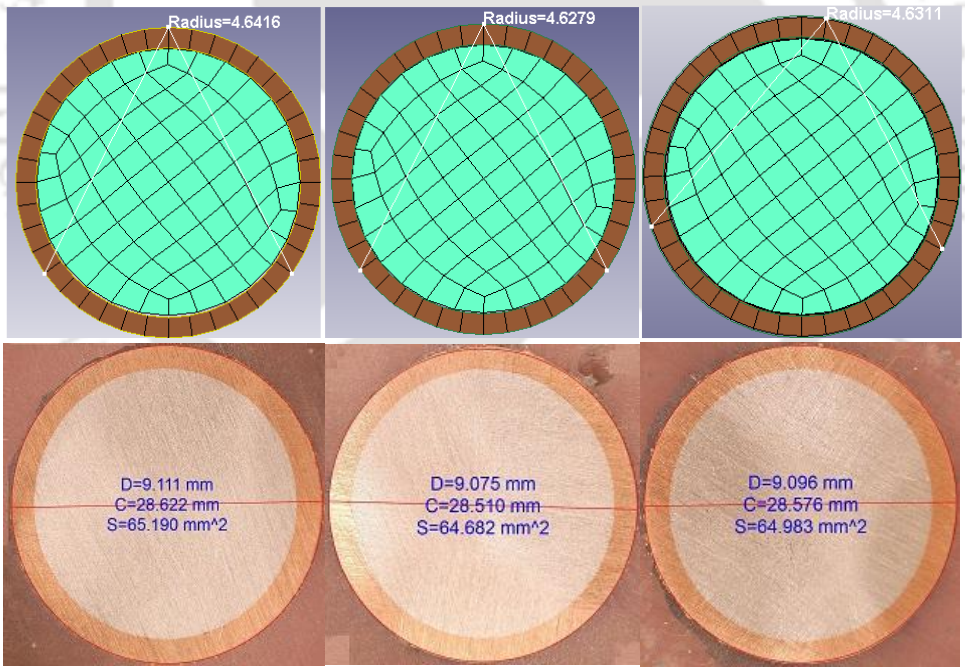

(a) Tapered (b) Taper-stepped (c) Stepped

Fig. 7.8 Outer diameter of the sample (top simulation, bottom experiment) with three types of the field-shaper at 6.2 kJ of the discharge energy

The magnetic field, plastic strain and impact velocity of the tube were also studied in the simulated model. The variation in the magnetic field, plastic strain, and impact velocity with the discharge current for three types of field shapers is shown in Fig. 7.10.

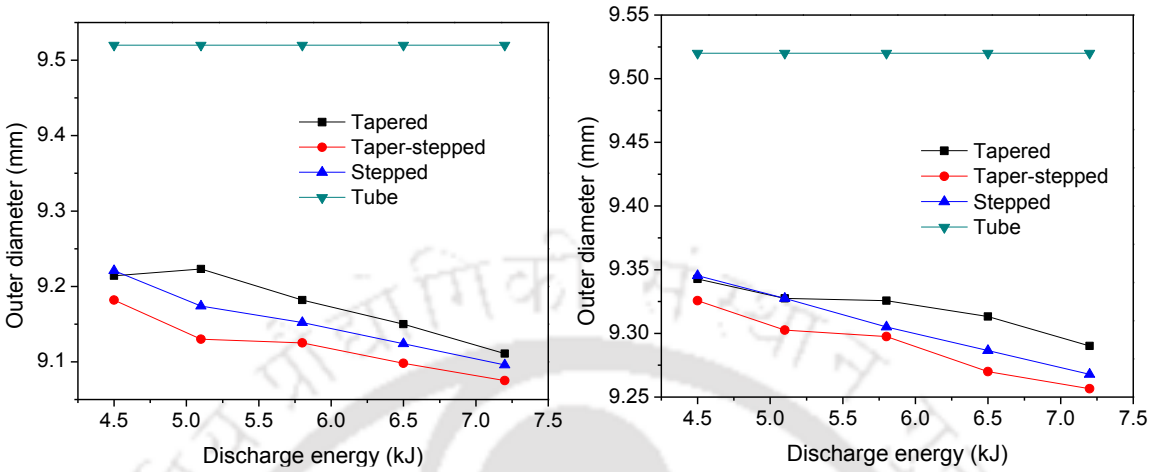

Fig. 7.9 Variation in the outer diameter of the crimped sample with the discharge energy for three types of field shaper (a) experimental values, and (b) simulations values

7.2.3 Distribution of the Lorentz force, magnetic field and current density

The validated finite element model based on the temperature variation and the outer diameter obtained, was used for comparative study of the field-shapers. In the comparative study, the results compared were the Lorentz force, the magnetic field and the current density developed in the tube. The results of the maximum value of the Lorentz force, the magnetic field and the current density plot revealed that the effectiveness of the taper-stepped field-shaper was higher compared to that of the other two field-shaper, tapered and stepped. The vector plot of the Lorentz force developed on the flyer tube with the three types of field-shaper is shown in Fig. 7.11. The maximum values of the Lorentz force on the flyer tube with the three field shapers namely tapered, step-tapered and stepped were 550 N, 1093 N and 790.2 N respectively, at 7.2 kJ of discharge energy.

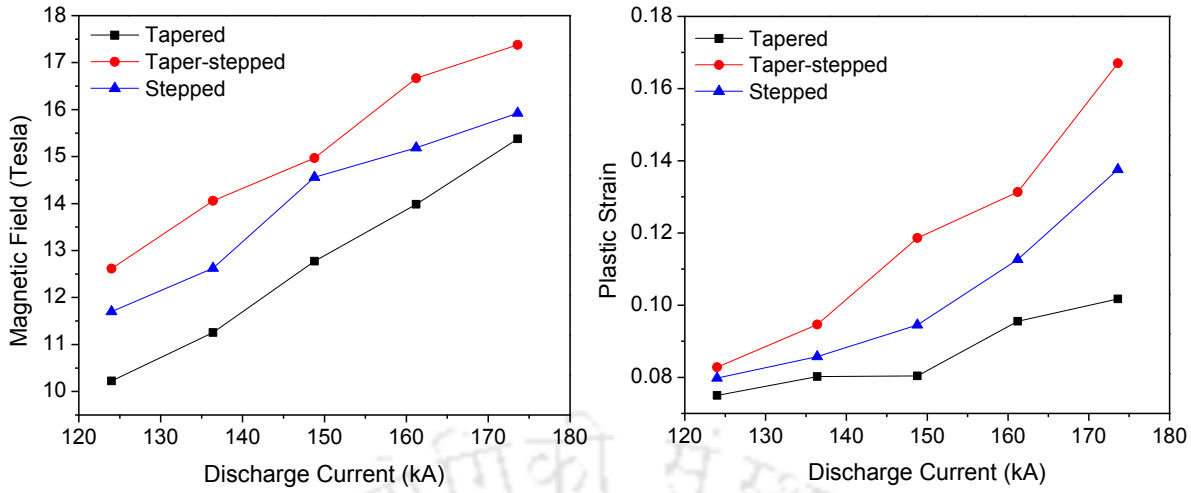

(a) (b)

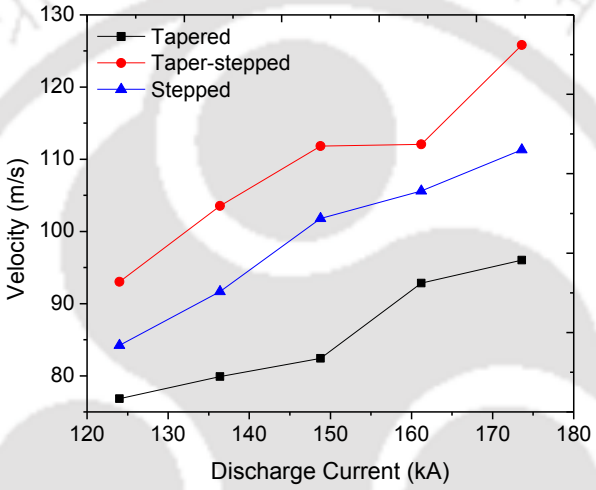

(c)

Fig. 7.10 Variation in the (a) magnetic field (in Tesla), (b) plastic strain, and (c) velocity (in m/s) with discharge current (in kA)

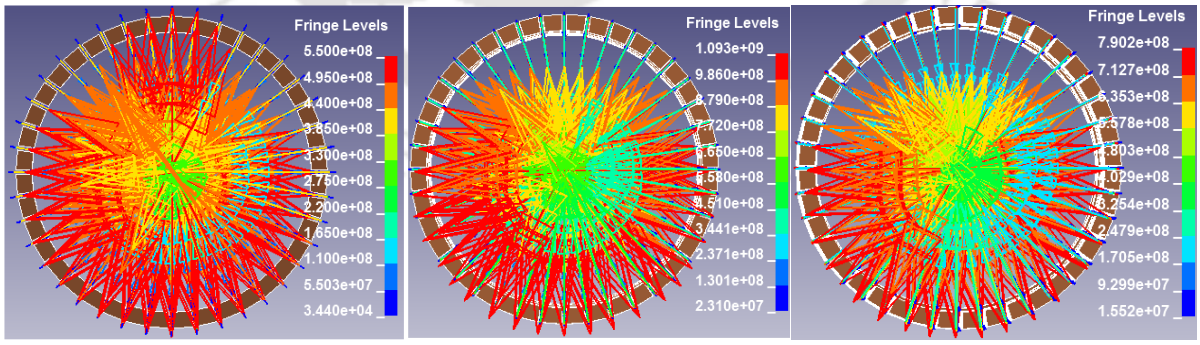

(a) Tapered (b) Taper-stepped (c) Stepped

Fig. 7.11 Vector pattern of the Lorentz force developed on the flyer with (a) tapered, (b) taper-stepped, and (c) stepped field shaper at 7.2 kJ of discharge energy

The vector plot of the magnetic field generated on the flyer tube with the three types of field-shaper is shown in Fig. 7.12.

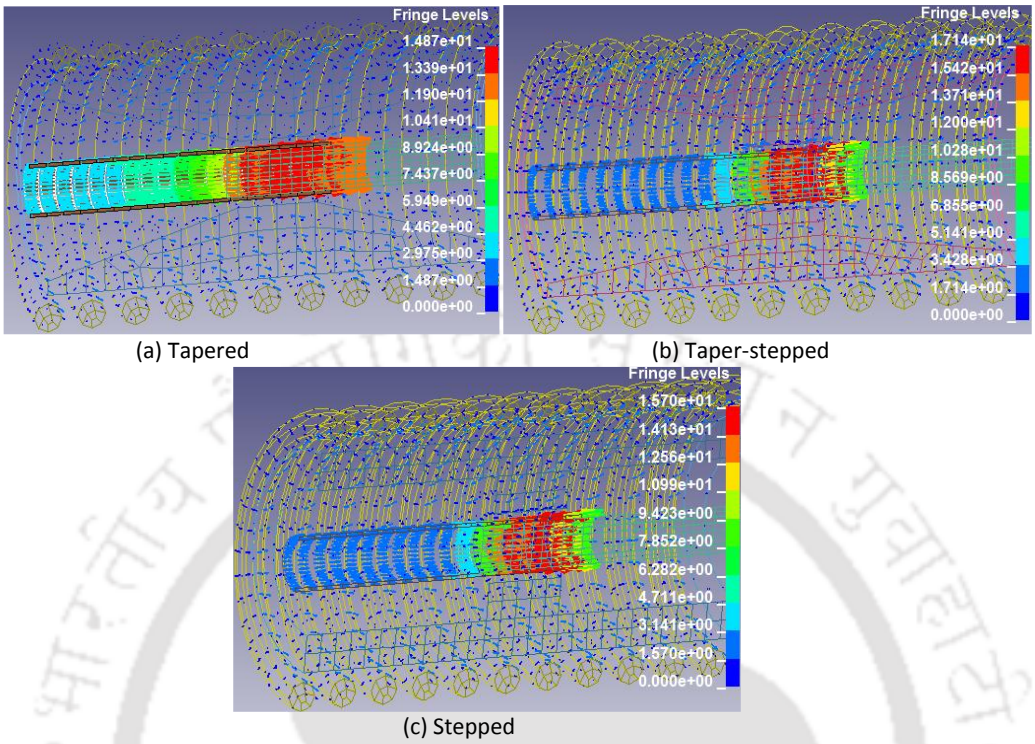

Fig. 7.12 Vector plot of the magnetic field developed on the flyer with (a) tapered, (b) taper-stepped, and (c) stepped field shaper at 7.2 kJ of discharge energy

The maximum values of the magnetic field on the flyer tube with the three field shapers namely tapered, step-tapered and stepped were 14.87 Tesla, 17.14 Tesla and 15.70 Tesla respectively, at 7.2 kJ of discharge energy. The concentration of the magnetic field in tube in case of taper-stepped and stepped field shapers were at the centre of the effective length while in the case of tapered field shaper the concentration of the magnetic field was at the end of the effective length of the field shaper.

The vector plot of the current density developed on the flyer tube with the three types of field-shaper is shown in Fig. 7.13. The maximum values of the current density on the flyer tube with the three field shapers namely tapered, step-tapered and stepped were 0.0345 A/m^2, 0.0639 A/m^2 and 0.0539 A/m^2 respectively, at 7.2 kJ of discharge energy.

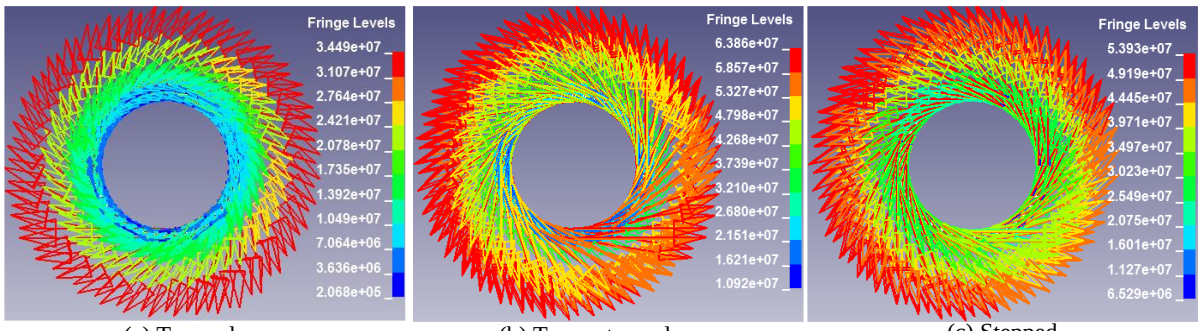

(a) Tapered (b) Taper-stepped (c) Stepped

Fig. 7.13 Vector plot of the current density developed on the flyer with (a) tapered, (b) taper-stepped, and (c) stepped field shaper at 7.2 kJ of discharge energy

From the vector plot of Lorentz force, magnetic field and current density with three types of field-shapers it can be concluded that the current density obtained with the taper-stepped field-shaper was higher compared to other two field-shapers. Hence, the geometry of the taper-stepped field-shaper was more efficient than that of the tapered and stepped field-shaper.

7.3 Summary

The EMC is a high speed and high strain rate metals joining technique. Numerical as well as experimental study was performed to produce the copper crimped aluminum rods. The specialty of this technique is that the crimped copper distributed uniformly over the circumference of the inner aluminum rod. For this study three types of field-shapers were used and their results were compared. The outer diameter of the copper crimped aluminum rod obtained from the experiment was compared with that obtained from the experiments, and maximum of variation 2.0 % was found. The temperature generated in the flyer copper tube as well as in the field shaper was measured and also simulated. The maximum values of the Lorentz force, magnetic field and current density with taper-stepped field shaper were 1093 N, 17.14 Tesla, and 0.0639 A/m^2 respectively. The results of outer diameter and temperature generated showed that the samples produced with the step-tapered field shaper were better in favor among the tapered, step-tapered and stepped field shapers. Copper crimped Al rod can be a replacement for electrical applications of aluminum rod having minimum electrical loss due to electrical resistance and higher electrical conductivity.

.----------*----------*----------.

भारतीय प्रौद्योगिकी संस्थान गुवाहाटी
Indian Institute of Technology Guwahati

8 Effect of Field Shaper Tapered Angle on the Electromagnetic Crimping Process

OVERVIEW

The objective of this study is to study the effect of the field shaper tapered angle on the performance of the field shaper i.e. on the impact velocity of the flyer tube, plastic strain in the tube and magnetic field generated on the tube. For this study the tapered angle of the tube used was 14.4°, 15.2°, 15.9°, 16.7°, and 17.4°. The other parameters related to the field shaper such as outer diameter, total length, inner diameter, and working length were kept constant. From this study, it was found that with the increase in the tapered angle of the field shaper, and maintaining the other parameters constant the impact velocity of the tube, magnetic field and plastic strain developed in the tube increase.

8.1 Materials and method

In this work, first of all the multi-turn solenoid coil was manufacture by using a circular cross-section copper wire. The diameter of the wire was 5 mm, the pitch of the coil was 8.0 mm, and the number of turns was 11 for the solenoid coil. To increase the performance and life of the coil stepped field shaper was also used in this work. The material of the field shaper as well as the coil were copper-beryllium alloy. The mechanical properties of the materials used for the field shaper and for the coil are tabulated in Table 8.1. The dimensions of the samples used for the crimping are tabulated in the Table 8.2. The field shapers used have constant outer diameter of 38 mm, inner diameter of 12 mm, total length of 84 mm, working length of 14 mm. The configuration of the field shaper along with the details dimensions is shown in Fig. 8.1 and the actual images of the filed shaper used in the experiment is shown in Fig. 8.2.

8.1.1 Physics of the process

In the numerical model, Maxwell's equations were used for the electromagnetic field. The Maxwell's equations can be expressed by equations (8.1) to (8.4). In Maxwell's equations, equation (8.1) summarises the effects of Coulomb's law of forces. The equation (8.2)

represents an extension of Ampere's circuital law, the equation (8.3) represents the Faraday's law of electromagnetic induction and equation (8.4) shows the non-existence of magnetic monopoles.

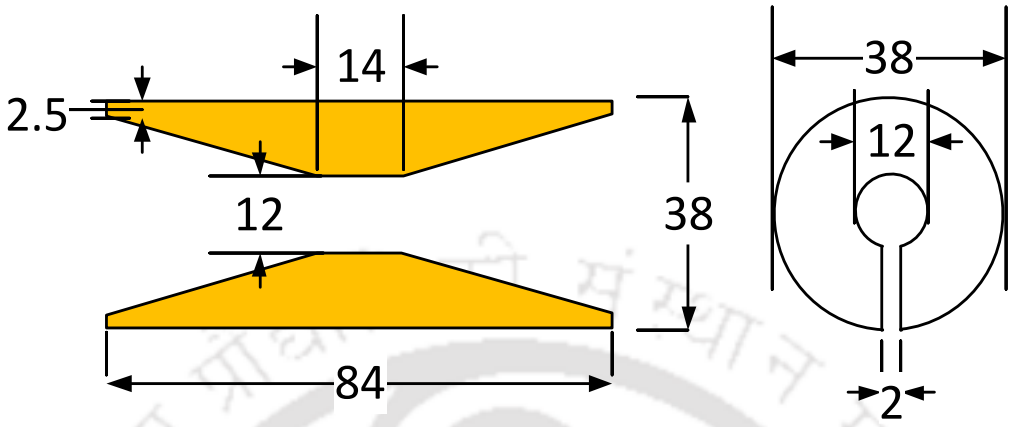

Fig. 8.1 Dimensions of the field shaper (all dimensions are in mm)

Table 8.1 Mechanical properties of tube (Cu 1010) and rod (Al 1050)

Properties	**Units**	**Cu 1010**	**Al 1050**
Modulus of elasticity (E)	GPa	54	69
Poisson's ratio (ν)	-	0.31	0.33
Heat capacity (C)	J/Kg-K	3.94	921
Electrical conductivity (σ)	MS/m	59	37.67
Thermal conductivity (k)	W/m-K	391	231
Density (ρ)	Kg/m^3	8940	2705

Table 8.2 Dimensions and materials of the flyer tube and rod

Specimen	**Materials**	**Outer diameter**	**Inner diameter**	**Length**	**Thickness**	**Stand-off**
Flyer tube	Copper	9.52 mm	8.24 mm	60 mm	0.64 mm	-
Base rod	Al 1050	7.70 mm	-	60 mm	-	0.27 mm

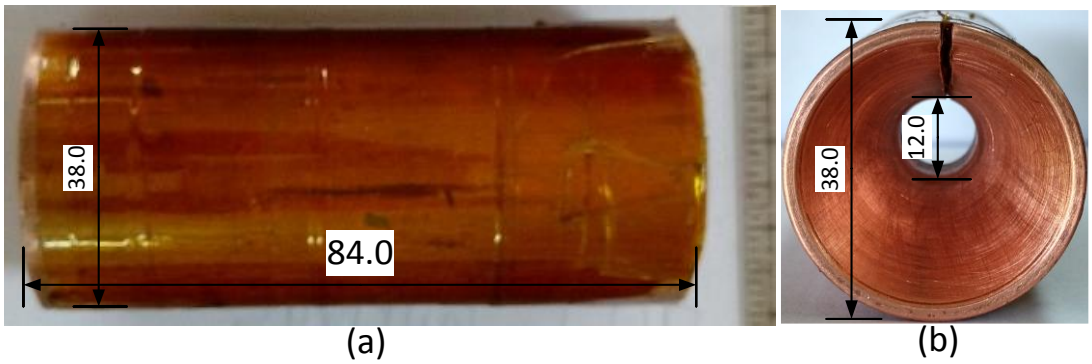

Fig. 8.2 Actual image (a) top view and (b) front view of the tapered field shaper (all dimensions are in mm)

$$\nabla \cdot \vec{D} = \rho \tag{8.1}$$

$$\nabla \times \vec{H} = \vec{J} + \frac{\partial \vec{D}}{\partial t} \tag{8.2}$$

$$\nabla \times \vec{E} = -\frac{\partial \vec{B}}{\partial t} \tag{8.3}$$

$$\nabla \cdot \vec{B} = 0 \tag{8.4}$$

In the above equations vector functions $\vec{E}$, $\vec{D}$, $\vec{B}$, and $\vec{H}$ are known as Electric field (V/m), Electric displacement field (coulomb/m^2), Magnetic induction (Tesla) and Magnetic field (A/m) respectively. Electric current density ($\vec{J}$, A/m^2) and electric charge density (ρ, C/m^3) are the sources which generate the electromagnetic field. These sources are related through the continuity equation which is given by equation (8.5).

$$\nabla \cdot \vec{J} = -\frac{\partial \rho}{\partial t} \tag{8.5}$$

8.1.2 Johnson Cook materials model

In the EMC process, the magnitude of the strain-rate is high, therefore Johnson Cook equation can be used for analysis of the process which incorporate the high strain. The Johnson Cook equation has a special characteristics that it includes the strain rate hardening effect in the flow stress for high strain rates. The mathematical form of Johnson Cook model can be represented by the equation (8.6).

$$\sigma_y = (A + B\varepsilon^n)\left(1 + C\, ln\, \dot{\varepsilon_p}\right)\left(1 - \left(\frac{T - T_r}{T_m - T_r}\right)^m\right) \tag{8.6}$$

In equation (8.6), σ_y represents materials flow stress, A, B are the parameters related to the yield strength of the material, ε is equivalent plastic strain, n is the strain hardening index, C is the strain rate sensitivity, $\dot{\varepsilon_p}$ represents plastic strain rate, T is absolute temperature, T_r is the room temperature, T_m represents the materials melting temperature and m represents the thermal softening index. These parameters have different values for different materials and can be determined experimentally for each materials. For this study, the values of the Johnson Cook equation are given by Table 8.3.

8.1.3 Linear polynomial equation of state

In a shock compressed solid analysis, pressure has to be determined. Therefore, an equation of state is required to define the relationship between volume and pressure in the Johnson Cook equation. In this study, the linear polynomial equation of state given by equation (8.7) was used [66].

$$P = c_o + c_1\mu + c_2\mu^2 + c_3\mu^3 + E_o\,(c_4 + c_5\mu + c_6\mu^2) \tag{8.7}$$

In equation (8.7), P is pressure, $c_o, c_1, \ldots, c_6$ are the constant parameters of the linear polynomial equation of state, E_o is the internal energy, and $\mu = \frac{\rho}{\rho_o} - 1$ is compression factor where $\frac{\rho}{\rho_o}$ is the ratio of the density of medium and initial density of the medium. The constant coefficients of the linear polynomial equation of state for copper and aluminum are presented in Table 8.4 [66]. In the simulations, after computing electromagnetic fields by electromagnetic solver at each and every node in the model the Lorentz force was calculated and added to the mechanical solver. In the LS-DYNA thermal solver model, the electromagnetic fields also included a Joule heating term for thermal study which is given by equation (8.8).

Table 8.3 Johnson Cook constant used in the simulation model

Materials	***A (MPa)***	***B (MPa)***	***n***	***C***	***T_m (K)***	***m***
Copper [67]	92	292	0.31	0.025	1338	1.09
Al 1050 [61]	110	150	0.4	0.01	918	1

$$Q = \gamma J^2 \tag{8.8}$$

where Q is the heat generated per unit volume (in W/m^3), J represents the current density (in A/m^2), and γ is the specific electrical resistivity (in Ω m). The deformation in the tube was obtained by a mechanical model which results in new geometry. The temperature generation in the tube was due to tube deformation by high-velocity impact and Joule heating. In the simulated model, mainly two thermal properties were used namely thermal conductivity (k) and the heat capacity (c).

Table 8.4 Values of linear polynomial equation of state

Materials	c_o	c_1	c_2	c_3	c_4	c_5	c_6	E_o	V_o
Copper [68]	0	140	2.8	1.96	0.47	0	0	0	1
Aluminum [69]	0	74.2	60.5	36.5	1.96	0	0	0	1

The input load in the simulation was the discharge current curve, which was measured from the experiment with the help of Rogowski current coil and oscilloscope. The change in the electrical conductivity of the flyer, coil, field-shaper and the base materials was assumed to be constant in the simulation because it leads to increase in the simulation time as well as the complexity of the problem. The parameter varied was the tapered angle of the field shaper. The five different tapered angles used were 14.4°, 15.2°, 15.9°, 16.7°, and 17.4°. Five different models of the field shaper were used in the study. The dimensions of the numerical model used in this study are shown in Fig. 8.3.

8.2 Results and Discussions

8.2.1 Discharge current measurement

The discharge current in the electromagnetic crimping process curve is typically a damped sinusoidal waveform. Digital oscilloscope and Rogowski coil were used to measured the discharge current in the experiment, passing through the multi-turn solenoid coil. The damped sinusoidal curve of the discharge current at five different values of discharge energy is shown in Fig. 8.4. The values of the discharge energies varied are 4.5 kJ, 5.1 kJ, 5.8 kJ, 6.5 kJ and 7.2 kJ for these energies the peak values of the discharge current were 124 kA, 136.4 kA, 148.8 kA, 161.2 kA, and 173.6 kA respectively. The measured discharge current was used as the input load in the electromagnetic crimping process. In this joining process, only the first half cycle of the discharge was was responsible to obtain the maximum impact velocity in the flyer

tube. The impact of the flyer tube onto the rod with high-velocity causes platic deformation of the flyer tube, and results in the formation of joint with the copper rod.

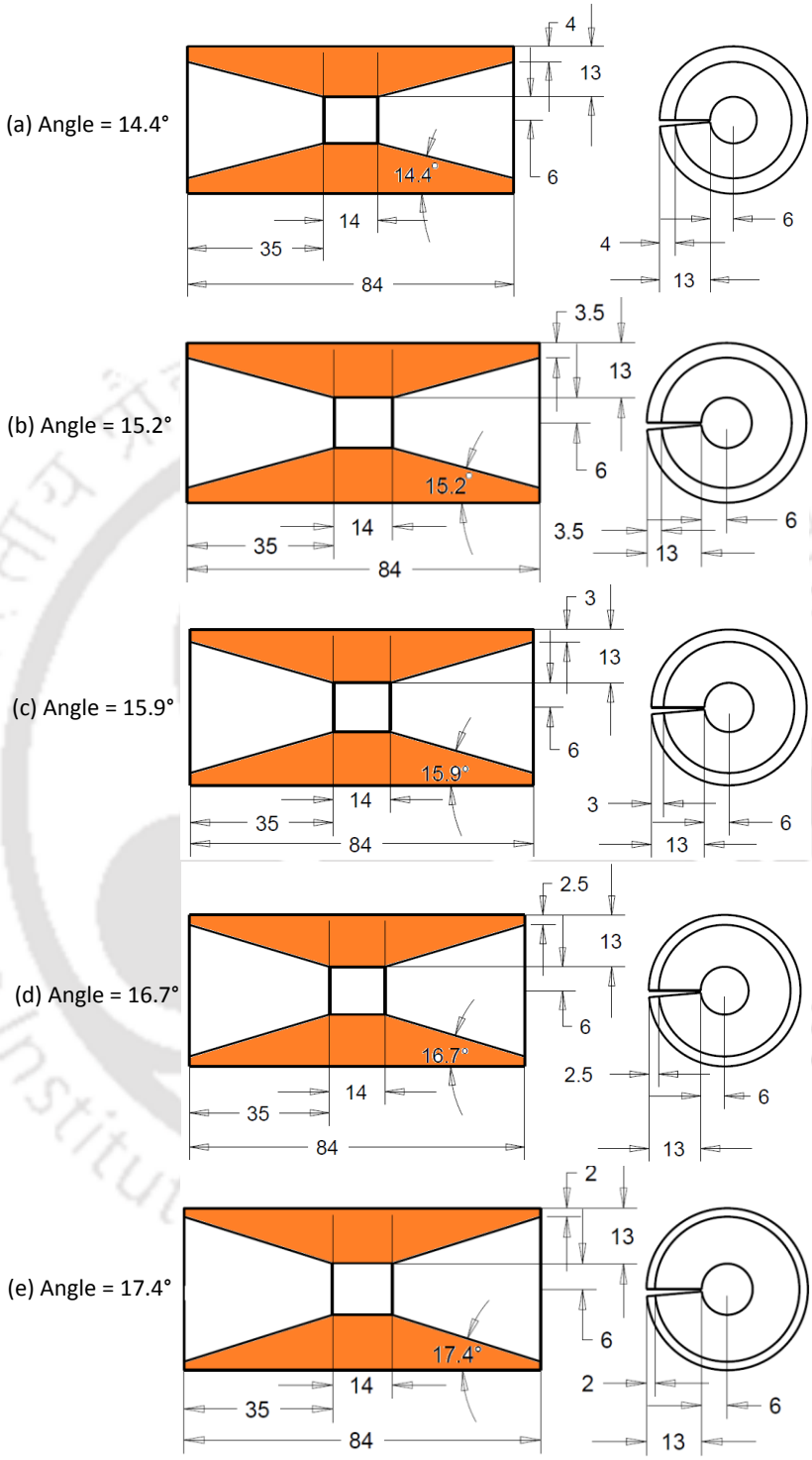

Fig. 8.3 Five different types of field shaper used in the study

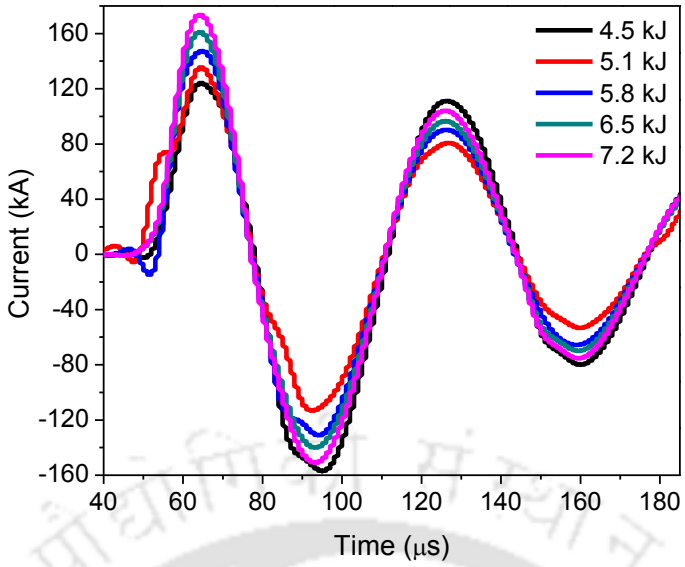

Fig. 8.4 Measured discharge current sinusoidal curve at five values energies

The discharge current is a typical damped sinusoidal curve and it can be well expressed by the mathematical relation given by equation (8.9).

$$I(t) = \frac{V_o}{\omega L} e^{-\beta\tau} \sin(\omega\tau) \tag{8.9}$$

where V_0 represents the initial discharge voltage, L represents the equivalent inductance of the system, ω represents the angular frequency, and β represents the damping exponent [70].

8.2.2 Outer diameter measurement and calculation

The outer diameter of the model calculated from the simulation (shown in Fig. 8.5(a)) was compared with the outer diameter of the crimped sample measured (shown in Fig. 8.5(b)). In the measured outer diameter of the crimped sample as shown in Fig. 8.5(b), D represents the outer diameter, C is the circumference, and S is the area of the circle.

There was a difference in the simulated diameter and measured diameter. The reason for the difference was due to the coarse mesh of the elements in the simulation. Coarse mesh causes relatively more gap at the interface, due to large element size and hence increase the outer diameter. The element size used in this work was sufficient for the objectives obtained in this work, and hence no finer mesh or mesh refinement was done. Fine mesh leads to higher simulation time as well as complexity in the convergence of the solutions.

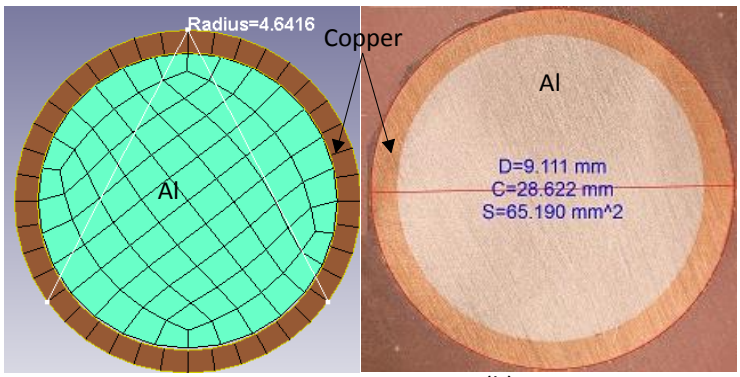

(a) Simulation (b) Experiment

Fig. 8.5 Outer diameter of the crimped sample measured in (a) simulation, and (b) experiment at 7.2 kJ of discharge energy

8.2.3 Temperature calculation and measurement

The temperature generated in the associated components such as the coil, field shaper and flyer tube at the working zone was studied, and the same was also simulated and compared. The thermo-graphic image of the arrangement of the working zone with field shaper is shown in Fig. 8.6(a). The temperature generated in the working zone in the experiment was measured by using an infrared thermometer. The infrared thermometer works on the principle that each body with a temperature above the absolute zero emits electromagnetic radiation from its surface, which is proportional to its intrinsic temperature or infrared radiation. At four different locations P1, P2, P3, and P4, on the tube the temperature was measured. The temperature was also calculated at the same locations as the experiments in the simulated model. The locations were the temperature measured in the experiments and the simulation is depicted in Fig. 8.6(a).

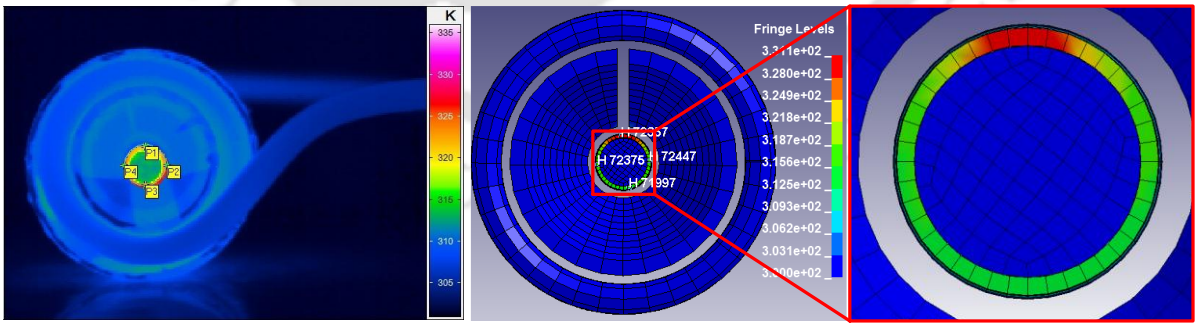

(a) (b) (c)

Fig. 8.6 Four different locations of temperature measurement (a) experimental result, (b) simulated result, and (c) magnified view of simulated result

Although, the temperature generated in all the components were studied. However, the variation in the temperature in the field shaper as well as in the coil were minimal, and that was

below 5 ℃. The comparative plot of simulated values of the maximum temperature with the peak value of the discharge current is shown in Fig. 8.7. It was observed that the maximum temperature generated in the simulation was more than that of the corresponding experimental values. This variation can be due to leakage of the current and losses in the experiment. The maximum variation between the values of the simulated from the experimental one was found to be 5.4 %.

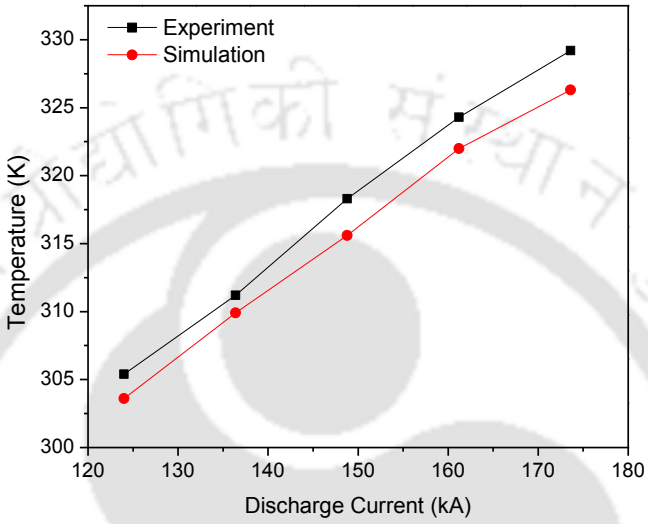

Fig. 8.7 Comparison of temperature measured in the experiment and the simulated

8.2.4 Magnetic field calculations

The magnetic field generated on the flyer tube circumference with five different tapered angles of the field shaper 14.4°, 15.2°, 15.9°, 16.7°, and 17.4° is shown in Fig. 8.8. From the magnetic field based analysis it was observed that with the increased in the tapered angle on the field shaper the magnetic field generated on the tube was also increased. The field shaper field having a tapered angle of 17.4° was found more efficient among the five different field shapers used.

The fringe pattern of the magnetic field generated in the flyer tube with the different types of the field shaper is shown in Fig. 8.9. From the analysis, it was found that with the increase in the magnitude of the tapered angle the magnetic field was also increased. The peak value of the magnetic field develops on the flyer tube with three different tapered angles 14.4°, 15.9°, and 17.4° at 7.2 kJ of the discharge energy are 11.51 Tesla, 12.20 Tesla, and 12.75 Tesla respectively.

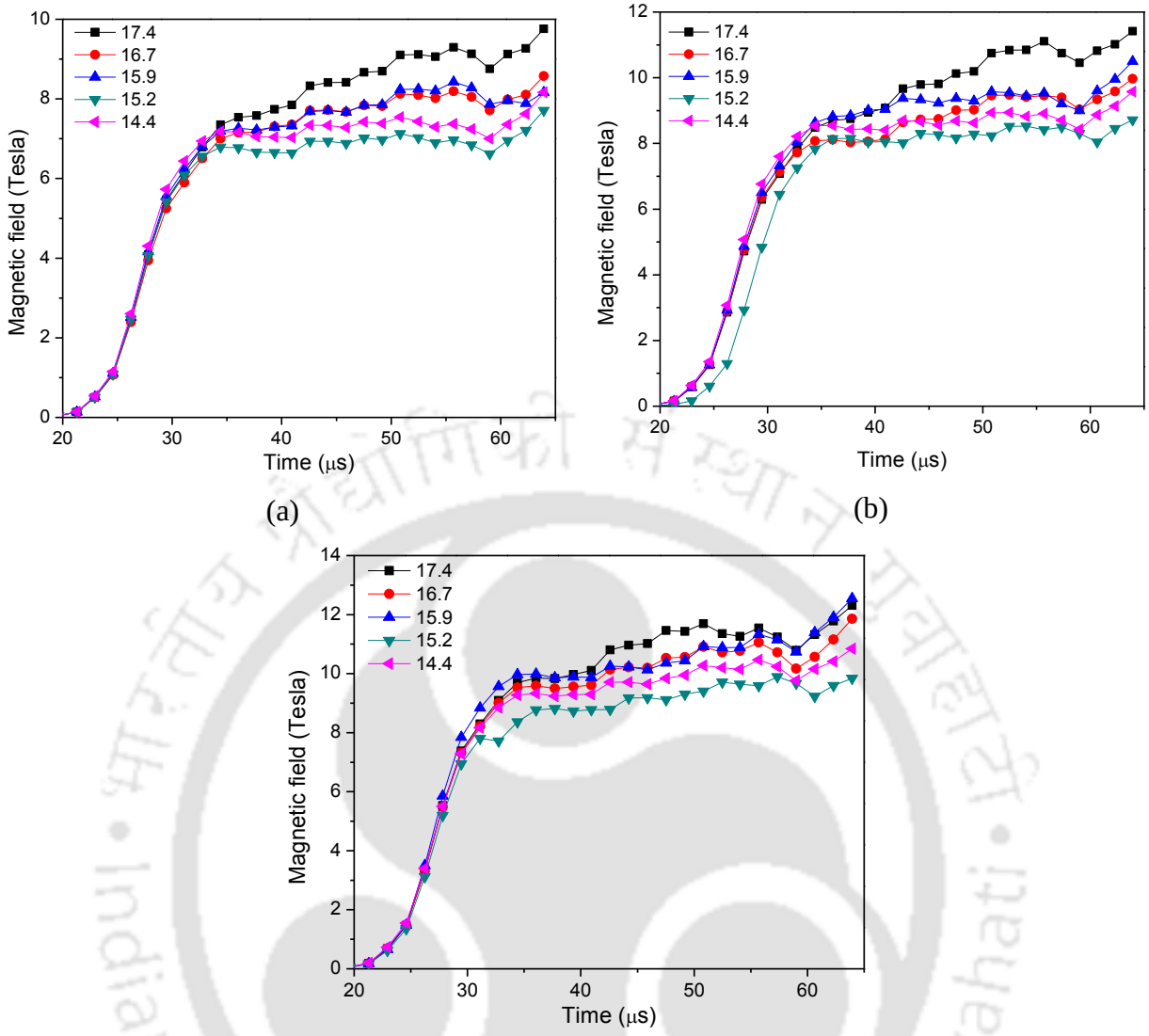

Fig. 8.8 Magnetic field comparison of five different types of field shaper at (a) 4.5 kJ, (b) 5.8 kJ, and (c) 7.2 kJ

8.2.5 Impact velocity and plastic strain results

In this process, flyer tube will impact on the rod with high-velocity. The magnitude of the velocity of impact of the flyer tube will be changed with the change in the taper angle of the field shaper. For five different tapered angles, the velocity of impact was compared and it is shown in Fig. 8.10(a). From this comparison, it was found that with the increase in the tapered angle of the field shaper the velocity of impact also increases. The high-velocity impact of the tube on the rod causes a plastic strain in the tube. The magnitude of the plastic strain also affected by the tapered angle of the field shaper. The magnitude of plastic strain was compared for five different tapered angles at 7.2 kJ of discharge energy and it is in Fig. 8.10(b).

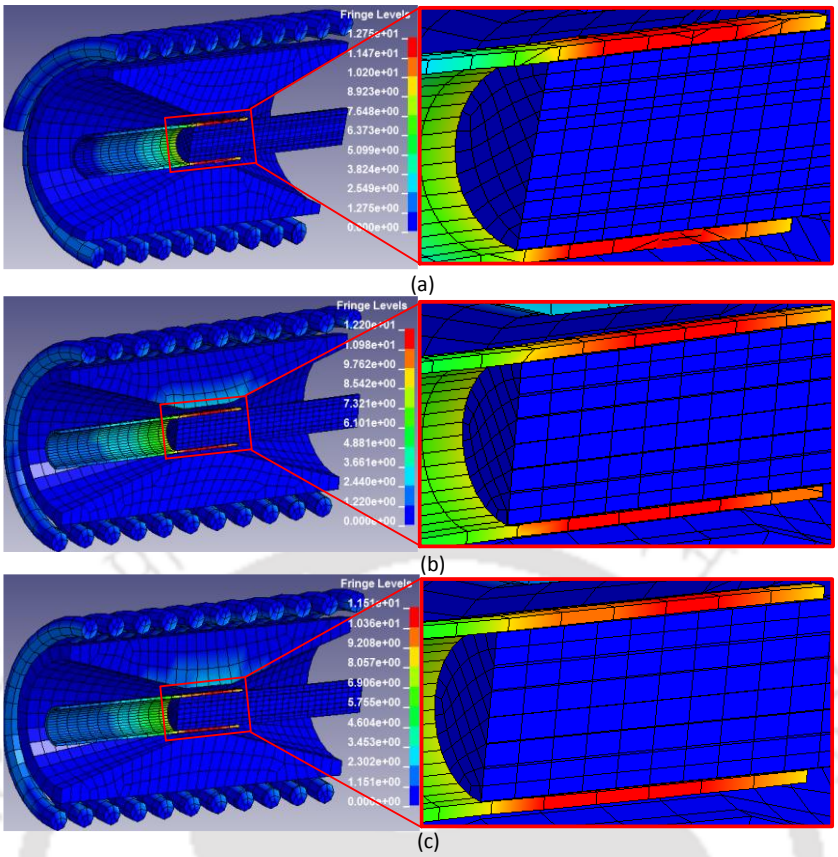

Fig. 8.9 Fringe pattern of the magnetic field of three different types of field shaper with (a) 17.4°, (b) 15.9°, and (c) 14.4° tapered angle at 7.2 kJ of the discharge energy

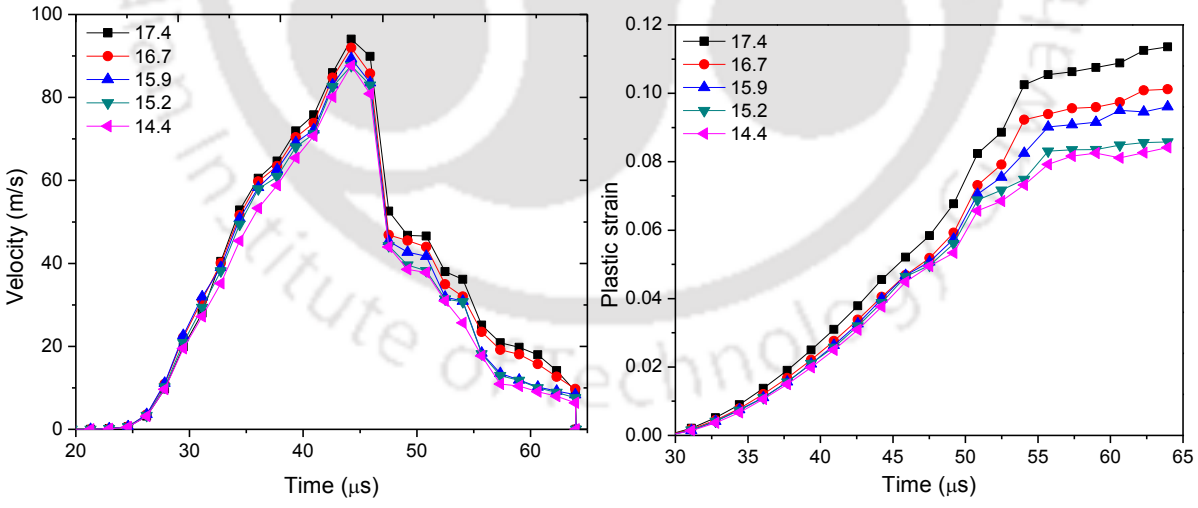

(a) (b)

Fig. 8.10 Comparison of (a) impact velocity, and (b) plastic strain of five different field shapers at 7.2 kJ of discharge energy

The numerical model was simulated for different values of the discharge energy or discharge current. From the simulations, it can be concluded that with the increase in the magnitude of

the discharge energy the impact velocity of the tube and the plastic strain developed in the tube increases. The peak value of the impact velocity developed in the tube at different discharge energy for five different types of field shaper is shown in Fig. 8.11(a). The maximum value of the plastic strain developed in the tube at different discharge energies for five different types of field shaper is shown in Fig. 8.11(a).

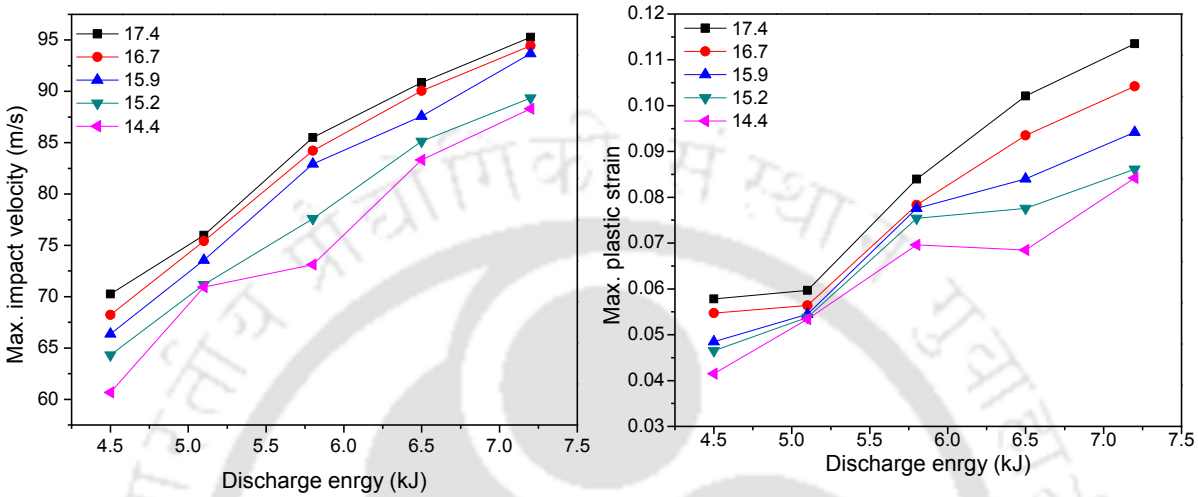

(a) (b)

Fig. 8.11 Variation of (a) impact velocity, and (b) plastic strain of five different field shapers with the discharge energy

8.3 Conclusion

The strength of the joint can be increased by increasing the magnitude of the peak value of the discharge current or by increasing the amount of the discharge energy. In this study, a validated numerical model based on temperature and the outer diameter of the tube was used to study the effect of the tapered angle of the field shaper. For this study, the tapered angle of the tube was varied as 14.4°, 15.2°, 15.9°, 16.7°, and 17.4° and other parameters like outer diameter, total length, inner diameter, and the working length of the field shaper were kept constant. The increase in the tapered angle of the field shaper, and maintaining the other parameters constant the impact velocity of the tube, magnetic field and plastic strain developed in the tube also increase.

.----------*----------*----------.

9 Conclusions and Scopes of Future

9.1 Conclusions

The electromagnetic crimping is a high energy, high strain rate, high velocity and green mechanical joining technique. This technique can be used for joining either similar or dissimilar materials. The important results obtain from the thesis work are as follows:

- Initially, feasibility study and the optimization of the process parameters of the electromagnetic crimping process was carried out. From the numerical results and experimental work it was found that process parameters such as stand-off distance, discharge energy and impact velocity is the governing parameters. To obtain the joint between the mating parts minimum value of these parameters must be maintained.
- The life of the solenoid coil used in the experiment was very short, not more than 10 shorts. From the experimental work it was observed that the life of the coil can be increased significantly minimum up to 100 by using the field shaper.
- To increase the strength of the joint produced by electromagnetic crimping process three types of profiles threaded, knurled, and plain were created on the base rod. Based on the mechanical tests of the joints it was concluded that the strength of the joint produced with the threaded profile was more than that of the knurled and plain profiles.
- The performance of the field shaper can be increased by modifying the geometry of the field shaper. Three combinations of the field shapers step-tapered, stepped and tapered field shaper were studied in the experiment. From the experimental work it can be concluded that the performance of the step-tapered field shaper was better among them.
- The performance of the step-tapered, stepped and tapered field shaper was also compared based on the numerical study. From the numerical study it can be concluded that the magnitude of the Lorentz force, magnetic field and current density developed with the step-tapered field shaper was higher than the stepped and tapered field shaper. The maximum value of the Lorentz force, magnetic field and current density developed at 7.2 kJ of the discharge energy with the step-tapered field shaper was 1093 N, 17.14 Tesla and 0.0639 A/m^2.

9.2 Future Scopes

Few more studies can be done in this field. Some of those studies can be

- The study of effect of the slit geometry of the field shaper on the magnetic field density and impact velocity of the flyer tube during EMC.
- Study based on the effect of heating of flyer tube and/or base rod on the strength of the joint in the EMC.
- Effect of surface roughness on the rod and/or inside surface of the tube on the bond strength and joint quality during EMC.
- Effect of the different surface coating on the joint strength and quality of the joint during EMC.
- Effect of the conductivity of the base rod on the joint strength and joint quality during EMC.
- Measurement of magnetic field generated in the flyer and field shaper in EMC.

----------*----------*----------.

References

[1] S. F. Golovashchenko, A. J. Gillard and A. V. Mamutov, "Formability of Dual Phase Steels in Electrohydraulic Forming," *Journal of Materials Processing Technology*, vol. 213, no. 7, pp. 1191-1212, 2013.

[2] S. D. Kore, J. Imbert, Y. Zhou and M. Worswick, "Magnetic Pulse Welding," *ASM Handbook*, vol. 06A, pp. 704-709, 2011.

[3] J. K. Doley and S. D. Kore, "FEM Study on Electromagnetic Formability of AZ31B Magnesium alloy," *6th International Conference on High Speed Forming* , pp. 273-280, 2014.

[4] A. Vivek, S. R. Hansen, B. C. Liu and G. S. Daehn, "Vaporizing Foil Actuator: A Tool for Collision Welding," *Journal of Materials Processing Technology*, vol. 213, no. 12, pp. 2304-2311, 2013.

[5] S. V. Desai, S. Kumar, P. Satyamurthy, J. K. Chakravartty and D. P. Chakravarthy, "Scaling Relationships for Input Energy in Electromagnetic Welding of Similar and Dissimilar Metals," *Journal of Electromagnetic Analysis and Applications*, vol. 2, pp. 563-570, 2010.

[6] M. Kimchi, H. Shao, W. Cheng and P. Krishnaswamy, "Magnetic Pulse Welding Aluminum Tubes to Steel Bars," *Welding in the World*, vol. 48, pp. 19-22, 2004.

[7] H. Hokari, T. Sato, K. Kawauchi and A. Muto, "Magnetic Impulse Welding of Aluminium Tube and Copper Tube with Various Core Materials," *Welding International*, vol. 12, no. 8, pp. 619-626, 1998.

[8] R. M. Miranda, B. Tomas, T. G. Santos and N. Fernandes, "Magnetic Pulse Welding on the Cutting Edge of Industrial Applications," *Soldagem & Inspecao*, vol. 19, no. 01, pp. 69-81, 2014.

[9] Y. Y. Chu and R. S. Lee, "Effect of Field Shaper Geometry on the Lorentz Force for Electromagnetic Sheet Impact Forming Process," *Journal of Engineering Manufacturing*, vol. 227, no. 2, pp. 324-332, 2014.

[10] A. R. F. Arezoodar, E. Garzan and H. Ebrahimi, "Effect of Various Field Shapers on Magnetic Pressure in Electromagnetic Inward Tube Forming," *Advances in Fluid Mechanics and Heat & Mass Transfer*, pp. 338-342, 2012.

[11] R. Chaharmiri and A. F. Arezoodar, "The Effect of Stepped Field Shaper on Magnetic Pressure and Radial Displacement in Electromagnetic Inside Bead Forming: Experimental and Simulation Analyses Using MAXWELL and ABAQUS Software," *Journal of Manufacturing Science and Engineering*, vol. 139, no. 6, p. 061003, 2017.

[12] Y. Murakoshi, M. Takahashi, T. Sano, K. Hanada and H. Negishi, "Inside Bead Forming of Aluminum Tube by Electro-magnetic Forming," *Journal of Materials Processing Technology*, Vols. 80-81, pp. 695-699, 1998.

[13] H. Suzuki, M. Murata and H. Negishi, "The Effect of a Field Shaper in Electromagnetic Tube Bulging," *Journal of Mechanical Working Technology*, vol. 15, pp. 229-240, 1987.

[14] P. Zhang, M. Kimchi, H. Shao, J. E. Gould and G. S. Daehn, "Analysis of the Electromagnetic Impulse Joining Process with a Field Concentrator," *In AIP Conference Proceedings*, vol. 712, no. 1, pp. 1253-1258, 2004.

[15] H. Yu, C. Li, . Z. Zhao and Z. Li, "Effect of Field Shaper on Magnetic Pressure in Electromagnetic Forming," *Journal of Materials Processing Technology*, vol. 168, pp. 245-249, 2005.

[16] J. Lueg-Althoff, A. Lorenz, S. Gies, C. Weddeling, G. Goebel, A. E. Tekkaya and E. Beyer, "Magnetic Pulse Welding by Electromagnetic Compression: Determination of the Impact Velocity," *Advanced Materials Research*, Vols. 966-967, pp. 489-499, 2014.

[17] J. G. Lee, J. J. Park, M. K. Lee, C. K. Rhee, T. K. Kim, A. Spirin, V. Krutikov and S. Paranin, "End Closure Joining of Ferritic-Martensitic and Oxide-Dispersion Strengthened Steel Cladding Tubes by Magnetic Pulse Welding," *Metallurgical and Materials Transactions A*, pp. 1-8, 2015.

[18] S. D. Kore, P. P. Date and S. V. Kulkarni, "Effect of Process Parameters on Electromagnetic Impact Welding of Aluminum Sheets," *International Journal of Impact Engineering*, vol. 34, pp. 1327-1341, 2007.

[19] Y. Haiping, F. Zhisong and L. Chunfeng, "Magnetic Pulse Cladding of Aluminum Alloy on Mild Steel Tube," *Journal of Materials Processing Technology*, vol. 214, pp. 141-150, 2014.

[20] J. Y. Shim, I. S. Kim, M. J. Kang, I. J. Kim, K. J. Lee and B. Y. Kang, "Joining of Aluminum to Steel Pipe by Magnetic Pulse Welding," *Materials Transactions*, vol. 52, no. 5, pp. 999-1002, 2011.

[21] M. Marya, M. Rathod, S. Marya, M. Kutsuna and D. Priem, "Steel-to-Aluminum Joining by Control of Interface Microstructures─ Laser-Roll Bonding & Magnetic Pulse Welding ─," *Materials Science Forum*, Vols. 539-543, pp. 4013-4018, 2007.

[22] V. Psyk, D. Risch, B. L. Kinsey, A. E. Tekkaya and M. Kleiner, "Electromagnetic Forming—A Review," *Journal of Materials Processing Technology*, vol. 211, no. 5, pp. 787-829, 2011.

[23] J. K. Doley and S. D. Kore, "Studies on Temperature Distribution in Electromagnetic Welding Process," *Materials Performance and Characterization*, vol. 1, no. 1, pp. 1-11, 2012.

[24] S. D. Kore, P. Dhanesh, S. V. Kulkarni and P. P. Date, "Numerical Modeling of Electromagnetic Welding," *International Journal for Applied Electromagnetics and Mechanics*, vol. 32, no. 1, pp. 1-19, 2010.

[25] Z. Fan, H. Yu, F. Meng and C. Li, "Experimental Investigation on Fabrication of Al/Fe Bi-metal Tubes by the Magnetic Pulse Cladding Process," *International Journal of Advanced Manufacturing Technology*, vol. 83, no. 5-8, pp. 1409-1418, 2016.

[26] S. D. Kore, P. P. Date, S. V. Kulkarni, S. Kumar, D. Rani, M. R. Kulkarni, S. V. Desai, R. K. Rajawat, K. V. Nagesh and D. P. Chakravarty, "Application of Electromagnetic Impact Technique for Welding Copper-to-Stainless Steel Sheets," *International Journal of Advanced Manufacturing Technology*, vol. 54, pp. 949-955, 2011.

[27] Z. Fan, H. Yu and C. Li, "A Numerical Investigation on Magnetic Pulse Cladding of Bi-Metal Tubes," *6th International Conference on High Speed Forming*, pp. 151-160, 2014.

[28] I. Masumoto, K. Tamaki and M. Kojima, "Electromagnetic Welding of Aluminum Tube to Aluminum or Dissimilar Metal Cores," *Transactions of the Japan Welding Society*, vol. 16, no. 2, pp. 110-116, 1985.

[29] K. Tamaki and M. Kojima, "Factors Affecting the Result of Electromagnetic Welding of Aluminum Tube," *Transactions of the Japan Welding Society*, vol. 19, no. 1, pp. 53-59, 1988.

[30] M. Kojima, K. Tamaki and T. Furuta, "Effect of Coliision Angle on the Result of Electromagnetic Welding of Aluminum," *Transactions of the Japan Welding Society*, vol. 20, no. 2, pp. 112-118, 1989.

[31] A. Stern and M. Aizenshtein, "Bonding Zone Formation in Magnetic Pulse Welds," *Science Technology*, vol. 7, no. 5, pp. 339-342, 2002.

[32] K. Faes, T. Baaten, W. D. Waele and N. Debroux, "Joining of Copper to Brass Using Magnetic Pulse Welding," *4th International Conference on High Speed Forming*, pp. 84-96, 2010.

[33] X. Zhidan, Y. Haiping, L. Chunfeng and H. Yujie, "Interface Microstructure of Al-Fe Tubes Joint by Magnetic Pulse Welding," *Journal of Iron and Steel Research International*, vol. 19, pp. 442-445, 2012.

[34] R. N. Raoelison, N. Buiron, M. Rachik, D. Haye, G. Franz and M. Habak, "Study of the Elaboration of a Practical Weldability Window in Magnetic Pulse Welding," *Journal of Materials Processing Technology*, vol. 213, pp. 1348-1354, 2013.

[35] X. Zhidan, C. Junjia, Y. Haiping and L. Chunfeng, "Research on the Impact Velocity of Magnetic Impulse Welding of Pipe Fitting," *Materials and Design*, vol. 49, pp. 736-745, 2013.

[36] S. A. A. A. Mousavi and P. F. Sartangi, "Experimental Investigation of Explosive Welding of Cp-Titanium/AISI 304 Stainless Steel," *Materials & Design*, vol. 30, no. 3, pp. 459-468, 2009.

[37] A. Stern, V. Shribman, A. Ben-Artzy and M. Aizenshtein, "Interface Phenomena and Bonding Mechanism in Magnetic Pulse Welding," *Journal of Materials Engineering and Performance*, vol. 23, pp. 3449-3458, 2014.

[38] J. Y. Shim and B. Y. Kang, "Distribution of Electromagnetic Force of Square Working Coil for High-Speed Magnetic Pulse Welding Using FEM," *Materials Sciences and Applications*, vol. 4, pp. 856-862, 2013.

[39] J. Y. Shim, I. S. Kim, K. J. Lee and B. Y. Kang, "Experimental and Numerical Analysis on Aluminum/Steel Pipe Using Magnetic Pulse Welding," *Met. Mater. Int.*, vol. 17, no. 6, pp. 957-961, 2011.

[40] A. Guglielmetti, N. Buiron, M. Marceau, M. Rachik and C. Rachik, "Modelling of Tubes Magnetic Pulse Welding," *Proceedings of the ASME 2012 11th Biennial Conference on Engineering Systems Design and Analysis*, pp. 1-12, 2012.

[41] Z. Fan, H. Yu and C. Li, "Plastic Deformation Behavior of Bi-Metal Tubes during Magnetic Pulse Cladding: FE Analysis and Experiments," *Journal of Materials Processing Technology*, vol. 229, pp. 230-243, 2015.

[42] A. Kapil and A. Sharma, "Magnetic pulse welding: an Efficient and Environmentally Friendly Multi-Material Joining Technique," *Journal of Cleaner Production*, vol. 100, pp. 35-58, 2015.

[43] X. Zhidan, C. Junjia, Y. Haiping and L. Chunfeng, "Research on the Impact Velocity of Magnetic Impulse Welding of Pipe Fitting," *Materials and Design*, vol. 49, pp. 736-745, 2013.

[44] X. Wu and J. Shang, "An Investigation of Magnetic Pulse Welding of Al/Cu and Interface Characterization," *Journal of Manufacturing Science and Engineering*, vol. 136, pp. 1-11, 2014.

[45] A. Lorenz, J. Lueg-Althoff, G. Gobel, C. Weddeling, E. Beyer and A. E. Tekkaya, "Influence of Axial Workpiece Positioning during Magnetic Pulse Welding of

Aluminum-Steel Joints," *6th International Conference on High Speed Forming*, pp. 189-198, 2014.

[46] V. Gonda, P. Racz and D. Horvath, "Joining of Tubular Parts by Electromagnetic Forming: Computational Investigations of Strength," *Materials Science Forum Volume*, vol. 792, pp. 194-197, 2014.

[47] T. Hammers, M. Marre, J. Rautenberg, P. Barreiro, V. Schulze, D. Biermann, A. Brosius and A. E. Tekkaya, "Influence of Mandrel's Surface and Material on the Mechanical Properties of Joints Produced by Electromagnetic Compression," *Steel Research International*, vol. 80, no. 5, pp. 366-375, 2009.

[48] J. Bellmann, J. Lueg-Althoff, G. Goebel, S. Gies, E. Beyer and A. E. Tekkaya, "Effects of Surface Coatings on the Joint Formation During Magnetic Pulse Welding in Tube-to-Cylinder Configuration," *Proceedings of the 7th International Conference on High Speed Forming Dortmund, Germany*, pp. 279-288, 2016.

[49] K. Faes, O. Zaitov and E. D. Waele, "Electromagnetic Pulse Crimping of Axial Form Fit Joints," *5th International Conference on High Speed Forming*, pp. 229-242, 2012.

[50] C. Weddeling, S. T. Woodward, M. Marre, J. Nellesen, V. Psyk, A. E. Tekkaya and W. Tillmann, "Influence of Groove Characteristics on Strength of Form-Fit Joints," *Journal of Materials Processing Technology* , vol. 211, pp. 925-935, 2011.

[51] C. Weddeling, S. Woodward, J. Nellesen, V. Psyk, M. Marre, A. Brosius, A. E. Tekkaya, G. S. Daehn and W. Tillmann, "Development of Design Principles for Form-Fit Joints in Lightweight Frame Structures," *4th International Conference on High Speed Forming*, pp. 137-148, 2010.

[52] M. Acarer, "Electrical, Corrosion and Mechanical Properties of Aluminum–Copper Joints Produced by Explosive Welding," *Journal of Materials Engineering and Performance*, vol. 21, no. 11, pp. 2375-2379, 2012.

[53] K. Faes and I. Kwee, "Electromagnetic Pulse Welded Aluminium to Copper Sheet Joints: Morphological and Mechanical Characterization," *Proceedings of the 7th International Conference on High Speed Forming Dortmund, Germany*, pp. 299-308, 2016.

[54] R. N. Raoelison, N. Buiron, M. Rachik, D. Haye and G. Franz, "Efficient Welding Conditions in Magnetic Pulse Welding Process," *Journal of Manufacturing Processes*, vol. 14, pp. 372-377, 2012.

[55] K. H. Grote and E. K. Antonsson, "Fundamentals of Magnetic Pulse Welding for the Fabrication of Dissimilar Material Structures," *Springer Handbook of Mechanical Engineering*, pp. 723-733, 2009.

[56] S. D. Kore and P. P. Kulkarni, "Effect of Process Parameters on Electromagnetic Welding of Aluminum Sheets," *International Journal of Impact Engineering*, vol. 34, pp. 1327-1341, 2006.

[57] R. Raoelison, M. Rachik, N. Buiron, D. Haye, M. Morel, B. D. Sanstos, D. Jouaffre and G. Frantz, "Assessment of Gap and Charging Voltage Influence on Mechanical Behaviour of Joints Obtained by Magnetic Pulse Welding," *5th International Conference on High Speed Forming*, pp. 207-216, 2012.

[58] H. Kim, J. Gould, J. Shang, A. Yadav, R. Meyer and P. L'Eplattenier, "Numerical Simulations to Investigate the Efficiency of Joint Designs for the Electro-Magnetic Welding (EMW) of the Ring-shaft Assembly," *13th International Ls-Dyna Users Conference* , pp. 1-10, 2014.

[59] G. Gunther, B. Eckard, K. Jorg and B. Berndt, "Dissimilar Metal Joining: Macro- and Microscopic Effects of MPW," *5th International Conference on High Speed Forming*, pp. 179-188, 2012.

[60] J. K. Shim, B. Y. Kang, I. S. Kim, M. J. Kang, D. H. Park and I. J. Kim, "A Study on Distributions of Electromagnetic Force of the Dissimilar Metal Joining in MPW using a FEM," *Advanced Materials Research*, vol. 86, pp. 214-221, 2010.

[61] H. O. S. Eide and E. A. Melby, "Blast Loaded Aluminium Plates Experiments and Numerical Simulations," *Master Thesis Norwegian University of Science and Technology*, pp. 1-139, 2013.

[62] K. Vedantam, D. Bajaj, N. S. Brar and S. Hill, "Johnson-Cook Strength Models for Mild and DP 590 Steels," *American Institute of Physics*, pp. 775-779, 2006.

[63] Y. Haiping and L. Chunfeng, "Effects of Current Frequency on Electromagnetic Tube Compression," *Journal of Materials Processing Technology*, vol. 209, pp. 1053-1059, 2009.

[64] S. A. A. A. Mousavi, S. J. Burley and S. T. S. Al-Hassani, "Simulation of Explosive Welding using the Williamsburg Equation of State to Model Low Detonation Velocity Explosives," *International Journal of Impact Engineering* , vol. 31, pp. 719-734, 2005.

[65] S. Mroz, G. Stradomski, H. Dyja and A. Galka, "Using the Explosive Cladding Method for Production of Mg-Al Bimetallic Bars," *Archives of Civil and Mechanical Engineering*, vol. 15, pp. 317-323, 2015.

[66] K. Vahedi and N. Khazraiyan, "Numerical Modeling of Ballistic Penetration of Long Rods into Ceramic/Metal Armors," *8th International LS-DYNA Users Conference*, vol. 14, pp. 39-50, 2004.

[67] M. A. Meyers, Dynamic Behavior of Materials, Canada: John Wiley & Sons, Inc, 2004.

[68] C. Maria, "Technology of EHIS (Stamping) Applied to Production of Automotive Parts," 2009.

[69] L. E. Schwer, "Aluminium Plate Perforation: A comparative Case Study Using Lagrange with Erosion, Multi-Material ALE, and Smooth Particle Hydrodynamics," in *7th European LS-DYNA Conference*, 2009.

[70] Z. Fan, H. Yu and C. Li, "Plastic Deformation Behavior of Bi-Metal Tubes during Magnetic Pulse Cladding: FE Analysis and Experiments," *Journal of Materials Processing Technology*, vol. 229, pp. 230-243, 2015.

.----------*----------*----------.

भारतीय प्रौद्योगिकी संस्थान गुवाहाटी
Indian Institute of Technology Guwahati

List of Publications

Journals

1. R. Kumar and S. D. Kore, "Effects of Surface Profiles on the Joint Formation during Magnetic Pulse Crimping in Tube-to-Rod Configuration," *International Journal of Precision Engineering and Manufacturing* , vol. 18, no. 9, pp. 1181-1188, 2017.

2. R. Kumar and S. D. Kore, "Electromagnetic Crimping in Tube-to-Cylinder Configuration: Influence of the Base Profiles on the Joint Quality," *Journal of Testing and Evaluation*, vol. 46, no. 3, pp. 1-14, 2018.
3. R. Kumar and S. D. Kore, "Numerical Study on Pulsed Magnetic Crimping of Tubes," *International Journal of Materials and Product Technology*, 2018. (Submitted revised paper on Nov 2017)
4. R. Kumar and S. D. Kore, "Effect of Field Shaper Geometry on Electromagnetic Pulsed Crimping of Tube on Rod," *The International Journal of Advanced Manufacturing Technology*, 2018. (Revision submitted on October 2018)
5. R. Kumar and S. D. Kore, "Numerical Prediction and Experimental Validation of Heating with Various Field Shaper Geometries in Electromagnetic Crimping of Tubes on Rods", *International Journal of Material Forming* (Submitted revision on Jul 2018).

Book Chapter

1. R. Kumar and S. D. Kore, "Pulse Electromagnetic Crimping of Al-Tube on DP Steel Rod," in *Strengthening and Joining by Plastic Deformation*, Springer, 2018.

Conferences

1. R. Kumar and S. D. Kore, "Pulse Electromagnetic Cladding of Al-Tube on DP Steel Rod," *Proceedings of 6th International & 27th All India Manufacturing Technology, Design and Research Conference (AIMTDR–2016)*, pp. 611-615, 2016.
2. R. Kumar, J. Doley and S. Kore, "Finite Element Modeling and Analysis of Electro-Magnetic Pulse Welding of Aluminium Tubes to Steel Bars," AIP Conference Proceedings, vol. 1769, no. 1, p. 060003, 2016.
3. R. Kumar and S. D. Kore, "Finite Element Modelling and Analysis of the Effect of Frequency on the Electromagnetic Compression of Tubes," In Journal of Physics Conference Series, vol. 759, no. 1, p. 012055, 2016.
4. R. Kumar, A. K. Rajak and S. D. Kore, "Numerical and Experimental Study of Electromagnetic Crimping," *8th International Conference on High Speed Forming (ICHSF 2018) 2018.*

.----------*----------*----------

भारतीय प्रौद्योगिकी संस्थान गुवाहाटी
Indian Institute of Technology Guwahati